Thermo-Mechanical Creep Behavior of Clearwater Caprock

by

Susan Sarmiento

A thesis submitted in partial fulfillment of the requirements for the degree of

Master of Science

in

Geotechnical Engineering

Department of Civil and Environmental Engineering

University of Alberta

ABSTRACT

Alberta's oil sands deposits are the third-largest proven crude oil reserve in the world. However, only 20% of the bitumen in Alberta's oil sands are shallow enough to be recoverable by surface mining techniques; the remaining 80% can only be extracted using in-situ techniques that involve the injection of steam at high temperatures, such as Steam Assisted Gravity Drainage (SAGD) and Cyclic Steam Stimulation (CSS). In order to guarantee the safety of the projects, the isolation of the injected fluid in the subsurface should be assured over the lifetime of a project. Caprock integrity has been identified as one of the main concerns that allow communication of the reservoir with the upper geological layers in thermal operations in the oil sands production. Clearwater Formation is the main caprock that hydraulically isolates the reservoir with the upper permeable zones and ground surface in the Athabasca area. Clearwater clay shales are typically classified as a "hard soil/ soft rock", representing the complexity when characterizing the mechanical behavior of the material.

This research is aimed to enrich the geomechanical characterization of Clearwater caprock through laboratory testing. Intact and reconstituted Clearwater samples test results served to identify the intrinsic properties of the material, the effects of material structure on caprock behavior, and the approximate degree of overconsolidation and yield stress. These studies evidenced that creep dominates the time-dependent behavior of Clearwater caprock. Time-dependent tests were used to evaluate the best way to analyze and understand the creep behavior of Clearwater for different laboratory conditions, and to find significant material properties and parameters that can be used to characterize and predict the long-term behavior of Clearwater clay-shale caprock. Finally, thermal creep tests supplement creep findings for the particular case of thermal recovery applications. From the latter tests, it was studied how temperature affects long-term deformation of Clearwater clay-shale at in-situ effective stress conditions. Furthermore, key parameters required to obtain quality tests when high temperature is involved were identified.

Models used in geomechanical simulation should honor the experimental results that the materials described in these tests, since having a proper understanding of the geomechanical response to thermal recovery of the reservoir and overlaying formation is crucial to avoid caprock integrity issues.

ACKNOWLEDGMENTS

The world is a better place because there is always someone out there helping others. I am immensely grateful for the people around me over the past couple of years, for their actions, comments, or just a sincere smile, it is a pleasure to acknowledge them.

I would like to especially thank my kind and generous supervisor, Dr. Rick Chalaturnyk, for admitting me as a graduate student and believe in my abilities even though I came from a different background. He has become someone I feel lucky to call a mentor whose wise counsel has shaped my work.

A special thanks to the excellent and dedicated staff of the Reservoir Geomechanics Research Group, Nathan Deisman, Stephen Talman, Keivan Khaleghi, Gilbert Wong, and Hope Walls, for their advice at various stages along the way. Nathan's thoughtful support helped me to clarify and push forward my thinking. Stephen became my "universal professor" who not only enlightened me with his insightful comments but also with his bad jokes. I am also grateful for my office and lab colleagues that now I can call friends, for their welcome distractions when research did not go our way.

This research could not have been possible without the economic support of Energi Simulation and Petro China Canada. Many thanks to them.

Finally, and most crucial, I want to thank my family. Infinite thanks to my husband Juan, who spent sleepless nights with me and has been by my side at every step of this way. He has been my constant source of love and encouragement. To my parents, Sonia and Eusebio, for all of the sacrifices that they have made on behalf of my education. They taught me to be curious about the world and have the remarkable ability to make me feel my luckiest when times are at their hardest. For that, I am immensely grateful. To my sister Stefany, she lights up the darkest room as well as my life. She was also responsible for adding to my life the best gift someone has given me, my niece Alana.

TABLE OF CONTENTS

LIST OF TABLES

LIST OF FIGURES

CHAPTER 1: INTRODUCTION

1.1 PROBLEM STATEMENT

Alberta's oil sands deposits are the third-largest proven crude oil reserve in the world, with a total of 163.5 billion barrels reported at the end of 2018 (British Petroleum, 2020). Furthermore, only 20% of the bitumen in Alberta's oil sands are shallow enough to be recoverable by surface mining techniques, the remaining 80% (130.5 billion barrels) can only be extracted using in-situ techniques. In-situ techniques involve wellbores that are used to pump out the bitumen from the oil sands to the surface. Due to the chemical composition of bitumen, density and viscosity are much higher than conventional oil making it very hard to flow through the porous space of the formation and inside the wellbore. The most common in-situ techniques involve the injection of steam at high temperatures to reduce the viscosity of the bitumen, which facilitates flow from the sand formation to the wells where it can be pumped. On average, 50% of Alberta's bitumen production in 2019 was provided using in-situ methods such as Steam Assisted Gravity Drainage (SAGD) and Cyclic Steam Stimulation (CSS) (AER, 2020).

Among the different in-situ production techniques, SAGD has been identified as the most effective recovery method due to its high recovery factor and high production rates (Guo, Li, & Yu, 2016). SAGD involves drilling a pair of horizontal wells that can be longer than 1 km. The vertical spacing between the wells is usually lower than 9 m. Then steam is injected from the upper well (injector) into the formation heating up the bitumen to a temperature that it can flow by gravity to the lower well (producer) where the oil is pumped up continuously. This technique involves the development of a steam chamber in

the reservoir that grows in the vertical and lateral directions as the operation continues, eventually reaching vertical boundaries. At this point, heat transfer from the reservoir to the base of the caprock takes place. Thus, the bottom of the caprock can be exposed to high temperatures from the reservoir for periods of time longer than 25 years.

In order to guarantee the safety of the projects, the isolation of the injected fluid should be assured all the time. The reservoir and the wells must be hydraulically isolated to ensure the containment of the injected and reservoir fluids. Caprock integrity has been identified as one of the main concerns that allow communication of the reservoir with the upper geological layers in thermal operations in the oil sands production. The shallow condition of oil sands reservoirs represents challenging geomechanical conditions due to different factors such as the low values of in-situ stresses that can be easily overtaken by injection pressure and temperature that leads to reservoir containment loss. Also, the deformation in the reservoir generated by the changes in pore pressure and temperature alters the stress state of the overlying formations that can lead to shear and tensile failure. Likewise, formations are characterized by having a low degree of lithification which manifests in a complex geomechanical behavior since it is not clear if rock or soil like. For the majority of SAGD projects in Alberta, the Clearwater Formation is the main caprock that hydraulically isolates the reservoir with the upper permeable zones and ground surface in the Athabasca area. In previous studies, the Clearwater Formation has been referred to as a “hard soil/ soft rock” (Zadeh, 2016) representing the complexity when characterizing the mechanical behavior of the material.

Even though thermal recovery methods have been used in Alberta for the last 40 years, there are many unanswered questions related to the constitutive models of the formations. Previous studies results suggest that Clearwater shale follows a viscoelastic behavior that has not been studied yet. Due to the long-term nature of SAGD projects (>25 years) including this behavior in numerical analysis is critical to accurately predict the response of the material. In addition, previous test results also showed a distinct contractive response of the material when subjected to temperature increments that has not been analyzed yet. The present study aims to bring some clarification about these behaviors in the Clearwater shale material.

Previous incidents in thermal projects related to caprock integrity as Joslyn Creek steam release (2006) and Primrose flow to surface release (2009-2013) motivated new regulations for thermal operations. Currently, SAGD projects where the base of the caprock is shallower than 150 metres must submit geomechanical analysis prior to project development (AER, 2016). This includes numerical simulation to assure that the operations can be performed safely. Models used in geomechanical simulation should honor the experimental results for caprock formations; this is why having a proper understanding of the geomechanical response to thermal recovery of the reservoir and overlying formations is crucial to avoid caprock integrity issues.

1.2 RESEARCH OBJECTIVES

The purpose of this research is to enrich the geomechanical characterization of Clearwater caprock through laboratory testing. These experimental results are essential to improve model inputs that lead to more accurate predictions and analyses of caprock integrity through numerical modeling. The main research objectives are described below.

1. To study time-dependent behavior of Clearwater shale using different laboratory setup as isotropic cell and oedometer.
2. To perform and analyse changes in volume due to changes in temperature on Clearwater caprock using isotropic cell and oedometer for Clearwater shale.
3. To perform consolidation test in reconstituted samples in order to identify the main differences with respect to intact samples.

This research includes a detailed comparison between two common experimental setups, oedometer and isotropic cell, that are commonly used for different tests such as consolidation and thermal expansion/contraction. The present study also targets to identify the most appropriate experimental procedure for caprock integrity application recognizing their limitations and commonly faced issues during the experiments.

Finally, comparing results from reconstituted and intact samples allow to determine the influence of soil structure in the consolidation curve and creep behavior of the samples.

1.3 SCOPE AND METHODOLOGY

This study provides essential data for geomechanical analysis of thermal recovery that predicts fluids production and operations safety. The thesis describes experimental procedures that were performed in order to identify constitutive behavior of Clearwater caprock such as time-dependent behavior and changes of volume due to changes in temperature. Both the models and the data obtained from this study are critical information used in the geomechanical models.

Samples used were selected from a wellbore located at MacKay River Petro China Canada commercial project. Through four chapters, this thesis covers three main topics on experimental tests conducted on samples from a wellbore located at MacKay River Petro China Canada commercial project. In Chapter 2, Clearwater is characterized and the two different setups (oedometer and isotropic cell) used for the experiments are described. In Chapter 3, intact samples are remolded and reconstituted to be used in consolidation tests that aid to evaluate the impact of clay structure in the geomechanical behavior of the material. Chapter 4 looks into creep tests performed over a range of effective stress from 2 MPa to 14 MPa, which is a wider range than the typically expected values during SAGD operations. The final chapter focuses on thermal creep tests performed over a range from 20 °C to 190 °C which covers all the possible temperatures at the base of the caprock.

Throughout each chapter, specific arguments and ideas from previous research are studied and related to our proposed research. Then, our experimental methodology and results are shown and discussed for each topic.

CHAPTER 2: MATERIAL CHARACTERIZATION AND TESTING METHODOLOGY

2.1 CORE DESCRIPTION

In this research work, the Clearwater shale cores to be studied were retrieved from the Petro China Mackay River Project area and correspond to the Well 6-12-90-14-W4. The cores provided for this research were carefully vacuum packed and placed in cans filled with oil to maintain core integrity by assuring the least possible moisture lost and disturbance.

2.1.1 Clearwater Formation

The Clearwater Formation directly overlies the McMurray Formation, which is the bitumen reservoir in the area. The Clearwater Formation ranges in thickness from 55 m to 65 m within the MacKay River Petro China Canada project area. At the base of the Clearwater Formation is the Wabiskaw Member that is typically subdivided in a sandy layer commonly referred as Lower Wabiskaw and a clayey silt layer referred as Upper Wabiskaw. This member usually acts as a first seal that prevents hydraulic communication from the reservoir to the layers above. Nevertheless, the Wabiskaw Member does not meet the Alberta Energy Regulator Directive 86 criteria to be considered as an effective caprock. This directive states that a layer can be considered a caprock if it meets the following:

- be a minimum of 10 m thick;

- be composed of clay-rich bedrock, with a gamma-ray value greater than 75 API units; and
- be laterally continuous across the project area (AER, 2016)

Clearwater Formation is defined as a succession of marine mudstone and siltstone deposited in the Cretaceous. It represents normal marine, basinal, mud-dominated deposition bound by regional flooding surfaces. Within this unit the most argillaceous zone has been mapped in the area and is referred to as the Clearwater argillaceous caprock interval. The Clearwater argillaceous caprock interval exhibits the most clay-rich lithology of the Clearwater Formation and occurs in the lower half of the Clearwater above the Upper Wabiskaw. The Clearwater argillaceous caprock thickness varies from 22 to 29 m across the Mackay River project area. The upper portion of Clearwater is described as a silty mud with coarser grains than Clearwater argillaceous which decreases the effectiveness as a caprock. (Huag, Greene, & Mei, 2014)

2.1.2 Clay shale

Clay shale is a term that is commonly used in geotechnical engineering to refer argillaceous materials that are well consolidated but have not been lithified so cannot be considered rock. This group of geomaterials is fine-grained and composed predominantly of clay and silt sized particles. The mechanical behavior of this kind of material is difficult to classify and is usually described as “soft rock-hard soil”. This description captures the nature of the clay shale, which is usually stiffer and has higher strength than a soil while is also more ductile and has lower strength than a rock. Clay shale commonly have the following features:

- usually highly overconsolidated,
- commonly small scaled fissured,
- strong diagenetic bonding,
- tendency to slake when rewetted after drying,

- high swelling pressure in the presence of fresh water, and
- significant disintegration as a result of interaction with water (William, 2005).

2.1.3 MacKay Clearwater Formation In-Situ Stresses

The laboratory testing program performed on this research was designed to replicate in-situ stress conditions of the samples. To determine these conditions, information from different sources, such as well logs and public reports were gathered to obtain the most representative conditions in the experiments. It has been found in previous research (Malik Belmokhtar, Delage, Ghabezloo, & Conil, 2017; Hueckel & Borsetto, 1990; Kosar, 1989; Hiroki Sone, 2012) that properties such as thermal expansion coefficient and creep coefficient are highly dependent on the effective confining stress.

The total mean stress applied to the sample was obtained by calculating the average of the three principal stresses in the well area. Previous works near the field show that the region is currently under a reverse faulting regime ($\sigma_H > \sigma_h > \sigma_v$) when the depth is shallower than 500 m (Bell, Price, & McLellan, 1994). This regime is the result of loading-unloading cycles that have occurred at the North America in the last 100,000 years caused by glaciation processes. The last glaciation took place around 25,000 years ago when the north of Alberta was covered by Laurentide Glacier, a 2 km thick ice layer. Once the glacier retreated 11,000 years, the Athabasca River Valley was formed (Research Council of Alberta, 1959). Due to lateral confinement condition of the layers, the weight of the glacier led to significant increments of the horizontal stresses. Even though the formations have rebounded after the glacier retreat, close to the surface the horizontal stresses remain higher than the vertical stress. This process also explains the overconsolidated characteristic of Clearwater shale.

The total vertical stress is calculated by integrating the density log obtained from the well using the following equation:

$$\sigma_v = \int_0^D g\rho_{(z)} dz \tag{2.1}$$

Where:

σ_v: Vertical stress

g: Gravity

$\rho_{(z)}$: Density log

D: Depth

Figure 2.1 illustrates the log information for Well *6-12-90-14-W4.* The first track is the density log, the second track is the calculated differential stress for each value of density from track 1. The third track is the integration of the differential values, which represents the value of the vertical stress profile of the well. The colour scale on the right side of the plot illustrates the stratigraphic column of the well. As Figure 2.1 illustrates, the value of the total vertical stress at the base of the caprock where the samples were taken, as noted by the red cross, is 3800 kPa.

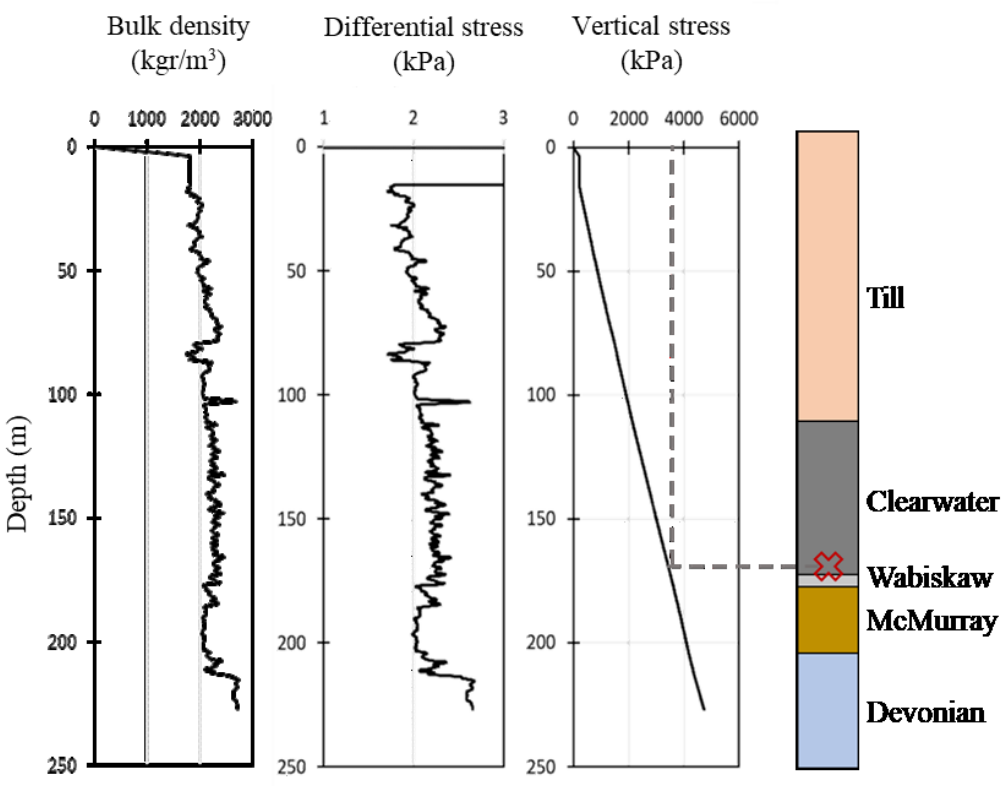

Figure 2.1: Density log, differential stress and total vertical stress for Well 6-12-90-14-W4.

The minimum horizontal stress is usually calculated from minifrac tests carried out in the field and can typically be found in the Annual Performance reports/presentations that companies are required to send to the Alberta Energy Regulator (AER) (Petrochina Canada, 2018). For this case, minifrac testing results confirmed that the vertical stress was the minimum stress. Without minifrac results to constrain the minimum horizontal stress, a ratio of horizontal to vertical total stress must be assumed. To reflect the overconsolidated nature of the Clearwater clay shale, a typical stress ratio for this area (Total E&P Canada Ltd., 2007) was used to find the minimum horizontal stress as follows:

$$\frac{\sigma_h}{\sigma_v} = 1.15; \tag{2.2}$$

Consequently,

$$\sigma_h = 1.15 \times 3800\ kPa = 4370\ kPa.; \tag{2.3}$$

The maximum horizontal stress S_H is challenging to compute without specific field data (e.g. wellbore breakouts, etc.) so was estimated using regional values suggested by the Alberta Energy Regulator (2010). For this well location, a ratio of S_H/ S_v of 1.4 was suggested (Energy Resources Conservation Board, 2010) and consequently:

$$\sigma_H = 1.4 \times 3800kPa = 5320\ kPa. \tag{2.4}$$

Therefore, the confining stress for the tests was calculated as the average of the three principal stresses:

$$\sigma_m = \frac{3800 + 4370 + 5320}{3} = 4497\ kPa \tag{2.5}$$

Lastly, the pore pressure used in the tests was obtained from the Annual Performance Presentation of the field.

Figure *2.2* illustrates different pore pressure measurements that were taken for neighbouring wells in the same field. These measurements show how McMurray Formation is underpressurized with respect to the overlying formations. Taking into account that the samples used in this research were located at the bottom of Clearwater Formation, the pore pressure used for testing is taken from

Figure *2.2* where it can be observed that there is hydraulic isolation between the reservoir and the caprock. Consequently, the pore pressure value assumed for testing was taken as the one reported in Wabiskaw Formation.

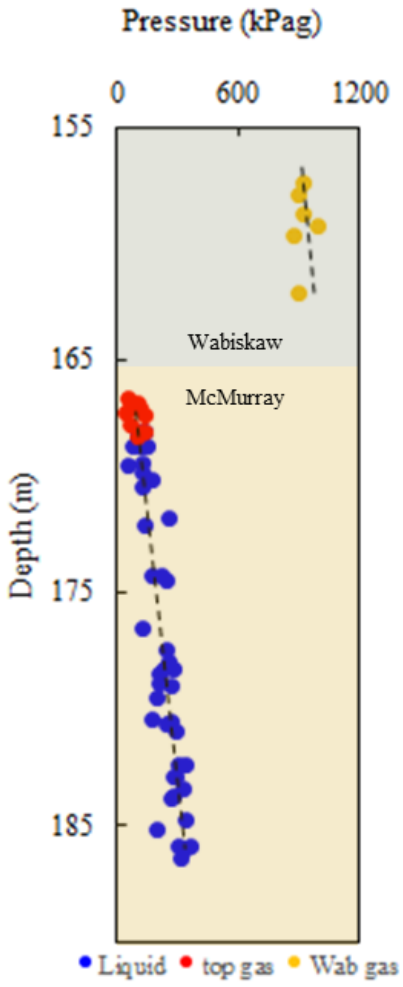

Figure 2.2: Pore pressure measurements in McMurray and Upper Wabiskaw Formations. (from Annual Performance Presentation MRP Brion 2017).

2.1.4 Well Logs and Core Selection

The cores used in the tests were obtained from the base of the Clearwater Formation, which is the section most likely to be exposed to high temperature conditions due its proximity to the steam chamber. For tests conducted in this research, samples were taken from cores that visibly had no or minimal fissures or discontinuities. Additionally, samples used in this research were selected to be representative of Clearwater shale (high Gamma Ray). Figure 2.3 shows the gamma ray log for the well and the gamma ray log over the depths of the samples. The selected section shows a very homogeneous gamma ray value through the tested section, which is close to 100° API. This is in good agreement with the AER requirements for caprock that states the gamma ray value must be at least 75 ° API.

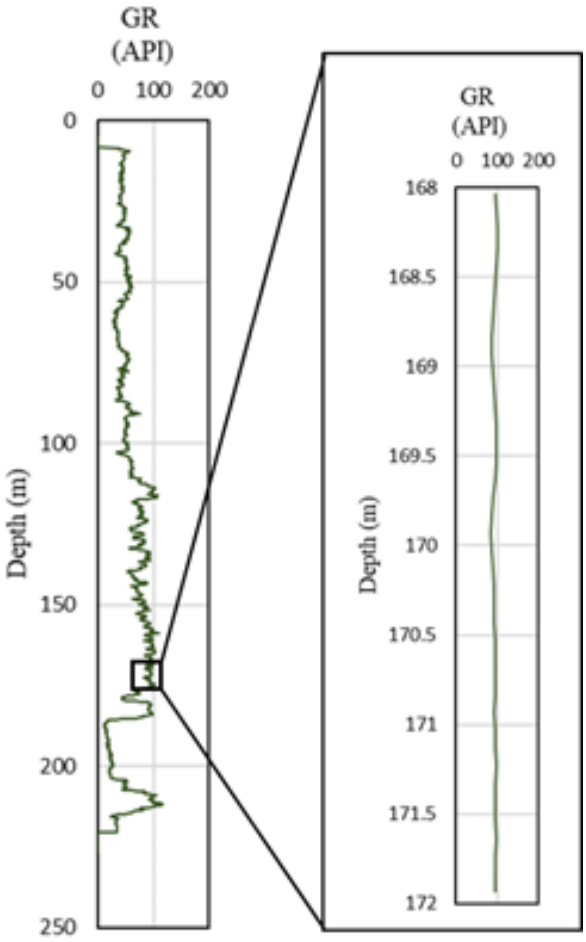

Figure 2.3: Gamma ray log for Well 6-12-90-14-W4 and for the cores used depth.

At this well location, samples were taken from drilling depths over a range from 168-171 meters. The samples taken from the deepest cores were used in the thermal testing phases of the research and slightly shallower samples were chosen for creep tests. The cores selected to perform the tests were from number 38 to number 43. The following table shows the core selection and depth for each sample.

Table 2.1: Samples Selected for Creep and Thermal Creep Testing

Well 6-12-90-14				Drilling Depth [m]		Distance from Top [m]
Sample #	Sample ID	Core #	Tube #	Top	Bottom	
38	C23T3S1	C23	T3	167.5	168.25	0.59
39	C23T4S1	C23	T4	168.25	169	0
40	C23T4S2	C23	T4	168.25	169	0.36
41	C24T1S1	C24	T1	169	169.75	0.57
42	C24T2S1	C24	T2	169.75	170.5	0.43
43	C24T3S1	C24	T3	170.5	171.25	0.03

2.2 SAMPLE PRESERVATION AND PREPARATION

Beyond the vacuum-packed and oil immersion procedure initally used to preserve the cores, the as-received cores were stored in the University of Alberta's moisture room to ensure continued preservation. Figure 2.4a shows the vacuum-packed specimen and the paint can and Figure 2.4b shows the original core as received. Each original core had cylindrical measurements of 69.85 mm (2¾") diameter and approximately 152.4 mm (6") length. Based on these dimensions, specimens were cut from the core samples with a diameter of 63.5 mm (2.5") and the ratio between the diameter and the height chosen to be 1:1. This dimension was appropriate for consistent sizing for every cell configuration and met minimum requirements for every test, such as to have an optimum drainage length assuring that the tests are performed under drained conditions. Each core was horizontally cut into two pices to the desired height using a masonry saw, in that way, each core number had sub-number, e.g. core #40 was cut into samples #40-1 and #40-2. Susbsequently, the diameter of each sample was re-cored using a press with a 2.5" cutter. Before re-packing the freshly cut samples, they were carefully examined and only the best quality material was used for the tests. Quality was assessed visually to determine that the specimens

remained intact, undisturbed and without significant fissures. It should be noted that some intact samples had non-persistent hairline fissures parallel to the bedding planes but since these were normal to the testing direction, were considered to not have an impact on the testing program. The final resulting specimens, as shown in Figure 2.5, were labeled, vacuum packed and stored again in oil cans ready for testing.

Discarded material was used to determine Clearwater clay shale index properties and mineralogical composition as well as for making reconstituted samples. For reconstituted samples, the material was finely crushed after drying, and then water was added to make a homogeneous slurry that was then consolidated. This procedure is described in detail in Chapter 3.

The preparation of the intact samples aimed to minimize sample disturbance. Following ASTM D4543-08, the material was carefully handled, and the humidity controlled at all times to avoid moisture loss at the greatest degree possible.

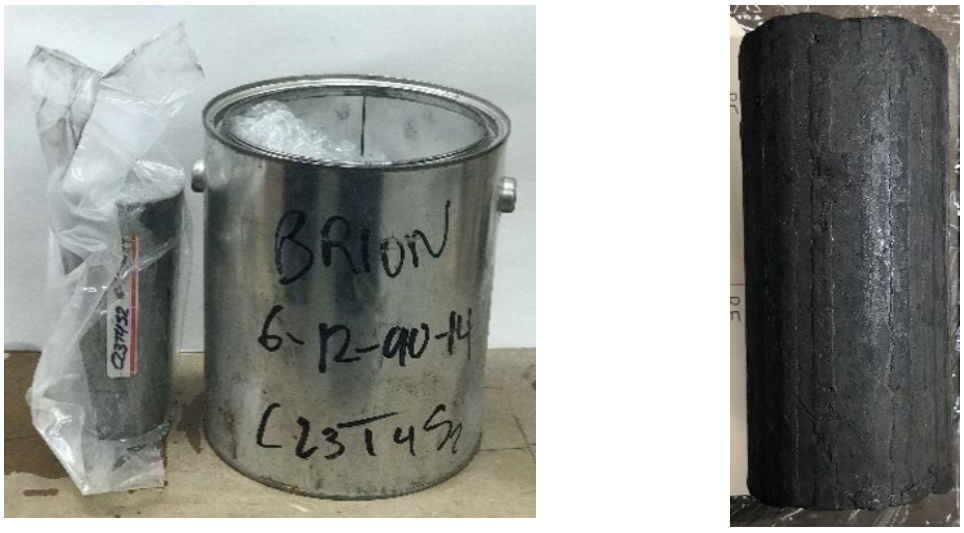

(a) (b)

Figure 2.4: Original Clearwater core: (a) vacuum packed in oil within paint can and (b) unpacked.

Figure 2.5: Intact Clearwater clay-shale sample to test.

2.3 TESTING EQUIPMENT

The primary testing equipment used for this research consists of two hydraulic oedometer cells and two isotropic cells. Each system is equipped with a computer-controlled data acquisition system that automatically process, plot and store the required data from the tests, including temperature data from different thermocouples, displacement measurements from LVDTs, pore pressure and confining pressure from the pump controller and from pressure transducers and pump volume.

Two Teledyne ISCO pumps, one for the pore pressure and one for the confining or axial pressure, depending on the cell type, are responsible for controlling the desired effective stress. Pressure transducers are installed on each line to monitor pump pressure accuracy.

Local displacements are measured with LVDT (linear variable differential transformer) devices, for the oedometer cells only one external axial LVDT is installed (Schalvitz HR-DC). For the isotropic cell tests, three Measurement Specialties MHR and MHR-T (high-temperature) series miniature LVDTs are used inside the cell, one LVDT measures the radial deformation and the other two measure axial displacement. The miniature LVDTs used have two different sizes, MHR and MHR-T 100 correspond to 8 mm displacement range and MHR and MHR-T 250 have 20 mm of optimum displacement

range. For the purposes of this study, we will call type 100 LVDTs "*short*" and type 250 LVDTs "*long*". The LVDTs used in this research are shown in Figure 2.6.

Figure 2.6: Displacement measurement devices: LVDTs Type 100 and 250.

2.3.1 Oedometer Cell

The oedometer cells used to study creep behavior consist of an aluminum cell with a stiff stainless steel consolidometer ring mounted inside the cell that holds the sample and restrains any lateral deformation. A hydraulic piston located on top of the sample is responsible for applying the axial load using pressurized silicon oil (hydraulic fluid), this piston is allowed to move freely in the vertical direction and the LVDT device responsible for recording the deformation of the sample is directly attached to the loading piston. Axial drainage is allowed through lower and upper ports since they are connected to the porous fluid lines. The fluid flowing through those lines is supplied by a reservoir containing the adequate pore fluid for each test. The stress and strain conditions are assumed to be axi-symmetric and the friction between the sample and the ring is assumed to be zero. A schematic description of the oedometer system is given in Figure 2.7. A photo of the cell is provided in Figure 2.8 and Figure 2.9 shows the oedometer cell cross sectional area and its parts.

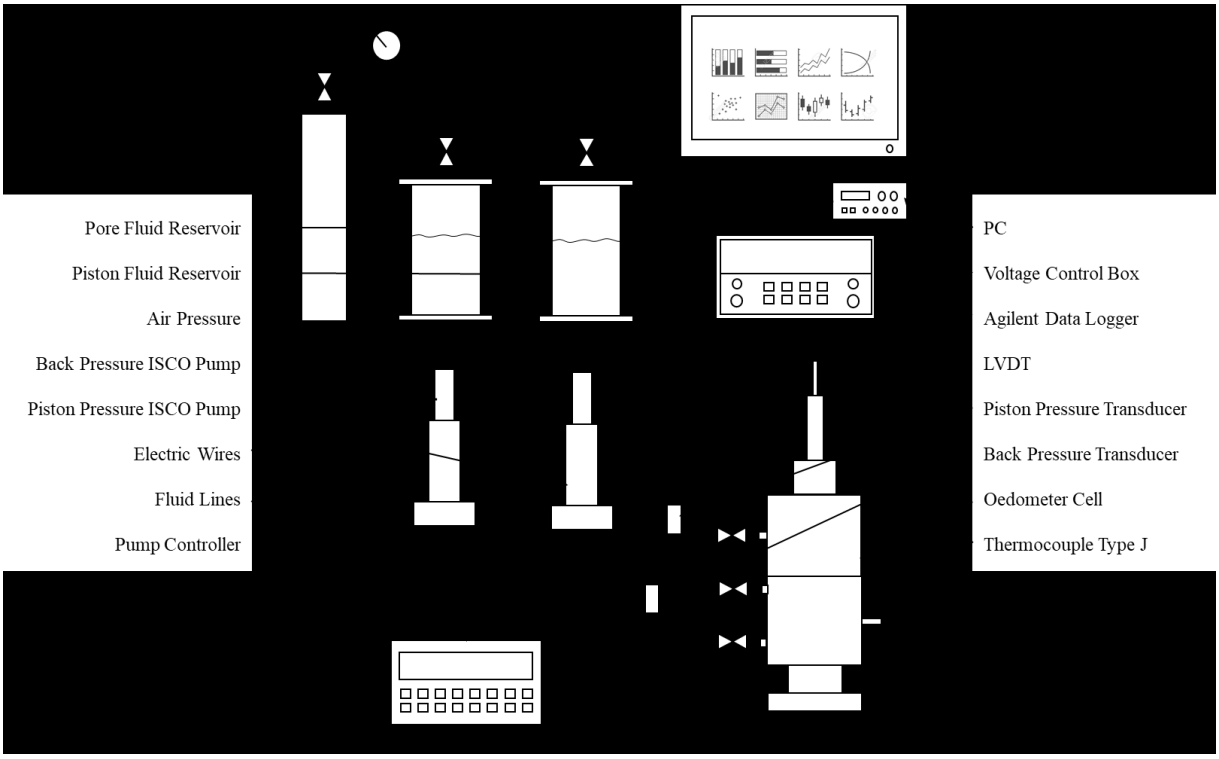

Figure 2.7: Schematic design of the oedometer system.

Figure 2.8: Oedometer Cell.

The aluminum oedometer cell described above is not suitable for very compressible material like a high-water content slurry since the maximum piston displacement allowance is about 5 cm. On the other hand, it requires placing a spacer on top of the testing material, so, if small load-deformation measurement (below 1 MPa) is required, the large oedometer cell will not have the accuracy to correctly measure such deformation. For this reason, a conventional oedometer ring is used to test slurry (reconstituted) material.

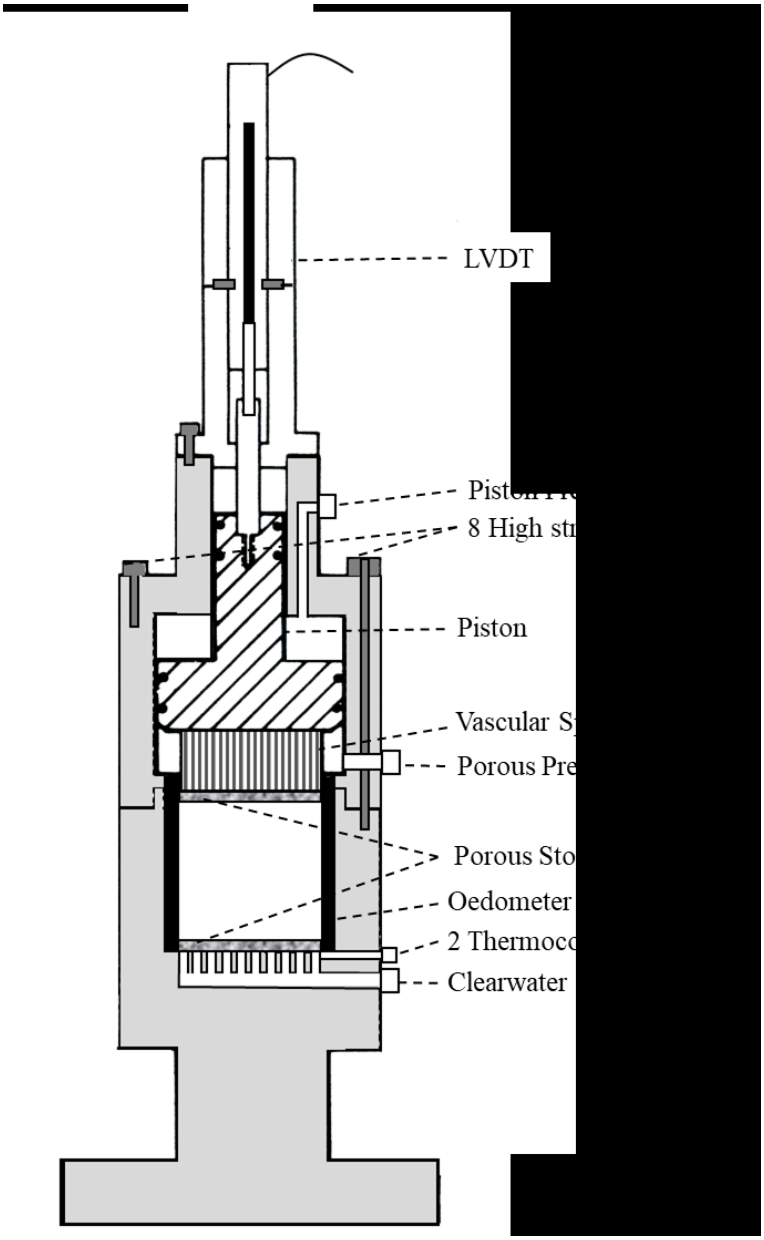

Figure 2.9: Cross sectional area and parts of oedometer cell.

2.3.2 High Temperature Oedometer System

The two high-temperature oedometer cells were designed and constructed at the University of Alberta's Geomechanical Reservoir Experimental Facility (GeoREF). A detailed description of the cell was provided by Kosar (1989). The high temperature oedometer system uses the same aluminum cell described in §2.3.1 and but is complemented to deliver, regulate and isolate high temperatures. The cell is heated by four cartridge heaters embedded in the wall of the cell, around the perimeter of the sample, the heating rods are controlled by OMEGA CSi8DH temperature controller capable of heating using a RAMP function, where the operator can control the heating rate. Two type-J thermocouples are installed to monitor cell and sample temperatures. The external part of the LVDT is covered with a spiral flowing coolant fluid at 15^0C to maintain a low temperature in the measuring device. These additional features are illustrated Figure 2.11. The cell is isolated using fiberglass insulation material to prevent any damage to the adjacent equipment; it also avoids that external temperature fluctuations affect the test conditions (Figure 2.10).

Figure 2.10: Oedometer fiberglass insulation

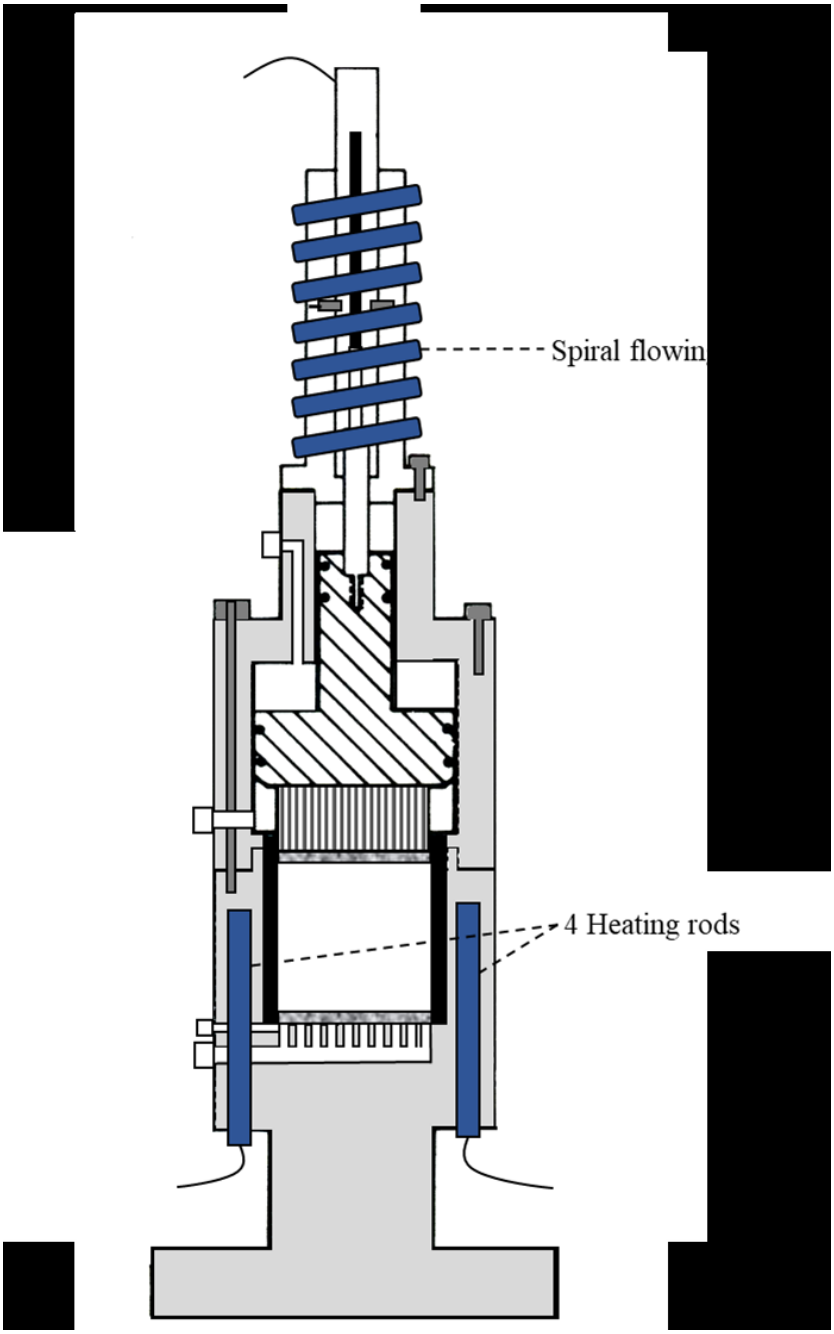

Figure 2.11: Additional oedometer features for high temperature tests

2.3.3 Isotropic System

A schematic of the setup for the isotropic testing system is shown in Figure 2.12. It is a high-pressure system consisting of one isotropic cell placed inside a heating chamber

that helps to maintain a constant temperature. The cell (Figure 2.13) is cylindrical with the outer wall threaded to the base plate where the sample pedestal is placed, it was developed at the University of Alberta and is further described in Deisman et al. (2011). A latex membrane is placed around the sample to prevent communication between pore and confining fluids. Drainage of the sample is allowed from the bottom pedestal and the top cap, which are connected to the external lines through pressure sealed fittings in the base; these lines also permit to apply pore pressure. Three ISCO pumps control pressures inside the cell, two for pore pressure and one for confining pressure. The volumetric change of the sample is measured by three LVDT's installed inside the cell, they are connected to the data acquisition system using three ports with pin connections, the LVDT's are fixed to measure the sample deformation with an axial holder system and a radial chain, as depicted in Figure 2.14.

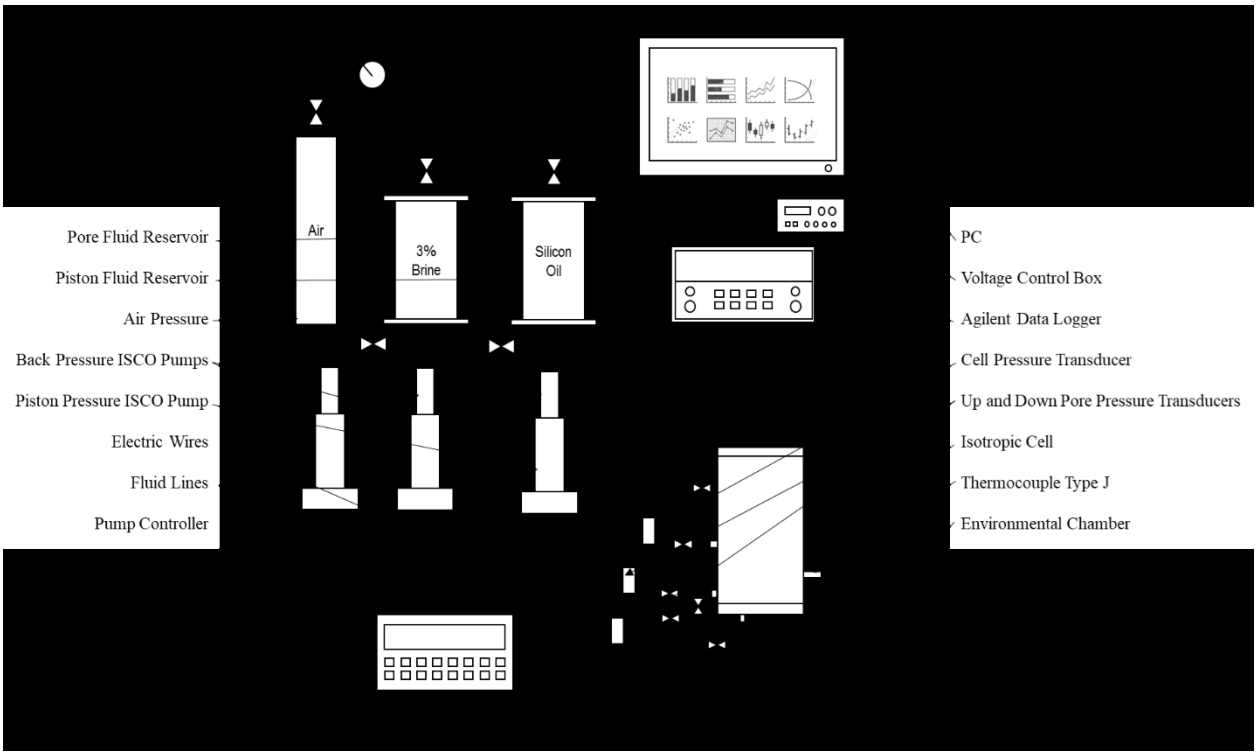

Figure 2.12: Schematic of the isotropic system.

Figure 2.13: Isotropic cell.

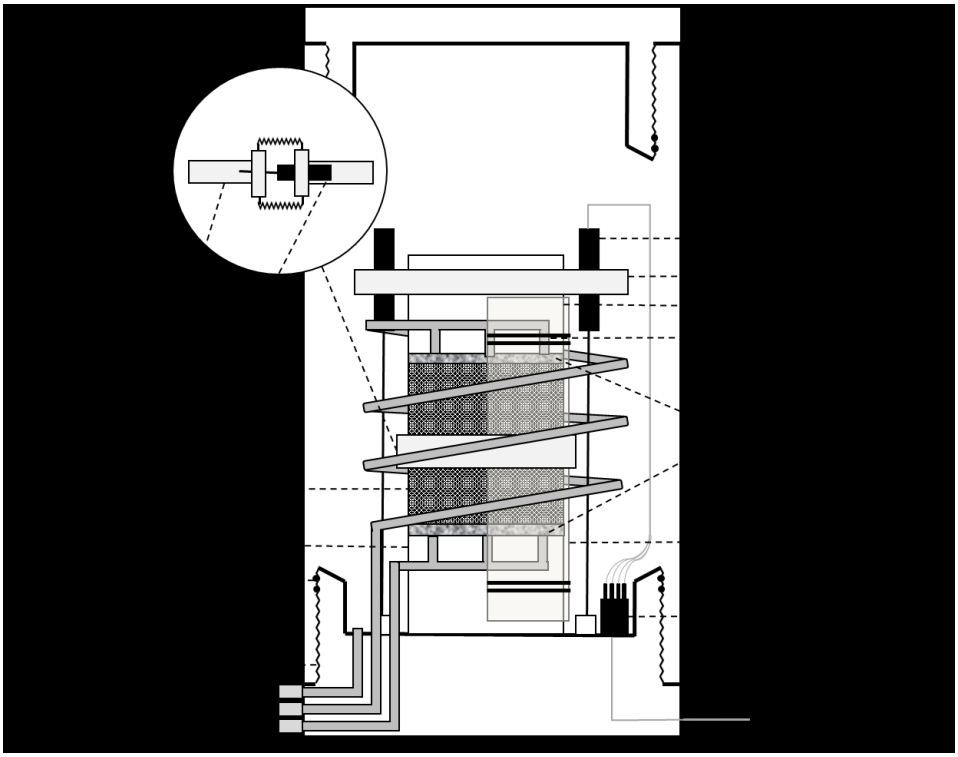

Figure 2.14: Cross section and set-up of the isotropic cell.

2.3.4 High Temperature Isotropic System

The high temperature isotropic tests use the same cell configuration as the hydrostatic cell described in §2.3.3 except for high-temperature wiring and the use of heat resistant Teflon high-temperature membranes as latex membranes are not appropriate for high temperature tests. This cell can sustain temperatures up to 300°C that can be monitored with a thermocouple capable of reading the temperature of the confining fluid inside the cell which is taken as the sample temperature. The cell is placed inside a sealed chamber responsible for heating the cell; the chamber has an integrated temperature controller system that can heat the cell using different functions, including heating rate.

2.4 EXPERIMENTAL TEST PROGRAM

The following experimental test program was designed to provide a better understanding of compression behavior of Clearwater reservoir caprock under different constant effective stresses and temperature exposure as a time dependent property of the material in its intact and reconstituted state. The clay shale cores used are adjacent to each other and share similar properties; thus, it is possible to make a comparison of the different behaviors observed between the oedometer cell and the isotropic cell. The pore fluid selected for the experiments is brine with a salinity of 3,000 ppm based on a previous experimental study carried out in the Reservoir Geomechanics Research Group ($[RG]^2$) facilities (Zadeh & Chalaturnyk, 2015).

To investigate the time dependent creep behavior and intrinsic properties of the Clearwater core, four intact and two reconstituted samples were studied using either a one-dimensional oedometer cell (§2.3.1) or an isotropic cell (§2.3.3). Two intact and one reconstituted sample were tested in each of the cells under isothermal conditions and multiple effective stress ranges: 2, 3.5, 7, and 14 MPa. The reconstituted samples were prepared from remoulded material that was initially placed in conventional oedometer devices following the ASTM D 2435 (2011) where the load was increased in steps until reaching an axial stress of 1 MPa.

The temperature effects generated by the steam chamber were studied in three intact samples; two of them were tested in the oedometer cell and one under hydrostatic conditions. For these tests, pore pressure and confining pressure were held constant at average in-situ conditions which correspond to an effective stress of 3.5 MPa. Cell temperatures were increased stepwise at a rate of 0.04°C/hour from 23 °C to 50 °C to 100 °C to 150 °C and to 180 °C in order to assure drained conditions and avoiding thermal shock that is caused by sudden temperature changes.

Through the nomenclature of each test, it is possible to identify the corresponding procedure and type of sample used. The first letter corresponds to the type of test (creep, thermal creep or reconstitution), the second letter denotes the state of the material (intact or reconstituted) and the underscore code denotes the test cell and number of test.

Table 2.2 shows the samples used in this experimental test program with their corresponding nomenclature and dimensions, where *C* stands for creep, *R* for reconstitution, *T* for thermal, *I* for intact, *Od* for oedometer and *Is* for isotropic cell.

Table 2.2: Nomenclature and dimensions of the tested samples

Sample No.	Test Id	Type of Test	Sample Condition	Apparatus/Cell	Initial Dimensions [mm, mm, g]		
					Height	Diameter	Weight
41-1	CI_Od1	Creep	Intact	Oedometer	64.40	62.72	436
40-1	CI_Od2	Creep	Intact	Oedometer	68.35	63.33	471
39-1	CI_Is1	Creep	Intact	Isotropic	70.65	63.33	484
42-1	CI_Is2	Creep	Intact	Isotropic	68.37	63.39	472
42-2	T_Od4	Thermal Creep	Intact	Oedometer	72.58	63.46	505.3
38-2	T_Od5	Thermal Creep	Intact	Oedometer	62.62	63.46	434.4
43-2	T_Is4	Thermal Creep	Intact	Isotropic	75.24	63.20	524.3
Mix 1	R_1	Consolidation	Reconstituted	Classic Oedometer			
	CR_Od3	Creep	Reconstituted	Oedometer	64.84	63.20	415.0
Mix 2	R_2	Consolidation	Reconstituted	Classic Oedometer			
	CR_Is3	Creep	Reconstituted	Isotropic	50.00	63.29	329.1

2.5 MATERIAL PROPERTIES

The initial material properties are discussed in the following this section and includes moisture content, liquid limit, specific gravity, bulk density, void ratio, scanning electron microcope (SEM) and x-ray powder diffraction (XRD). All tests were conducted following accepted ASTM standards.

2.5.1 Moisture Content and Liquid Limit

Liquid limit and moisture content tests on intact specimens were performed following a modified procedure from ASTM D4318-10 (2005) and ASTM D2216-10 (2010). Testing on the reconstituted material to obtain Clearwater slurry and samples CR_Od3 and CR_Is3 is described in Chapter 3. For all studied cores, the initial moisture contents are summarized in Table 2.3, which range between 13.7 and 15 %, with an average of 14.31% for the intact samples. The liquid limit was calculated from two different specimen mixes (mix R_1 and mix R_2) and the number of blows causing closure of the groove versus water content of both mixes showed consistency and could be fitted on the same line (Figure 2.15). The average liquid limit is 41.8% and according to Casagrande's plasticity chart and the plasticity chart of Clearwater clay shale (Zadeh, 2016), the material could be classified as medium plastic inorganic clay. These two properties were expected to be similar between all samples since they are contiguous from the same lithological division within Clearwater Shale.

Table 2.3: Moisture content of intact Clearwater samples to test and slurry for reconstitution

Sample #	36	37	38	39	40	41	42	Mix 1	Mix 2
MC [%]	15.0	14.2	14.5	14.5	14.3	14.0	13.7	51.6	50.8

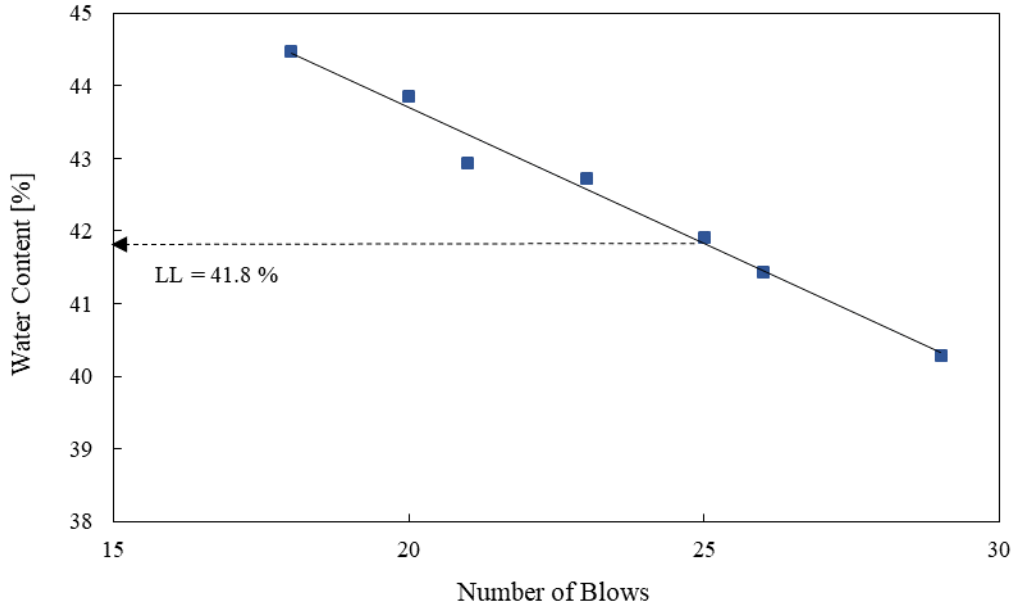

Figure 2.15: Average liquid limit of Clearwater testing material

2.5.2 Specific Gravity

The specific gravity of Clearwater clay shale was determined using a water pycnometer following the ASTM D 854-14, 2014. Soil samples from three different depths were tested with results ranging from 2.61 to 2.72 (Table 2.4). Due to the concurrent nature of testing, the precision of the results may vary with soil type, method used, and depends on the operators' judgment. Therefore, it was assumed that the final Gs used for calculations was the average of the three calculated values obtaining a value of 2.68.

Table 2.4: Specific gravity of three Clearwater cores from different depths

Sample #	Depth [m]	Gs
39	169.0	2.72
41	169.8	2.69
43	171.3	2.61

2.5.3 Void Ratio

The void ratio, e, is calculated from other basic geotechnical properties such as bulk density, specific gravity, and moisture content. Void ratio can be adequately used to represent compression properties of a material, however, initial void ratio calculation e_o is very sensitive to small variations of any of the mentioned properties, for that reason, it is recommended to use this value only as a rough reference. Table 2.5 summarizes the initial bulk density and initial void ratio of the tested samples.

Table 2.5: Bulk density and void ratio of testing samples.

		T_Od5	CI_Is1	CI_Od2	CI_Od1	CI_Is2	T_Od4	T_Is4	R_1	R_2
		38-2	39-1	40-1	41-1	42-1	42-2	43-2	Mix 1	Mix 2
ρ_{Bulk}	kg/m3	2193.3		2189.3	2189.3	2189.3	2200.8	2221.1	1716.2	1741.5
e_o	-	0.39		0.40	0.38	0.38	0.37	0.37	1.36	1.32

2.5.4 Mineralogy and Microstructure

The investigation of the mineralogy and microstructure of the samples provides the composition of the material and the structural fabric of the clay shale. Scanning electron microscooy (SEM) and X-ray diffraction (XDR) methods were used for qualitative and semi-quantitative analysis of Clearwater material used for this investigation, respectively.

2.5.4.1 Scanning Electron Microscopy (SEM)

The SEM analysis was conducted on each of the intact cores and the appearance was found to be very similar across all specimens. The SEM image shown in Figure 2.16 was taken from sample #42 and is representative of all the samples. The image shows that this clay-shale is formed by aggregates with a variety of shapes, from thin layers to nearly round bodies. A typical clay rich matrix is identified with significant amount of coarse quartz particles. From the image the presence of different clay minerals such as kaolinite aggregation in book-like structure can be recognized as well as illite. At microscopic scales, a preferred orientation of the clay aggregates is not recognized although at macroscopic scale fissures in the horizontal direction can be recognized with the naked eye.

SEM images were also taken after creep tests and thermal creep tests, in order to study how microstructure change with creep and thermal creep. Chapters 4 and 5 will address these results.

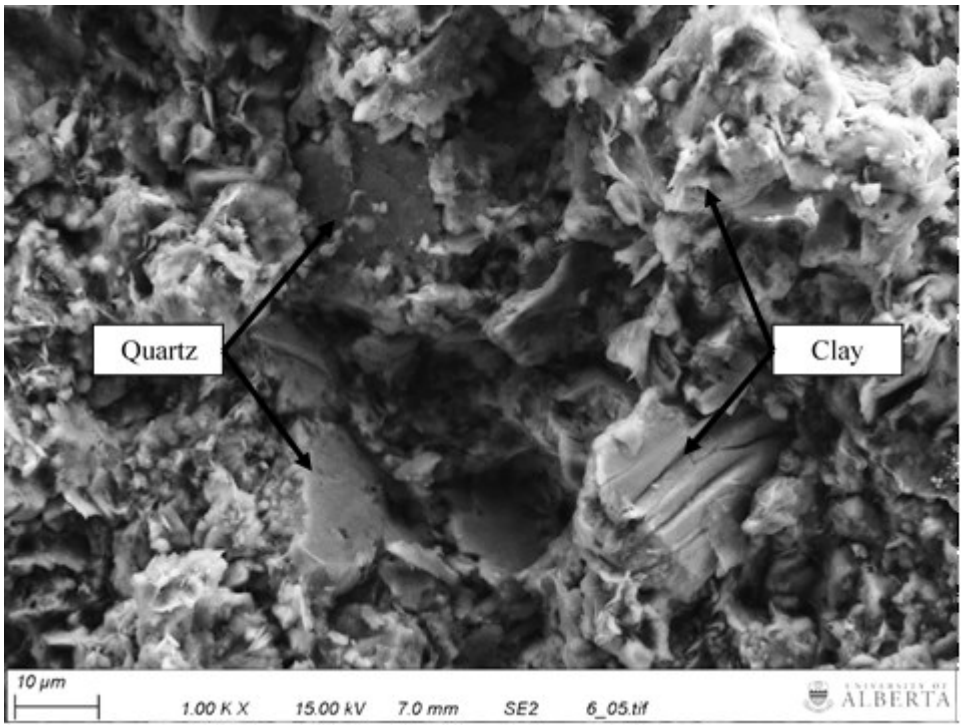

Figure 2.16: SEM image of Clearwater before test at 1000X magnification.

2.5.4.2 X-ray Diffraction (XRD)

XRD was chosen as the best available technique for the identification and quantification of minerals in Clearwater clay shale. The mineralogical composition with XRD was performed in two samples, #40 and #39. Sample #40-1 corresponds to an intact material and #38-2 was a piece of sample taken after it was exposed to compression and high temperatures. The chosen samples were sent to AGAT Laboratories to perform the test. The mineralogical composition as determined by XRD tests is illustrated in Table 2.6.

Clay fraction XRD results indicate the dominance of illite, kaolinite, and chlorite. Moderate amounts of carbonate (dolomite) and minor quantities of plagioclase feldspar are also present. The existence of significant amounts of freshwater sensitive smectite in the

after thermal creep test suggests that due to high exposing temperatures, partial clay minerals transformed to smectite.

Table 2.6: Summary of XRD analysis of Clearwater samples.

SAMPLE ID.	TYPE OF ANALYSIS	WEIGHT %	Qtz	Plag	K-Felc	Cal	Dol	Anhy	Pyr	Musc	Bar	Sider	CLAYS Kaol	Chl	Ill	ML	Smec	Total Clay
# 40 Before test	BULK FRACTION:	61.62	52	5	1	0	11	0	1	2	0	0	9	8	11	0	0	28
	CLAY FRACTION:	38.38	11	1	0	0	2	0	0	0	0	0	26	22	35	0	3	86
	BULK & CLAY	100	36	3	1	0	7	0	1	1	0	0	15	13	20	0	1	49
# 38-2 After thermal test	BULK FRACTION:	80.96	49	5	2	0	13	0	1	1	0	1	8	7	7	0	4	26
	CLAY FRACTION:	19.04	5	1	0	0	1	0	TR	0	0	TR	18	11	28	0	36	93
	BULK & CLAY	100	40	5	2	0	11	0	1	1	0	1	10	8	11	0	10	39

2.6 HIGH SENSITIVITY CALIBRATIONS

The magnitude of any expected test measurement will guide the degree of precision that will be expected from any measurement device. Based on the composition, mineralogy and type of material chosen for this testing program, it was possible to examine the compression characteristics of different Clearwater shales tested previously (Kosar, 1989; Chalaturnyk, 1992; Zadeh, 2015; Ghassemi, 2016; Oldakowski et al, 2016). It was concluded that for the creep and thermally induced strains, the expected deformation are of orders of micrometers (μm) and millimetres (mm), respectively.

Ultimately, the veracity of experimental test results rely on accurate conversions of a measurement system's electrical output to engineering units. Even if a test is rigourously designed and performed but poor calibration procedures are adopted, it will give inaccurate results or, even worse, it could lead to a false conclusion on the behavior measured in a test. For this reason, particular attention was placed on high sensitivity calibrations for this research. Experience during this research has clearly shown that every time a new test is going to be performed, it is advisable that the experimentalist execute their own calibration of the testing equipment and instrumentation used in their system with annual recalibrations being conducted, at a minimum. Old calibration and compliance test files can often be different for a new test even though the same system is used, because the electronic configuration may have changed, or the previous operator used different components in the test setup, and it is very difficult to track these details over time.

Additionally, the error tolerance could be satisfactory for previous tests, but too large for new expected value ranges.

For the tests involving temperature variations, it was also found that additional calibration considerations were required. Regrettably, some calibration issues were only found after anomalous behavior was recorded for some tests and significant effort was required to correct the experimental results. It was found that temperature variation not only affects the results due to mechanical expansion of equipment, but also due to change in electrical properties of LVDTs despite high temperature series LVDTs were used. According to François and Laloui, 2010, the calibrations required to correct miscalculations induced by temperature changes have been found to be one of the main problems faced during thermo-mechanical experimental tests. To eliminate the influence of temperature induced anomalous readings a series of calibration tests were conducted in this research, from where it was possible to obtain correction factors. Thermal compliance tests for the oedometer and isotropic cells, and thermal sensitivity tests for the LVDTs are addressed in Chapter 5.

2.6.1 High sensitivity LVDT Calibration

The linear variable differential transformer (LVDT) consists of an external barrel that corresponds to a cylindrical transformer (electrical sensor) and an internal moveable soft iron core that creates an alternating magnetic field when is moved (Figure 2.17). This excitement induces an AC voltage that is linearly proportional to the direction and magnitude of the displacement - the voltage output is zero when the core is perfectly centered between the two secondary coils (null position).

Calibrations of the LVDTs used in this research were meticulously addressed; the procedure is summarized below. It is a modification from a standard practice for calibration of linear displacement sensor systems used to measure micromotion (ASTM F2537, 2017) and it is not intended to replace, but to complement the mentioned ASTM method. Hence, ASTM F2537 should be read beforehand to follow initial protocols and to be aware of safety and technical hazards.

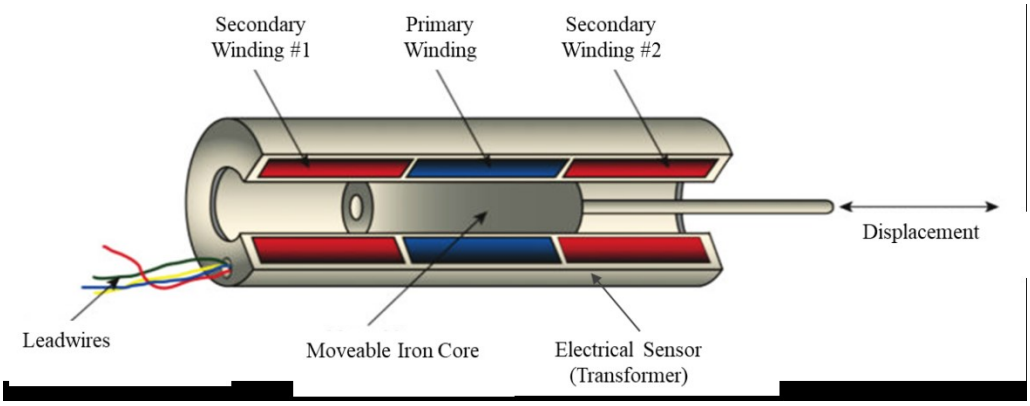

Figure 2.17: LVDT sensor scheme. Source: Honeywell International.

The calibration device used was made in $[RG]^2$ facilities and consists of a fixed dial gage with high displacement resolution (0.0001 in) and a LVDT holder, avoiding systems using Vernier or low-resolution digital calipers. The calibration starts after verifying all electronic configuration that utilize the sensor is correctly connected and tuned, including the correct voltage supply required by the LVDT and data logger reading AC volts. The proper functioning of the LVDT and the system is checked, first, the LVDT is connected to a voltmeter and the voltage range when moving the internal core between both ends of the head should the same number with opposite polarity and zero in the center. Then, the LVDT is connected to the Agilent data logger and voltage readings of the PC should be similar to those of the voltmeter.

The external head is fixed into the calibration device, the core is threaded in a nonmagnetic extension rod and it is placed at one end of the head, this position is defined as the dial gage zero displacement value; the voltage is recorded from the PC. The internal rod is then moved in small increments and the voltage and dial gage numbers are recorded. This last step is repeated until the core has reached the opposite end of the head. ASTM recommends a minimum of 10 readings, but more readings are necessary especially at both ends in order to capture the voltage where the line starts to curve. Repeat the calibration procedure starting form the end point. From the plot voltage versus displacement, it will be observed how the initial and final recorded values start to curve, this is due to the

existing electromagnetic field. Only the data in the linear working range should be used to calculate the linearity of the sensor (R^2) and the calibration factor using the slope's linear regression. Even though it is possible to include a linear regression model with intercept in the calibration file, this test provides the possibility to zero the regression intercept and it is preferable to take this approach, since in the future working with an intercept-free linear model is easier.

The two end line voltages at which the line starts to curve are recorded and are used to define the working LVDT linear ranges. The calibration factor is loaded into a new calibration file, the LVDT is fixed into the calibration device and again, voltage and displacement measurements are recorded and plotted, this will allow calculation of percent error, which is the difference between the PC displacement value (using calibration factor) and the actual measurements of displacement, over the calibrated range. If the calibration procedure is performed correctly, error will be zero or close to zero. Figure 2.18, shows and example of a calibration plot from a type 100 LVDT (8 mm of total displacement range) used in the isotropic thermal cell. The test was validated, and the percent error results are presented in Table 2.7. When it is time to test a sample, place the core in a strategical position according to the expected sample deformation, a position that allows LVDT displacement while the core remains in a centered position during the test so it will never be out of the linear voltage range.

Table 2.7: Validation of LVDT calibration

Dial Reading [in/0.0001]	Dial Reading [mm]	PC Reading [mm]	***Percent Error* [%]**
0	0.0000	-3.768	*0.00%*
403	1.0236	-2.739	*0.07%*
802	2.0371	-1.726	*0.07%*
1203	3.0556	-0.705	*0.09%*
1500	3.8100	0.044	*0.02%*
2000	5.0800	1.314	*0.02%*

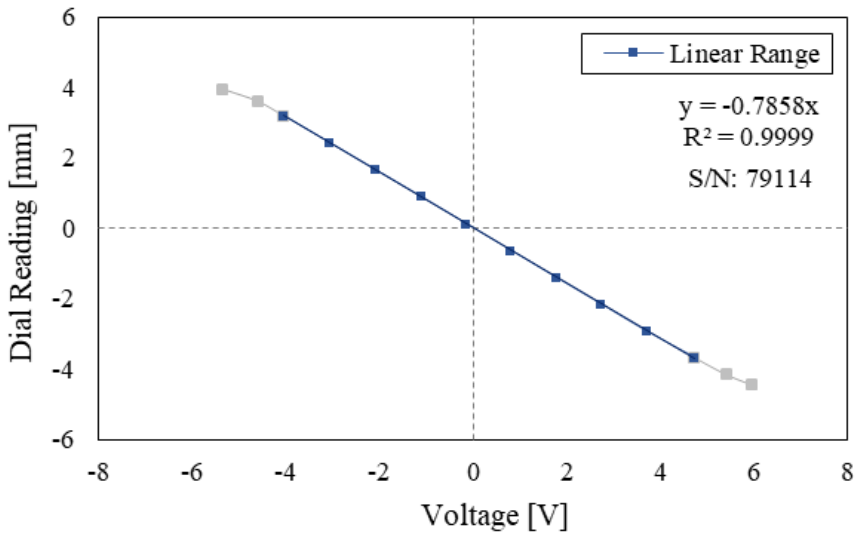

Figure 2.18: MHR-T 100 LVDT displacement calibration

CHAPTER 3: INTRINSIC PROPERTIES OF CLEARWATER

3.1 INTRODUCTION

Clearwater clay shale is an example of a soft-rock hard-soil. The mechanics of these transitional materials are complex and, at times, misunderstood since these materials are known to exhibit a wide range of behaviors, from soil to rock-like. The mechanical characteristics of constituent materials control the mechanical behavior of clay-shale, thus, it is important to have an idea of its induration, considering not only the geological history but also the diagenetic processes the material has undergone. Cementation developed in the process of lithification of clay-shales is not very strong, and the degree of induration differs significantly; this is particularly important in the case of Clearwater Formation. Clearwater was deposited over one hundred million years ago, throughout this time, the material has experienced geological and diagenetic processes that have defined its structure, where the term structure was described by Mitchell (1976) as the combination of fabric (arrangement of particles), and interparticle bonding.

According to (Burland, 1990), the compressibility of reconstituted clays is used as a basic framework for interpreting the corresponding characteristics of natural sedimentary clays. Burland (1990) named the properties of remolded or reconstituted materials "intrinsic properties" and described them as inherent to the soil and independent of the natural state. Thus, it is soil structure (fabric and bonding) that makes the difference between the properties of an intact clay and its intrinsic properties. Furthermore, ongoing experimental research at the University of Alberta (Jia, 2018) suggests that deformations

in the reservoir caused by SAGD can generate microcracks at the base of the caprock, as it is shown in Figure 3.1. Due to the pressure of the steam chamber and the low density of the steam, steam and condensate can easily flow into these microcracks (see Figure 3.2), slowly leading to a fully-softening behavior. Stark defines softening as an increase in water content due to the expansion of material particles or fissures that creates negative pore-water pressures, drawing more water into the fissures and softening the clay. Fully-softening behavior is equivalent to the behavior of remolded specimens. Thus, studying the behavior of the caprock at reconstituted conditions helps to characterize the structure of the material as well as understanding the compression behavior if a significant amount of water infiltrates it.

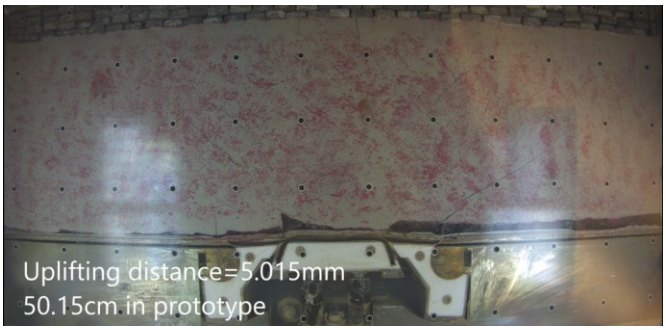

Figure 3.1: Physical modelling for caprock during SAGD using the beam centrifuge (Jia, 2018). Microcracks and the base of the caprock are generated due to reservoir expansion

In this chapter, consolidation tests are performed on intact and reconstituted Clearwater samples, and a comparison of the compressibility is made to assess the effects of material structure on caprock behavior. There is a threshold pressure above which structured materials exhibit different mechanical behaviors. Yield stress and preconsolidation pressure are not often well defined since destructuration is a gradual process, but it is crucial to identify these values. Loading pressures in this study have been selected with respect to pressures experienced by the caprock. The maximum testing pressure selected (14 MPa) was not large enough to identify a clear threshold pressure. However, destructuration was identified and the test results from intact samples together with tests from reconstituted samples provide an essential frame of reference for assessing

the in-situ state of Clearwater and the influence of structure of the natural material, increasing fundamental knowledge on Clearwater.

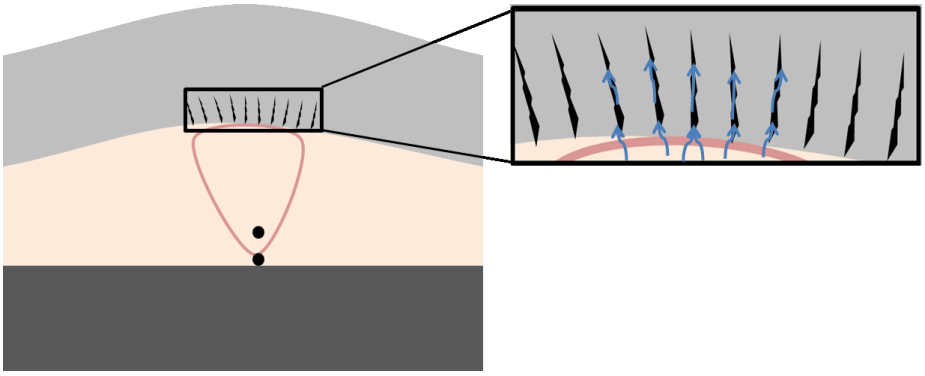

Figure 3.2 Illustration of steam and water infiltration in microcracks at the base of the caprock.

3.2 Intrinsic Properties and Structure on the Compressibility

The properties obtained from the reconstituted samples are referred to as intrinsic properties; an intrinsic property is one that is essential to the material and is independent of the physical and chemical changes that altered the characteristics of the sediment throughout its history (digenetic processes). (Burland, 1990) used the term intrinsic properties to describe reconstituted clays at a water content of between W_L and 1.5 W_L (preferably 1.25 W_L), and then consolidated under one-dimensional conditions and ideally using water with a similar composition to its natural state in order to avoid geochemical reactions. Burland (1990) also introduced the use of "void index I_v" (Figure 3.3) to normalize the void ratio in the classic compressibility curve (Terzaghi, 1925), by virtue of the fact that the void index is measured from two properties obtained directly from the laboratory through compression tests. These properties, e^*_{100} and C^*_c are referred as constants of intrinsic compressibility form the definition of I_v, as described by Equation 3.1:

$$I_v = \frac{e - e^*_{100}}{e^*_{100} - e^*_{1000}} = \frac{e - e^*_{100}}{C^*_c} \quad (3.1)$$

where:

I_v: Void index;

e: Void ratio;

e^*_{100}: Intrinsic void ratio corresponding to σ_v'=100 kPa; and

e^*_{1000}: Intrinsic void ratio corresponding to σ_v'=1000 kPa.

The intrinsic compression curve (ICL) obtained in the normalized compression plot $I_v - \log \sigma'_v$ is a unique line for a wide range of materials. It is not affected significantly by using different water contents for the reconstitution at effective stresses higher than 100 kPa and it is not influenced by the load increment duration (Leonads & Ramiah, 1956). It is also possible to obtain a normalized compression curve for natural materials taking advantage of the void index. In fact, Burland (1990) normalized individual sedimentation compression curves of normally consolidated clays from the sites considered by Skempton (1970) and concluded that they lie in a clearly defined continuous band. Burland (1990) called the regression line from this band the sedimentation compression line (SCL). ICL and SCL are initially parallel but tend to converge at pressures above 1 MPa. The observed difference was attributed to the structure that has developed in natural soils over natural deposition time. As fabric and bonding develop, the soil skeleton strengthens. This new line (SCL) is not a fundamental line because it depends on depositional conditions but is a useful reference soil behavior.

The term structure refers to the composition, arrangement of the soil particles (soil fabric), and the forces between particles (bonding) (Mitchell & Soga, 2005). Cotecchia & Chandler (2000) suggested that the structure of clays resulting from geological history can be distinguished as a sedimentation structure or post-sedimentation structure. The difference relies on whether the structure was developed solely from normal consolidation

or if it was developed from geological processes after normal consolidation. The subsequent processes correspond to mechanical unloading, creep, thixotropic hardening, bonding, overall, diagenesis. Mechanical unloading, however, is usually separated and identified in terms of over-consolidation (Burland, 1990; Cotecchia & Chandler, 2000; Leonards & Ramiah, 1959) where preconsolidation pressure σ_p' corresponds to the maximum past pressure. This preconsolidation pressure σ_p' is not necessarily the yield point where substantial deformation starts to happen in a material. If the material has developed structure from diagenesis, the yield pressure will be higher than σ_p'.

For over-consolidated clays, such as Clearwater formation, the ICL and SCL are of significant use to assess an approximate degree of over-consolidation and the influence of structure on the compression behavior.

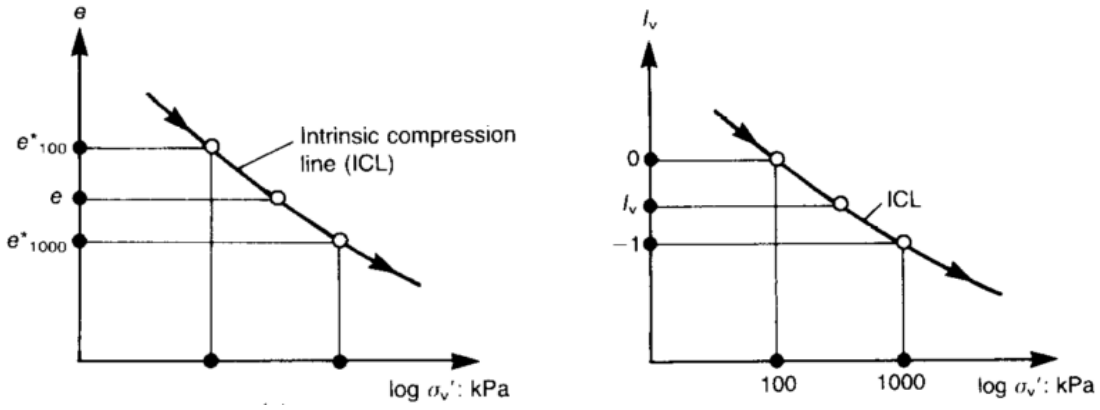

Figure 3.3. The use of void index Iv to normalize intrinsic compression curve. (a) compression curve, (b) normalized compression curve. Burland (1990)

3.3 EXPERIMENTAL METHODS

The Clearwater material crushed and reconstituted in this research was retrieved from Clearwater Formation at the Mackay River Project, as discussed in Chapter 2. Currently, there is no an international standard for the preparation of the reconstituted samples. Therefore, Burland (1990), Cepeda-Diaz & Mesri (1986) and Castellanos (2013)

techniques will be used as a baseline for the purpose of this study. In the following section, the reconstitution process used in this research is presented.

3.3.1 Reconstitution Procedure

Reconstitution procedure involves subjecting the clay to processes that aim to 'destroy' its structure in order to have a material that is independent of its stress history and structure. Different sample preparation techniques have been used to measure index properties, and the main difference they have is the level of disaggregation achieved during sample preparation. In general, a higher degree of disaggregation results in lower fully-softened strength and higher index properties (LaGatta, 1970; Townsend and Banks, 1974; Stark, 1995; Stark et. al, 2005). It is important to determine the appropriate sample-processing method in accordance with the degree of induration and the level of particle disaggregation desired. The processing should not break down or reduce the quantity of silt and coarse-grained particles in the representative sample (Stark, 2016). Ball milling is not used for these materials because it would change the texture and gradation of the soil (Stark et al., 2005). The methodology used in this research is explained in detail below:

1) Breaking and crushing: With the aid of a hammer, the intact sample was broken into small pieces. Then, the broken material was crushed to a smaller particle size using a mortar and pestle. The material was fully dry. Finally, the resulting material was crushed again using a mortar and pestle until all the particles passed through the #40 sieve.

2) Soaking: the crushed material was soaked in a mix of in site-specific water and distilled water and was taken to the moisture room for 48 hours, allowing appropriate hydration time.

3) Blenderizing: The soil-water slurry was blenderized without interruption for 15-20 minutes to create a homogeneous slurry. The blenderized material was placed in a moisture control room for 24 hours, for another hydration session.

4) Drying: The slurry was at a water content greatly more than desired. To reduce the water content of the slurry, it was allowed to air dry to near liquid limit. Airflow was controlled, and the mass was stirred continuously to prevent caking.

5) Liquid limit, W_L: When thicker consistency of the material was observed, the moisture content was calculated using Casagrande's method for liquid limit. The liquid limit test method is modified from ASTM D4318-10 - Method A (Multipoint method). The sample was air-dried until the consistency required about 20 drops of the cup of the liquid limit device to close the groove (a water content slightly higher than the liquid limit value). If over dried, the sample was hydrated again by adding water. In this method, the water content is decreasing, and the number of blows increasing, opposing the decreasing blows in ASTM D4318-10. A plot of water content WC vs. N is used to find the water content corresponding to the intersection of the line with 25 drops.

6) Burland W_L: Following Burland's (1990) recommendations, the soil should be reconstituted to a water content of 1.5-1.25 WL. Preferably 1.25 WL to facilitate the consolidation process. After water content at the liquid limit was measured, the required amount of water that should be added to the current slurry state in order to obtain 1.25 WL was estimated and added.

7) Final Hydration: After remolding the material at the desired water content, it was allowed to hydrate in a high humidity room for 24 hours to ensure the fine-grained particles have sufficient time to absorb as much water as desired.

8) Consolidation: The remolded Clearwater material depicted in Figure 3.4 was ready to proceed with consolidation tests.

Figure 3.4: Clearwater remolded at 1.5 W_L.

3.3.2 Compression Tests

3.3.2.1 Low-Pressure Oedometer Tests

The slurry obtained from the reconstitution process was allowed to consolidate in a conventional consolidometer following ASTM D 2435 – 96, where low pressures can be applied accurately. The big oedometer cells (Chapter 2) were not used for this procedure since small pressures, and high deformations are not possible in these cells. The loads were applied to the piston in increments and the slurry was consolidated. The final target effective consolidation stress σ_v' was 1000 kPa to obtain the intrinsic compression line, e_{100}^*, and C_c^* values for Clearwater. Figure 3.5 shows some samples retrieved from the consolidometer after a test.

Figure 3.5: Reconstituted sample loaded to σ'_v = 1 MPa.

3.3.2.2 High-Pressure Oedometer and Isotropic Tests

Solid samples obtained from low-pressure oedometer tests (Figure 3.5) were immediately and carefully transferred to the big oedometer (§2.3.1) and the isotropic cell (§2.2.3) to perform CR_Od3 and CR_Is3 consolidation tests using effective stress pressures from 1 MPa to 14 MPa and in-situ pore pressure of 1 MPa. Figure 3.6 shows the sample obtained after CR_Od3 test. Before starting the tests, both systems were calibrated and tested. The samples were weighed, photographed, and measured. The measurements of all samples are shown in

Table 2.2.

For the oedometer test, the sample was placed inside a ring having the same internal diameter with de-aired wet porous stones and filter paper placed on top and bottom of the sample. The cell lines were saturated with saline pore fluid (3000 ppm), and then the cell

was immediately closed. System lines were also saturated and connected to the cell. The data logging system was set. Oedometer piston load/pressure was calculated from the ram, piston, and sample area dimensions.

In-situ pore pressure was applied, while keeping an effective stress of at least 200 kPa. The sample was recompressed to 1 MPa. Then, the computed piston pressure for the first effective stress stage (2 MPa) was applied. The specimen was allowed to consolidate and creep under double drainage conditions permitting dissipation of the excess pore pressure. Once the excess pore pressure has dissipated, the primary consolidation ends. From this point, if the sample continues deforming under constant applied stress, the creep stage or secondary consolidation curve is attained. Axial (volumetric) deformation was recorded, and the sample was allowed to deform until substantial creep was observed, the next load was applied following the same procedure, and so on. Samples were loaded in increments to 1, 2, 3.5, 7, and 14 MPa effective stress using a nearly constant loading rate.

The isotropic multi-stage tests are conducted in a triaxial cell under isotropic stress conditions, where the cylindrical sample can be subjected to the same pressure all-around before starting the test, the system was air vacuumed, and the lines were saturated with pore fluid and white oil for the pore pressure and cell pressure, respectively. Each specimen was fixed between saturated porous stones, the pedestal, and top cap using a latex membrane, and sealed using Viton O-rings, as showed in Figure 2.1.17: Cross-section and set-up of the isotropic cell, experiencing drainage on both ends. The mounting system of the LVDTs was installed, and the devices were connected and placed above zero voltage position since the sample is expected to contract, thus, it is ideal to have the LVDT core as centered as possible. A full schematic of the system was shown in Figure 2.1.15. The cell lines were saturated with saline pore fluid, and the cell was connected to the system and filled with white oil. The sample was set-up and ready to start the saturation and compression phase. The Skempton's B parameter was measured until the value was close to 1. Incremental isotropic loads were applied to the specimen, and drainage was allowed from both ends until significant creep deformation was observed during each stage.

Figure 3.6: Reconstituted sample after CR_Od3 test.

3.4 EXPERIMENTAL RESULTS AND DISCUSSION

Figure 3.7 shows the normalized compression curves of void index versus effective stress $I_v - \log \sigma'$ of the intact and reconstituted samples. These curves were compared with the intrinsic compression line ICL and sedimentation compression line SCL presented in Burland (1990).

3.4.1 Intrinsic Compression Curve

Compression results of low-pressure consolidation tests on remolded material are shown in Table 3.1. The intrinsic parameters e^*_{100}, e^*_{1000}, C^*_c, and C^*_s were obtained for Clearwater material and are reported in Table 3.2. Before test slurry is showed in Figure 3.4. and after-test specimens are shown in Figure 3.6. Then, compression curves are normalized using I_v. Extensive results (Burland, 1990) demonstrate that all clays follow the intrinsic line when the structure has been completely removed, despite the water content and the mineralogical composition of the material, and Clearwater Formation material was

no exemption. As shown in Figure 3.7, the resulting intrinsic compression curve of Clearwater is in very good agreement with the results obtained by Burland (1990). Burland et al. (1996) suggested that an intrinsic swelling index, ISL, could be taken as the slope of a swelling line at an overconsolidation ratio, OCR, of 10 preferably after the soil had been consolidated to at least 1000 kPa. The Burland's intrinsic swelling index C_S^* is calculated and the ISL is shown in Figure 3.7.

The behavior of reconstituted samples tested in the large oedometer cell (CR_Od3) and the isotropic cell (CR_Is3) is analyzed for a range of stress from 100 kPa to 14000 kPa. While the test procedure allowed the samples to swell to initial stress, equipment issues resulted in the swelling data being discarded in the analysis. Swelling of CR_Od3 was discarded since the big oedometer did not allow a proper movement of the piston on the upward direction for low pressures like swelling pressure. And deformation on CR_Is3 was measured from pump volume since the radial LVDT stopped working, however, pump volume does not measure correct swelling deformations. Compression test results of CR_Od3 and CR_Is3 are shown in Figure 3.7, where it can be observed that both samples exhibited a recompression path up to 1 MPa, which was the last effective stress applied, and then joined the ICL. The similarity in behavior between the oedometer and isotropic cell shows that the position of the ICL is insensitive to test conditions. As long as the duration of each load increment is sufficiently long to allow primary consolidation, the ICL is well defined (Burland, 1990).

Table 3.1: Compression results of low-pressure consolidation tests on remolded Clearwater sample

σ'_V	e	I_v
100	0.00	0.00
250	-0.43	-0.43
500	-0.73	-0.73
1000	-1.00	-1.00

Table 3.2: Intrinsic parameters for Clearwater sample

e^*_{100}	e^*_{1000}	C_c^*	C_s^*
0.78	0.525	0.255	0.06

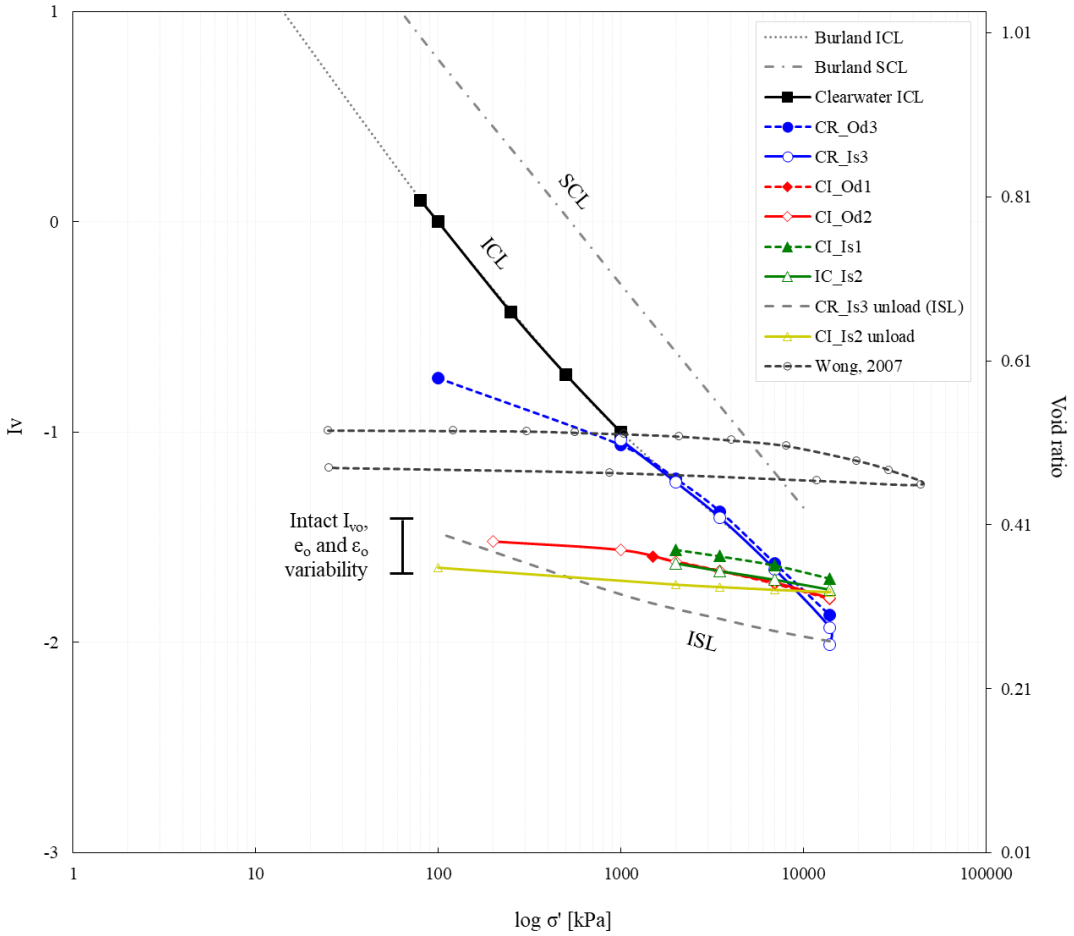

Figure 3.7: I_v normalized compression curves on intact and reconstituted Clearwater samples.

3.4.2 Structure Properties

Compression behavior of intact Clearwater samples is described in more detail in Chapter 4. For the current discussion on structure, the normalized compression curves $I_v - \log \sigma'$ for oedometer tests CI_Od1 and CI_Od2 and isotropic tests, CI_Is1 and CI_Is2, as

shown in Figure 3.7, are analyzed. The position of the in-situ effective stress on the intact compression curves, relative to the ICL and SCL provides an indication of the approximate degree of over-consolidation and structure. As shown in Figure 3.7, the oedometer and isotropic compression curves display similar behavior. The main difference between these curves is caused by the difficulty in determining the exact initial void ratio and initial water content values on intact clay-shale samples. There is inherent variability in e_o and this is why a range for I_{vo} is shown in Figure 3.7. The variance mainly affects how the degree of structure is perceived but does not affect yield stress.

Figure 3.7 shows the compression curves of intact samples relative to the position of ICL and SCL. The compression curves cross the ICL indicating the enhanced resistance of the Clearwater clay shales due to structure developed by aging (fabric and bonding). While the compression curves begin to bend slightly after crossing the ICL, the applied consolidation stresses were not high enough to determine if the curve intersects the SCL and the extent of yielding. Burland (1990) and Cotecchia and Chandler (2000) have indicated that the yield stress may be unrelated to the stress history of the material and we believe this is the case of Clearwater. Leonards (1960) recommended that the critical yield pressure is referred to as quasi-preconsolidation pressure or yield stress σ'_y, and that preconsolidation pressure σ'_p is used for magnitudes calculated by geological means (unloading). From the behavior shown in Figure 3.7, it is evident that the conventional normal consolidation line (NCL) has not been reached at 14 MPa. For hard, overconsolidated clays, the yield stress is often not well-defined (Burland 1990, 1996) since post-yield disruption, named "destructuration" by Leroueil et al (1979), is a gradual process and can require high pressures to destroy the material's structure. Usually, after yield pressure is reached, the samples follow a steeper path than the ICL and SCL, and its slope depends on the subsequent structural changes. When all the fabric has been lost, the compression curve eventually joins the ICL.

Results from a previous oedometer study for Clearwater (Gilbert, 2007) are also shown in the figure. Even though the void ratio from the sample used in that study was higher, the results are in very good agreement with the conclusion obtained from the current research showing a strong structure for Clearwater formation. Comparing the test

conditions, in the previous study a wider range of stress was applied to the sample reaching 40 MPa; the curve shows that even at such high-stress conditions, the sample does not reach the conventional normal consolidation line (NCL). The curve follows a long destructuration zone where the yield point cannot be easily identified, suggesting that the sample present high strength as explained above.

From the swelling test carried out on CI_Is2, an apparent discrepancy can be noted from the swelling curve of the reconstituted sample CR_Is3 and the intact sample; the intact sample shows a less expansive behavior than the reconstituted material. This discrepancy can be attributed to the aging and the degree of induration that the natural sample has gained through the long period of time that has been buried that is not comparable with the reconstitution of the sample. The results suggest that the material becomes stiffer and increases its strength not only by applying vertical stress but also by processes such as aging and induration that occur during the long period that the clay is buried.

The ratio c_s^*/c_s , is defined by Schmertmann (1969) as the swell sensitivity, an indicator of the fabric, and interparticle bonding that material has gained by aging. When internal structure and bonds of intact sample are destroyed, the sample exhibits a behavior similar to that of the remoulded material. Ratios above one indicate that the behavior of the material becomes increasingly influenced by fabric and interparticle bonding effects. For specimen CI_Is2, this ratio was determined to be 4.2, which indicates that the material has a strong structure even after being loaded to 14 MPa. According to these results, the Clearwater Formation material has developed strong structure not only from geological unloading but also from processes like creep and diagenesis. The above conclusion together with the position and shape of the compression curves of intact samples relative to the position of ICL and SCL, and the fact that at 14 MPa the yield stress has not been reach indicate that caprock is still a long way from experiencing these heavy destructuration conditions during SAGD. However, the material should be tested at higher effective stresses to confirm this hypothesis.

The compression studies presented in this chapter provide a valuable framework to discuss the mechanical properties of the Clearwater Formation shale specimens that are discussed in Chapter 4.

CHAPTER 4: CREEP TESTS ON CLEARWATER

4.1 INTRODUCTION

Creep behavior in geomaterials refers to the time-dependent change in structure under constant effective stress. Creep in soils has been widely studied inside the civil engineering community to inform geotechnical design challenges caused by time-dependent behavior on long-term projects, such as earth structures stability and foundations settlement. Over the past few years, the petroleum industry has increasingly gained interest in shale's creep behavior and the effects it may have on in-situ stresses, strength properties, caprock integrity, and wellbore and casing stability. A reason for this interest is the long operating periods of many petroleum-related projects; such is the case of SAGD projects in western Canada heavy-oil reservoirs.

In SAGD projects, caprock integrity assessments, required to ensure safe operation conditions, rely mainly on Clearwater caprock formation (Alberta Energy Regulator, 2016). Li and Chalaturnyk (2017) found a pronounced creep behavior in Wabiskaw member samples from the base of the Clearwater Formation while investigating its hydro-mechanical behavior. They found that long-term deformation dominated Wabiskaw clay-shale sample's behavior and that this property is less prominent in sandy-shale samples. Studies on the fundamentals of soil creep behavior (Mitchell & Soga, 2005) state that soil properties change with time, and some fundamental factors determine how significant is the creep rate for a particular geotechnical problem.

There are four main conditions that trigger creep behavior: load, material properties, temperature and time. During SAGD operations, Clearwater caprock is

subjected to effective stress changes caused by pressure and temperature changes in the reservoir. Also, Clearwater Formation clay-shale has compositional materials that have been proven to exhibit creep behavior [Fjaer, Holt, Horsrud, Raaen, & Risines (2008); Sone & Zoback (2014); M. Belmokhtar, Delage, Ghabezloo, & Conil, (2017); Cerasi et al.(2017); Rassouli & Zoback (2017)]. Furthermore, SAGD projects can operate for years so time becomes a factor in assessing creep deformations. Finally, steam is injected at elevated temperatures, and as the steam chamber reaches the caprock, it can result in thermal induced deformations, which is studied in more detail in Chapter 5. From the presence of these conditions and inspired by previous research evidence, it is postulated that creep deformation may be a significant process involved in the long-term behavior of Clearwater caprock. Understanding how the properties and stress-strain behavior of Clearwater are changing over the time while the steam chamber is active and affecting the overlying material is a significant challenge due to the lengthy testing times but remains an important area of investigation.

In this chapter, creep behavior in Clearwater is studied with a series of multi-stage creep tests on well preserved and saturated intact samples, which were described in Chapter 2. Experiments were conducted in both isotropic and oedometer cells to address the influence of stress path. The pore pressure conditions reproduce in-situ conditions, and the maximum load achieved is far above the pressure that could reach Clearwater caprock under normal thermal operations. All the tests were performed following the same steps of effective stress (2, 3.5, 7, and 14 MPa) with consistent loading rates and similar loading times. A loading rate different than the typical instant load was used on CI_Is2 to identify the effects of strain rate on creep behavior. Results from each experiment were compared to evaluate the best way to analyze and understand the time-dependent creep behavior of Clearwater for different laboratory conditions, and to find significant material properties and parameters that can be used to characterize and predict the long-term behavior of Clearwater clay-shale caprock. These experimental results have direct application to reservoir-geomechanical simulations; by using the appropriate constitutive model, it is possible to identify potential effects of creep on reservoir behavior, caprock integrity, and maximum operating pressures.

4.2 CREEP BEHAVIOR OF CLAY SHALE

According to Terzaghi's Theory of Consolidation (Terzaghi, 1923), consolidation is a process caused by a change in the effective stress of a saturated soil involving a decrease of the water content without replacement of the water by air. On this basis, consolidation ends when excess pore pressures are fully dissipated. However, when effective stress increases on a clayey specimen, the deformation of the material can continue indefinitely to establish internal equilibrium even after the effective stress becomes constant.

Compression as a result of a change in effective stress is controlled by how rapidly water can flow under a hydraulic gradient or Darcy's law and is commonly referred to as primary consolidation. The continued compression with time under constant effective stress is controlled by the rate at which the structure of the material can creep or deform at certain conditions after excess pore pressures are dissipated and is commonly referred to as secondary compression (Taylor & Merchant, 1940). This secondary compression phenomenon is associated with a viscous or creep deformation of the material structure under the action of sustained stress; it involves time-dependent rearrangement of the internal components and fabric elements toward a more stable fabric and inter-particle forces (Mesri & Feng, 2014; Mitchell & Soga, 2005). Hence, when primary consolidation takes place, the compressibility parameters $(\partial e/\partial \sigma_v')_t$ and $(\partial e/\partial t)_{\sigma_v'}$ contribute to compression; however, during secondary compression when $(d\sigma_v'/dt) = 0$, only $(\partial e/\partial t)_{\sigma_v'}$ contributes to compression and in general, primary and secondary stages are treated separately (Terzaghi, Peck, & Mesri, 1996).

The idealized relationship between deformation and logarithm of time that shows primary consolidation and secondary compression behaviors is presented in Figure 4.1. In this curve, two main sections separated by the end of primary consolidation (EOP) at time t_p can be identified. The first part reveals the primary consolidation and the second part of the curve, the secondary compression. In contrast to primary consolidation, there is no official or well-accepted theory to study the mechanics behind secondary compression of clayey materials. Nevertheless, following the concepts mentioned earlier and according to (Augustesen, Liingaard, Lade, & Asce, 2004; Mitchell & Soga, 2005), secondary

compression behavior observed during one-dimensional and triaxial drained creep tests has been recognized to represent the actual creep behavior of the soil. Thus, by letting the stress be constant for a period of time on a clay shale sample, a creeping process is initiated and the secondary compression index C_α can be computed to help characterize the material's creep behavior.

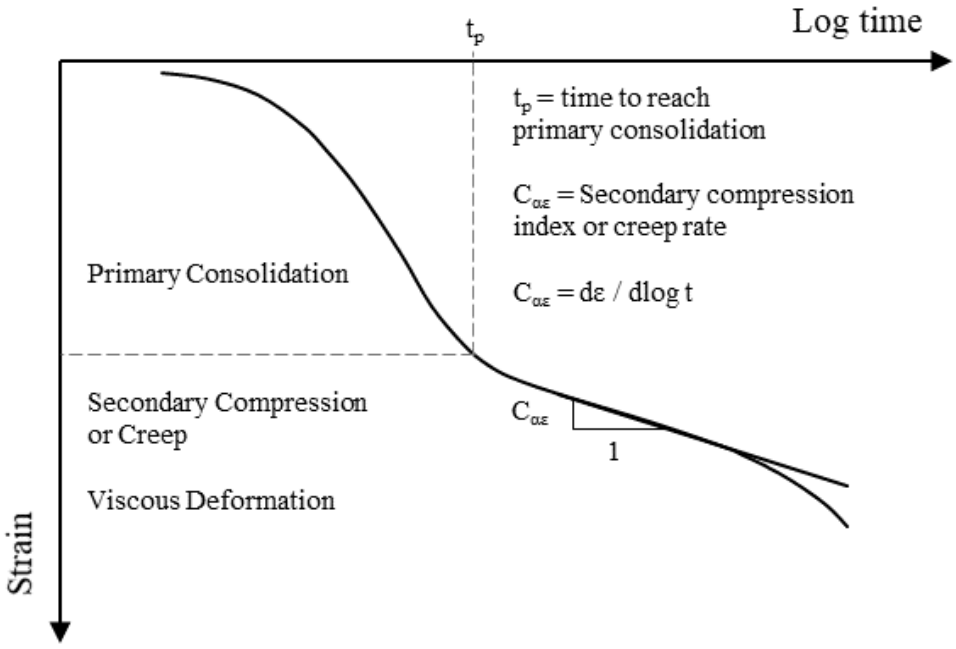

Figure 4.1: Strain-logarithm of time relationship showing primary consolidation and secondary compression

4.2.1 C_α/C_c Law of Compressibility

The C_α/C_c law of compressibility can explain the secondary compression behavior of any geotechnical material by defining a unique interrelationship between the effective stress compressibility (C_c) and time compressibility at the secondary compression phase (C_α).

Mesri et al. (1977, 1979, 1985, 2001) discovered that a unique EOP $e - \log \sigma'_v$ relation exists and describes the compression behavior of any soil under the same loading

conditions. Thus, the compression behavior of a material, if adequately calculated, is independent of the duration of primary consolidation and specimen size. This hypothesis has been continuously debated; however, Mesri (Mesri & Castro, 1987; Mesri & Choi, 1984; Mesri & Feng, 2014) has addressed most of the salient objections, explaining that important terms and concepts are incorrectly defined in most scenarios. He also proposed the C_α/C_c law of compressibility after concluding that a unique relationship exists between C_α and C_c throughout the secondary compression stage for all consolidation pressures from the recompression to the compression range. C_α can remain constant, decrease or increase with time as the tangent compression index C_c remains constant, decreases or increases with σ'_v, respectively (Mesri & Castro, 1987).

The relation of C_α/C_c together with the unique EOP $e - \log \sigma'_v$ completely explains the secondary compression behavior of any soil. This relation has been widely investigated from experimental tests (laboratory and field) and theoretical statements remaining true at any time, effective stress, and void ratio. (Mesri & Ajlouni, 1997; Mesri & Castro, 1987; Tavenas, Leroueil, La Rochelle, & Roy, 1978). The corresponding pairs of compression index and secondary compression index at any instant (e, σ'_v, t) denote the slopes of the $e - \log \sigma'_v$ and $e - \log t$ curves passing through that point. Figure 4.2, shows a graphical procedure of an increase loading consolidation test with three increasing pressures. C_α and C_c are evaluated graphically using the following designations:

$$C_a = \frac{\Delta e}{\Delta \log t} \tag{3.2}$$

$$C_c = \frac{\Delta e}{\Delta \log \sigma'_v} \tag{3.2}$$

After the C_α and C_c pairs are carefully selected, a best-fit line through the origin is plotted in a C_α versus C_c chart. The values of C_α/C_c for different geotechnical materials are shown in Table 4.1 (Terzaghi et al., 1996), where values for mudstones and shales such as Clearwater clay-shale average between 0.04 ± 0.01. It is a narrow range because the internal interparticle forces in all soil compositions are controlled by a limited set of particle interaction mechanisms. According to literature, numerous studies show that

overconsolidated soils exhibit smaller magnitude of creep than normally consolidated soils. Also, creep deformation increases as the clay content and organic content of the material increases (H Sone & Zoback, 2010).

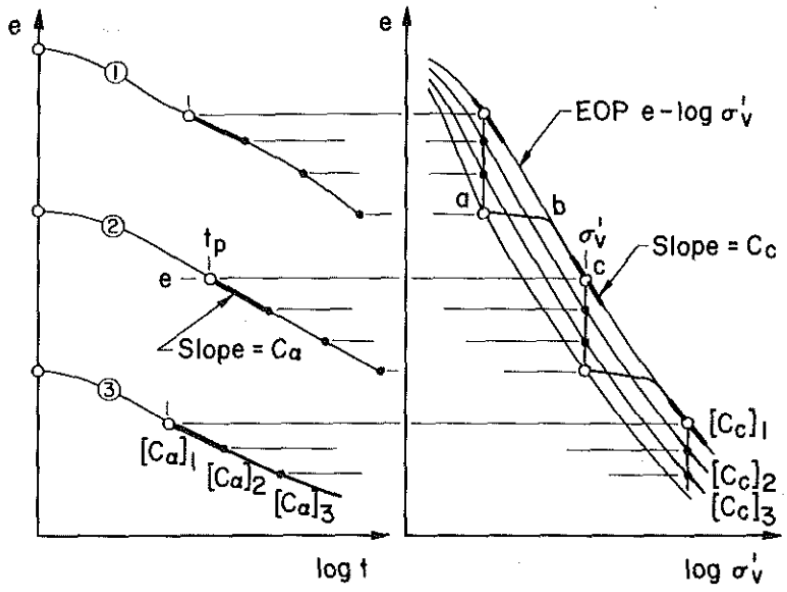

Figure 4.2. Corresponding values of C_α and C_c at any instant (e, σ'_v, t) during secondary compression (Mesri and Castro 1987).

Table 4.1. Values of C_α/C_c for geotechnical materials (Terzaghi et al. 1996).

Material	C_α/C_c
Granular soils including rockfill	0.02 ± 0.01
Shale and mudstone	0.03 ± 0.01
Inoganic clays and silts	0.04 ± 0.01
Organic clays and silts	0.05 ± 0.01
Peat and muskeh	0.06 ± 0.01

4.3 EXPERIMENTAL METHODS

4.3.1 One-Dimensional Multi-Stage Creep Tests

The one-dimensional oedometer test is a classic experiment of soil mechanics. It is the most popular procedure to test the consolidation and creep properties of soils and sedimented materials due to its convenience and reliability when it comes to predicting the in-situ behavior (1-D consolidation). The oedometer principle is to load the specimen axially while preventing lateral deformations ($\varepsilon_2 = \varepsilon_3 = 0$) and allowing axial drainage. This is known as axisymmetric strain conditions and simulates the subsurface deformation where the material is constrained laterally, similar to vertical settlements in reservoirs of a large horizontal extent. Oedometer tests assume that the friction between the walls of the apparatus and the sample is zero. Since lateral strain is prevented, the vertical strain in the oedometer, ε_a, equals the volumetric strain, ε_v. For this study, the modified oedometer cells described in Chapter 2 were used at ambient temperature using incremental effective stress steps and constant pore pressure.

Experimental Set-Up and Test Procedures

Before starting the tests, all system components were calibrated. Two intact saturated samples (41-1 and 41-2) were taken from the moisture room and carefully examined. They had some small hairline fissures in the direction of the bedding plane (horizontal), which are characteristic of shales; nonetheless, connected fissures were not present in the specimen. The samples were weighed, photographed, and the dimensions were measured (Table 2.1). They were placed inside oedometer rings of the same diameter with de-aired wet porous stones and filter paper placed on top and bottom of the sample. The cell lines were saturated with saline pore fluid (3000 ppm), and then the cell was immediately closed. System lines were also saturated and connected to the cell. The data logging system was set. Oedometer piston load/pressure was calculated from the ram, piston, and sample area dimensions.

Even though the cores were very well preserved, some moisture loss took place during sample cutting and preparation. For this reason, tests started with a saturation phase.

To saturate the samples, backpressure was applied on both ends of the specimen. The maximum possible backpressure was used, which was the in situ pore pressure (1 MPa), and low vertical effective stress (100 kPa) was maintained until pore pressure stabilized and no more pore fluid was pumped. The process took several days due to the low permeability of the samples.

The computed piston pressure for the first effective stress stage (2 MPa) was applied while the backpressure was maintained at in-situ conditions. The specimens were allowed to consolidate and creep under double drainage conditions permitting dissipation of the excess pore pressure. Once the excess pore pressure had dissipated, the primary consolidation ends. From this point, if the sample continues deforming under constant applied stress, the creep stage or secondary consolidation curve is attained.

Axial (volumetric) deformation was recorded, and the samples were allowed to deform until substantial creep was observed, the next load was applied following the same procedure, and this procedure was repeated until the test was complete. Samples were loaded in increments to 1, 2, 3.5, 7, and 14 MPa using a nearly constant loading rate. Including the saturation stage, it took an average of 100 days to complete each test.

4.3.2 Isotropic Multi-Stage Creep Tests

These tests are conducted in a triaxial cell under isotropic stress conditions, where the cylindrical sample can be subjected to the same pressure all-around. Isotropic tests are commonly used to investigate deformations since the stress state of the sample is directly controlled and known at all times, unlike the oedometer test configuration. Additionally, a local (i.e. on the specimen) measurements of volumetric strain can be computed from two axial and one radial deformation measurement devices (LVDTs).

Experimental Set-Up and Test Procedures

As in the oedometer procedure, the system was calibrated, and pressure tested before starting the set-up. The system was air vacuumed, and the lines were saturated with pore fluid and white oil for the pore pressure and cell pressure, respectively. Intact samples

number 39-1 and 42-1 were used for these tests (Table 2.1). Each specimen was fixed between saturated porous stones, the pedestal, and top cap using a latex membrane, and sealed using Viton O-rings, as shown in Figure 2.1.17. The mounting system of the LVDTs was installed, and the devices were connected and placed above zero voltage position since the sample is expected to contract, thus, it is ideal to have the LVDT core as centered as possible. A full schematic of the system is shown in Figure 2.1.15. The cell lines were saturated with saline pore fluid, and the cell was connected to the system and filled with white oil.

When the sample was set-up and ready to start the saturation and compression phase, a pore pressure of 1 MPa was applied with constant effective stress of 100 kPa until the pore pressure stabilized after 2-3 days. For isotropic conditions the Skempton's B parameter was measured until the value was close to 1, this happens when at a particular change in confining pressure, $\Delta\sigma_c$, the pore pressure, u, changes by the same amount. Both samples showed B values higher than 95%.

$$B = \frac{\Delta u}{\Delta\sigma_c} \tag{3.3}$$

Incremental isotropic loads were applied to the specimen, and drainage was allowed from both ends. An interpretation of the real data was necessary to verify that the pore pressure had been dissipated and that secondary compression was taking place. For each stage (1, 2, 3.5, 7, and 14 MPa), the sample was allowed to creep for about two weeks.

4.4 EXPERIMENTAL RESULTS AND DISCUSSION

Increase loading test results can be interpreted in terms of void ratio or strain. For creep experiments in this research, the results are presented in terms of volumetric strain due to the inherent variability of the initial void ratio e_o. Strains are calculated from direct LVDT measurements as follows:

$$\varepsilon = \frac{\Delta X}{X_o} \tag{3.4}$$

For the case of the oedometer test results, since no radial movement is allowed, the volumetric strain can be calculated directly from axial strain measurements:

$$\varepsilon_v = \varepsilon_a \tag{3.5}$$

and, for the isotropic condition, ε_v corresponds to:

$$\varepsilon_v = \varepsilon_a + 2\varepsilon_r \tag{3.6}$$

where ε_v is the volumetric strain, ε_a the axial strain, and ε_r the radial strain.

4.4.1 Creep Strain-Time Relationship

Strains for each load increment were calculated and plotted versus the logarithm of time. Volume change of stages below the in-situ effective stress condition (3.5 MPa), and especially at the beginning of the test, are not representative of the intact material behavior since they are influenced by sample disturbance during coring and handling. Sample disturbance effects are only reduced once the sample is brought to its approximate in-situ conditions. Therefore, while test results beyond 2 MPa are considered in the analyses, extra precaution is taken ensure its validity.

Nearly all of the $\varepsilon - \log t$ plots show the characteristic "s" shape curve that defines creep behavior. Thus, primary consolidation and secondary compression sections could be established after EOP. The strain and time (t_p) data was carefully identified for each loading step. From the secondary compression stage of the consolidation behavior, the secondary compression index from strain graph ($C_{\alpha\varepsilon}$) is determined graphically, as follows:

$$C_{\alpha\varepsilon} = \frac{\varepsilon}{\Delta \log t} = \frac{\Delta e}{(1 + e_i)\ \Delta \log t} = \frac{C_\alpha}{1 + e_i} \tag{3.7}$$

$C_{\alpha\varepsilon}$ can increase, decrease, or remain constant with time during a constant effective stress stage, as will be shown subsequently.

To directly compare creep strain behavior of different samples under a pressure increment from σ_j' to σ_{j+1}', the duration of secondary compression under σ_j' should be carefully controlled. It is not the total duration of the test that is important, but the duration of the test in relation to the time to reach EOP or t/t_p, as schematically illustrated in Figure 4.3. If two identical samples are being compared but one sample is allowed an arbitrary secondary compression time under σ_j' (point b), while the other is only allowed to reach EOP (point a), primary consolidation strains in σ_{j+1}' can not be directly compared. Samples starting from point b will have a shorter duration of primary consolidation and shorter strain. Therefore, misleading conclusions can be made if one is not aware of this particular feature of compression behavior. The previous arguments are based on the uniqueness EOP $\varepsilon - \log \sigma_v'$ relationship (Mesri & Choi, 1985).

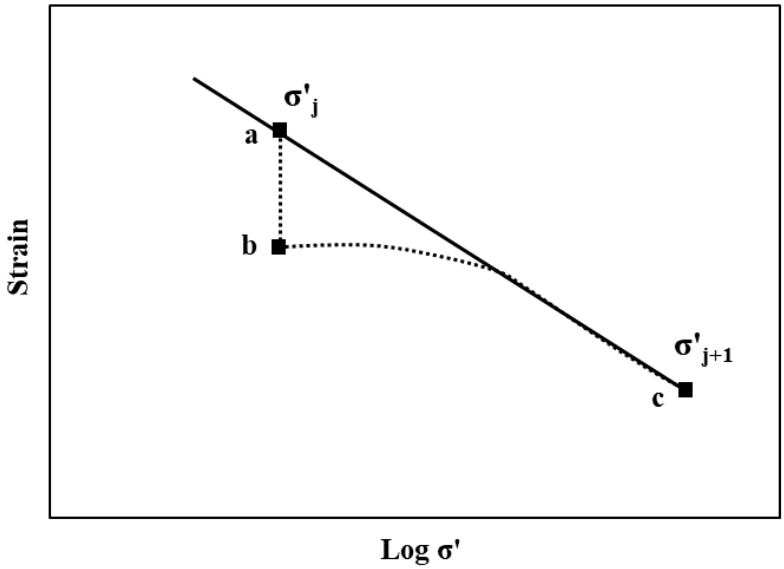

Figure 4.3: Single pressure increment and EOP.

4.4.1.1 $\varepsilon_v - \log t$ Curves from Oedometer Tests

Volumetric strain-log time plots for 2, 3.5, 7, and 14 MPa effective stress on oedometer cell tests of intact samples CI_Od1 and CI_Od2 are presented in Figure 4.5 to Figure 4.7. These figures illustrate a similar creep behavior for both samples. The EOP consolidation strains are very similar for CI_Od1 and CI_Od2 at all stress stages. As mentioned earlier, the 2 MPa data is used cautiously because this stress magnitude is lower than in-situ conditions (for the depth of the sample), and creep strains can be affected by sample disturbance. In addition, the secondary compression time for the stage prior to the 2 MPa loading stage experienced an arbitrary period of secondary compression. However, for loading stage beyond 2 MPa, the time $t/\ t_p$ is controlled, and it is possible to directly compare the results from both samples. The $\varepsilon_v - \log t$ curves from oedometer tests show a characteristic creep behavior with approximately linear trends of creep strain C_α. The C_α index exhibits a proportional behavior with the effective stress. Repeatability of results on such a complicated material as Clearwater clay shale reflects a reliable performance of the equipment and set-up used and confirms the hypothesis that all the tested samples have very similar material properties.

4.4.1.2 $\varepsilon - \log t$ Curves from Isotropic Tests

Figure 4.8 to Figure 4.11 illustrates the volumetric creep strain-time relation for isotropic creep tests performed on intact Clearwater samples. In order to study the effects of a different loading rate on the stress-strain time relationship, the loading rate of test CI_Is2 was not instantaneous as for CI_Is1 but was controlled with a slower pump flow rate until the target pressure was achieved. The results show two different "s" shape trends, where CI_Is2 exhibits a larger time to reach EOP. Note that while the $t_p{}'$s are different for each test, the EOP strains of both samples during every load increment are very similar. This will be discussed in more detail subsequently when $\varepsilon - log\ \sigma_v'$ results are introduced.

Figure 4.8 , which illustrates the behavior for the 2 MPa loading stage, clearly shows the difference in behavior between CI_Is1 and CI_ Is2. The reason for this is that before the 2 MPa load increment, each sample experienced different secondary

compression times; CI_Is1 was allowed to creep more than CI_Is2 and therefore, it shows smaller primary consolidation strain, as explained previously. Beyond the 2MPa stage, testing times were controlled to achieve consistent results creep times and directly compare strain curves of subsequent stages.

It can be seen that CI_Is2 curves tend to join CI_Is1 curves during the secondary compression section at about 1 log time cycle of CI_Is1 t_p, then, the curves start to behave with a similar trend. Results overlay and exhibit similar creep rates and even show an increase of creep rate at similar times. This means that the loading rate used on CI_Is2 caused a delayed t_p affecting the ability to detect the unique EOP strain values. However, CI_Is2 will follow similar isochrone curves to CI_Is1 beyond the unique EOP $\varepsilon - \log \sigma'_v$ (e.i: curve t/tp=10 of CI_Is1 similar to curve EOP of CI_Is2) ; this is discussed further in §4.4.2 .

Creep strain rates $C_{\alpha\varepsilon}$ for isotropic tests show an increase of magnitude with time and with effective stress for stresses higher than in-situ effective stress. After some time of secondary compression, creep rates start to increase with time dramatically; which is a typical behavior in pressure increments near the preconsolidation pressure σ'_p. However, for complex materials as Clearwater clay shales, other factors may be influencing this behavior. Special care should be taken in stress steps nearby the preconsolidation pressure since this segment corresponds to a destructuration zone where C_c drastically increases with effective stress, and consequently, C_α values are actively increasing with time. Thus, there is a tendency to overestimate C_α and to underestimate the corresponding value of C_c.Previous studies on Clearwater caprock of adjacent zones (Zadeh & Chalaturnyk, 2015) determined that the preconsolidation pressure can take values of around 6.5 MPa. The results from Chapter 3 confirm that the ranges of applied stresses in this testing program operate over the destructuration zone. In this range, just certain amount of secondary compression after EOP is required to define C_α, and C_α can not be taken as the average slope curve. This also has consequences on the corresponding C_c pair, C_c has to be determined form the slope of the tangent slightly to the right of strain at t_p (Mesri & Castro, 1987; Mesri & Choi, 1984). If this is not considered, C_α is overestimated and C_c is underestimated simultaneously, as shown in Figure 4.4

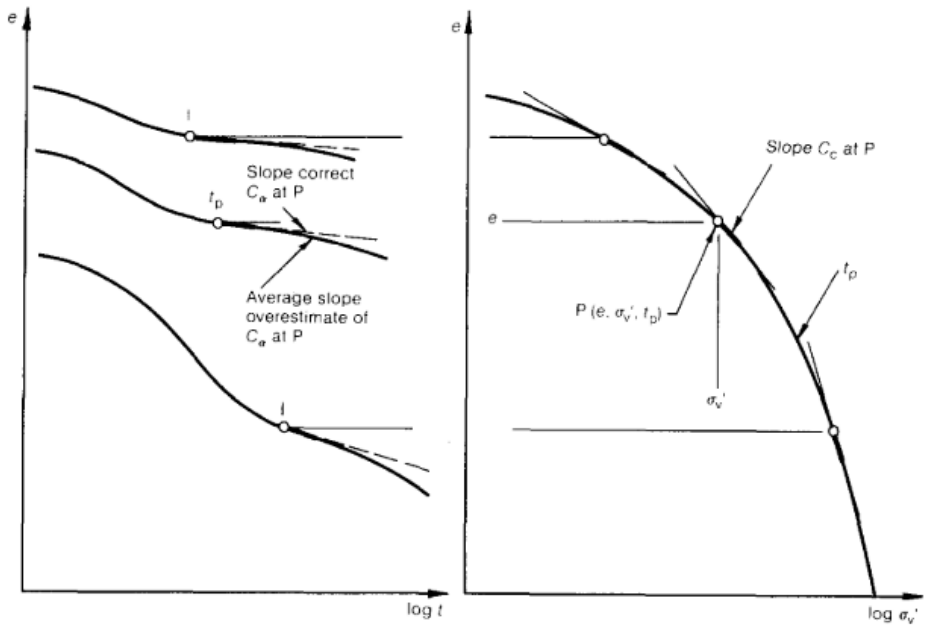

Figure 4.4: Evaluation of the corresponding values of C_α and C_c at point P (Mesri and Choi, 1984)

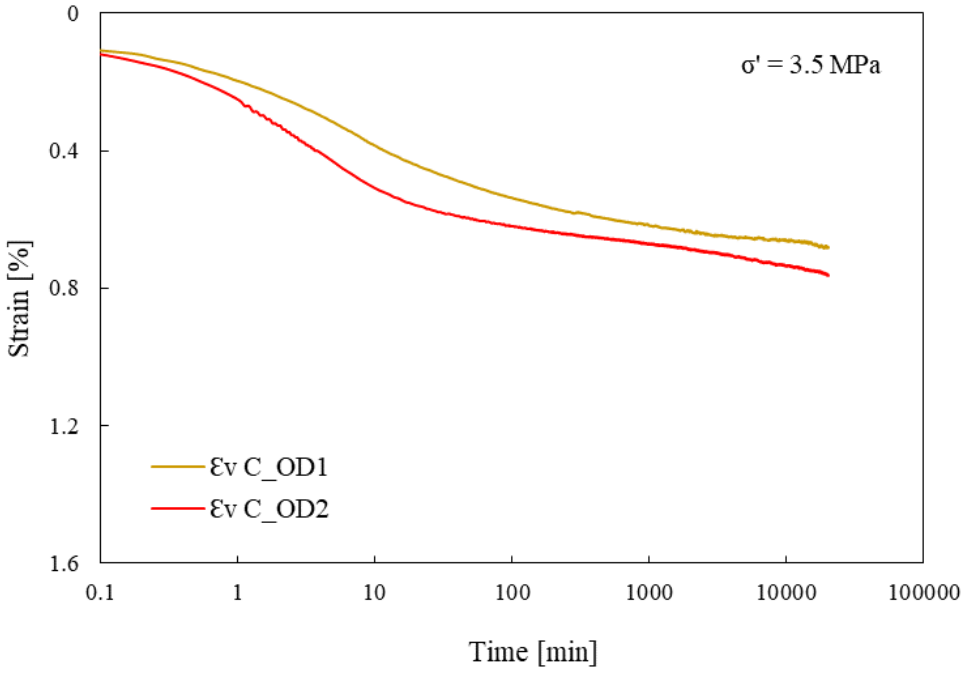

Figure 4.5: Creep strain behavior from oedometer tests at 3.5 MPa.

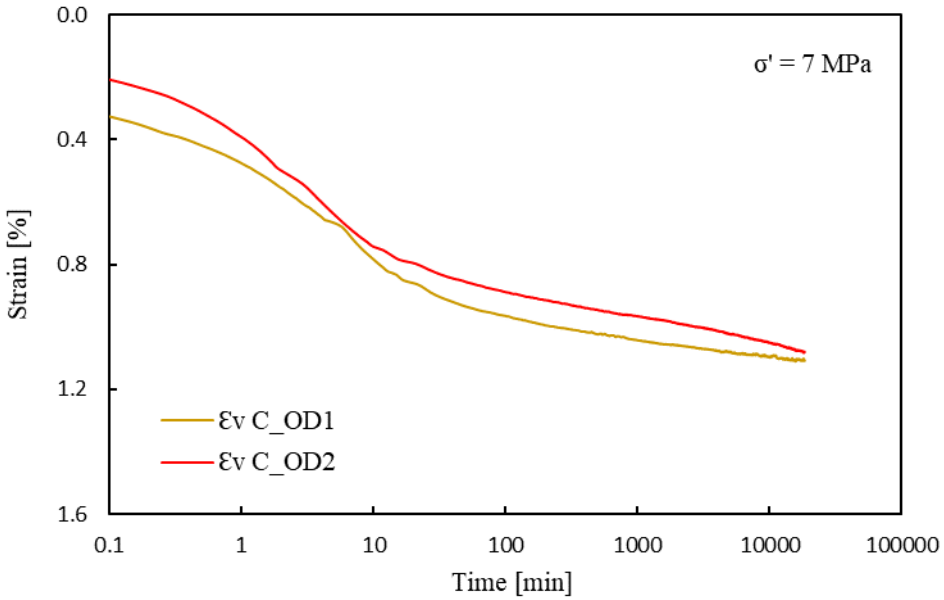

Figure 4.6: Creep strain behavior from oedometer tests at 7 MPa.

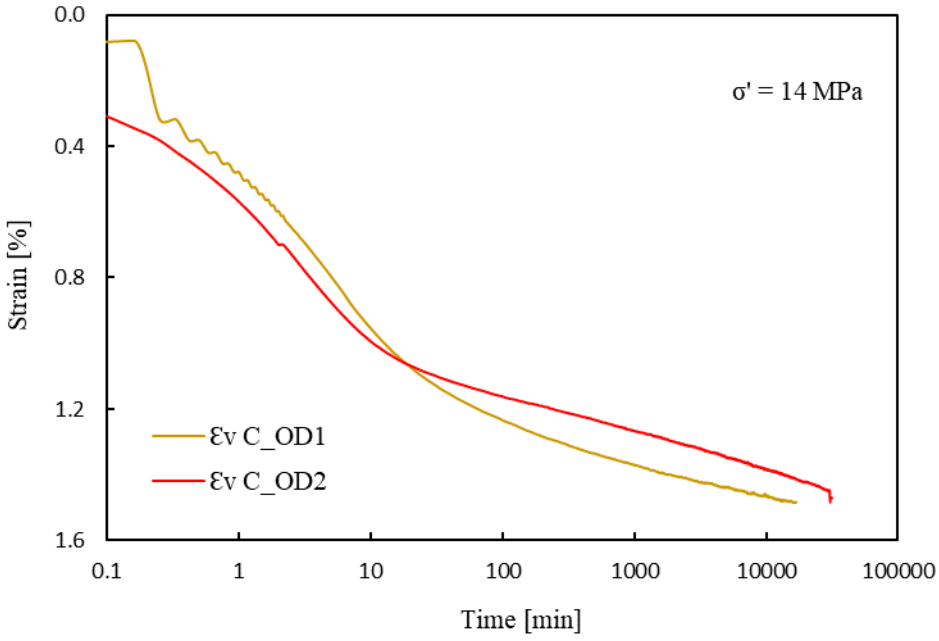

Figure 4.7: Creep strain behavior from oedometer tests at 14 MPa.

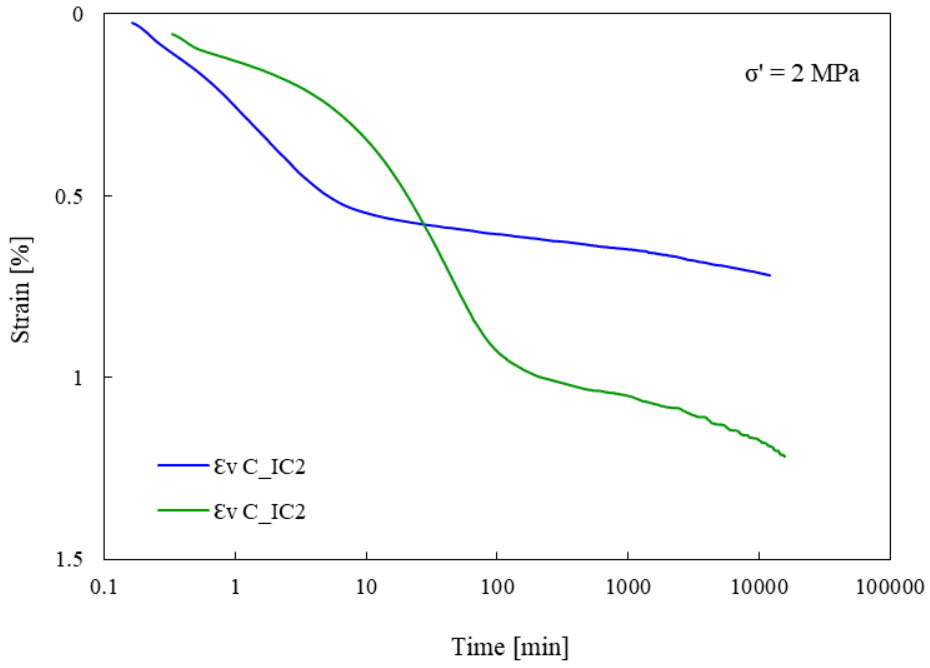

Figure 4.8: Creep strain behavior from isotropic tests at 2 MPa.

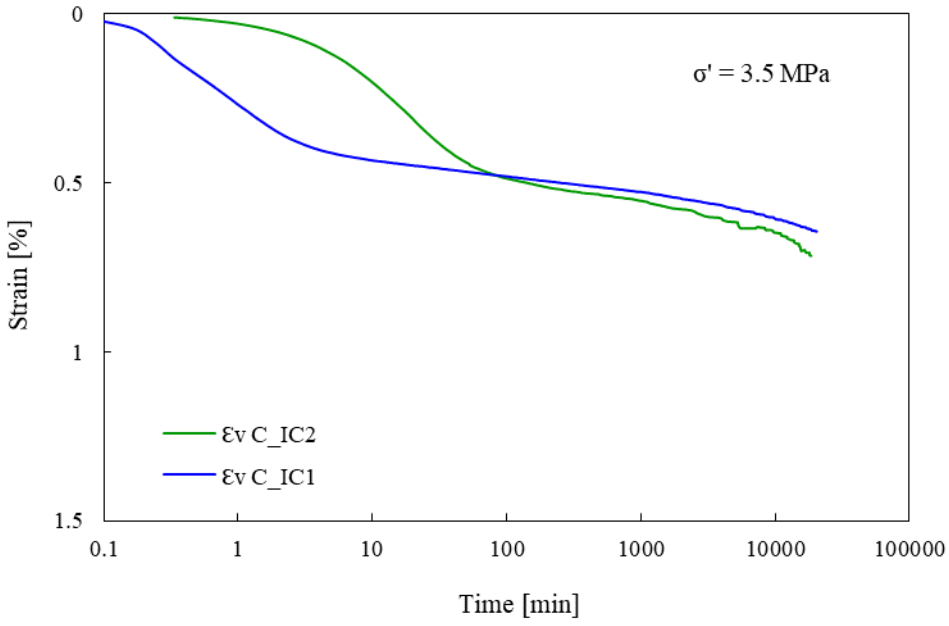

Figure 4.9: Creep strain behavior from isotropic tests at 3.5 MPa.

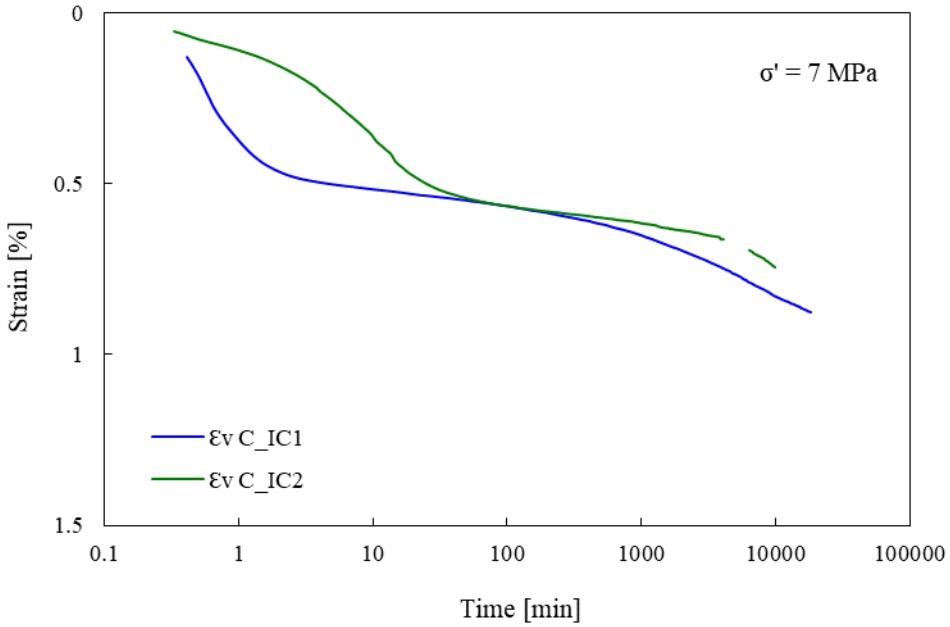

Figure 4.10: Creep strain behavior from isotropic tests at 7 MPa.

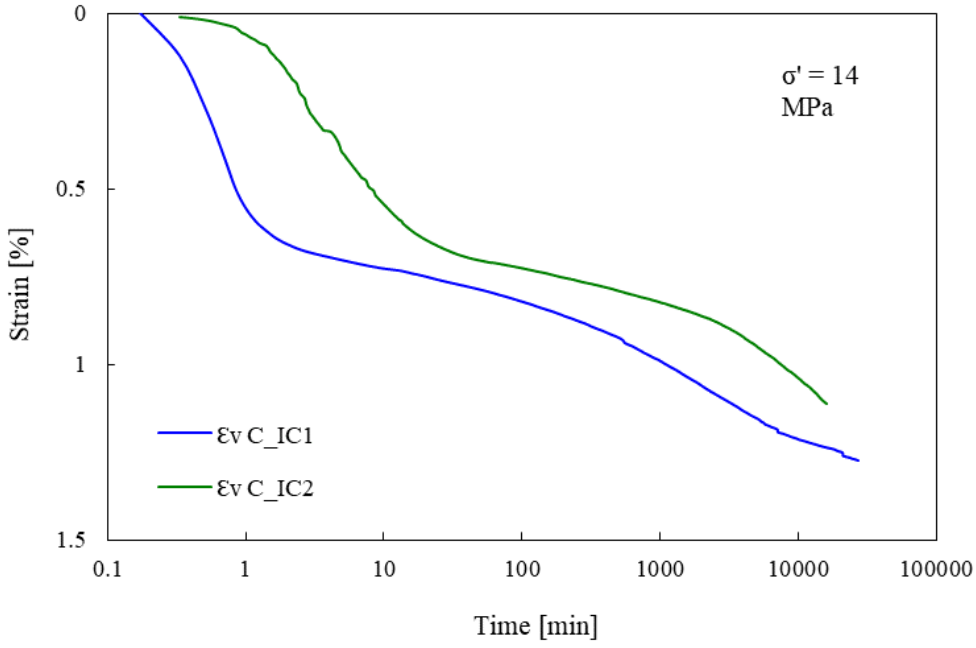

Figure 4.11: Creep strain behavior from isotropic tests at 14 MPa.

4.4.1.3 Anisotropy of Creep Behavior

Axial strain ε_a and radial strain ε_r curves of CI_Is1 and CI_Is2 for 3.5, 7, and 14 MPa are illustrated from Figure 4.12 to Figure 4.15. A significant difference between axial and radial measurements can be observed along each stage. The predominant axial deformation of the samples suggests strong anisotropic compression behavior which is likely the result of the anisotropic fabric of Clearwater clay shale. Shales are strongly anisotropic due to bedding plane distribution of material, clay mineral alignment, and natural micro-fissures creating fabric anisotropy.

From visual observations of the test samples before each test, Clearwater samples showed minor discontinuities and well defined bedding planes in the horizontal direction. This preferred horizontal orientation is also noticed in microstructural observations under scanning electron microscope (SEM). Pre-test SEM pictures are illustrated in Figure 4.16 and Figure 4.17. These images show the preferred orientation of the clay minerals while in the post-test images, clay is more randomly oriented. SEM pictures also show that the shape and size of the material that make up Clearwater vary from thin layers to round patches of different size, which becomes a source of fabric anisotropy. The initial state of Clearwater fabric or contact anisotropy seems to play a significant role in its creep deformation. The preferred direction of contact forces determines the degree of strain on each axis since contact forces act like pillar support in the structure. The vertical axis is perpendicular to the preferred direction of contact forces, which translates into a softer response compared to strains on the horizontal axis that is parallel to the preferred direction of contact forces, making it stiffer.

By comparing the radial and axial creep strains of CI_Is1 and CI_Is2, important observations are noted. First, we see that radial strain measurements are between 24% and 35% of axial strains and the difference decreases when effective stress increases. This could be explained with particle rearrangement reducing anisotropy when effective stress is increased.

As discussed before, from 3.5 MPa (in-situ conditions) the samples exhibit a transient creep behavior followed by a nonlinear region characteristic of a destructuration zone. The accelerated creep rate is more pronounced in the radial component of CI_Is2. Taking into account that CI_Is2 was exposed to a delayed compression that may have given

more time to the structure to react to the imposed load, during consolidation the material could have reoriented its anisotropic structure to a preferred direction. Considering that creep deformation greatly depends on the particular fabric and microstructural conditions of the sample, especially on anisotropy, and taking into account that CI_Is2 was exposed to a delayed compression, the difference in strain behavior of CI_Is2 and CI_Is1 during destructuration is reasonable. The results are in agreement with Kuwano (1999), who stated that radial creep strains are greater than axial strains in soils with angular particles than in soils with rounded particles due to a more anisotropic initial fabric.

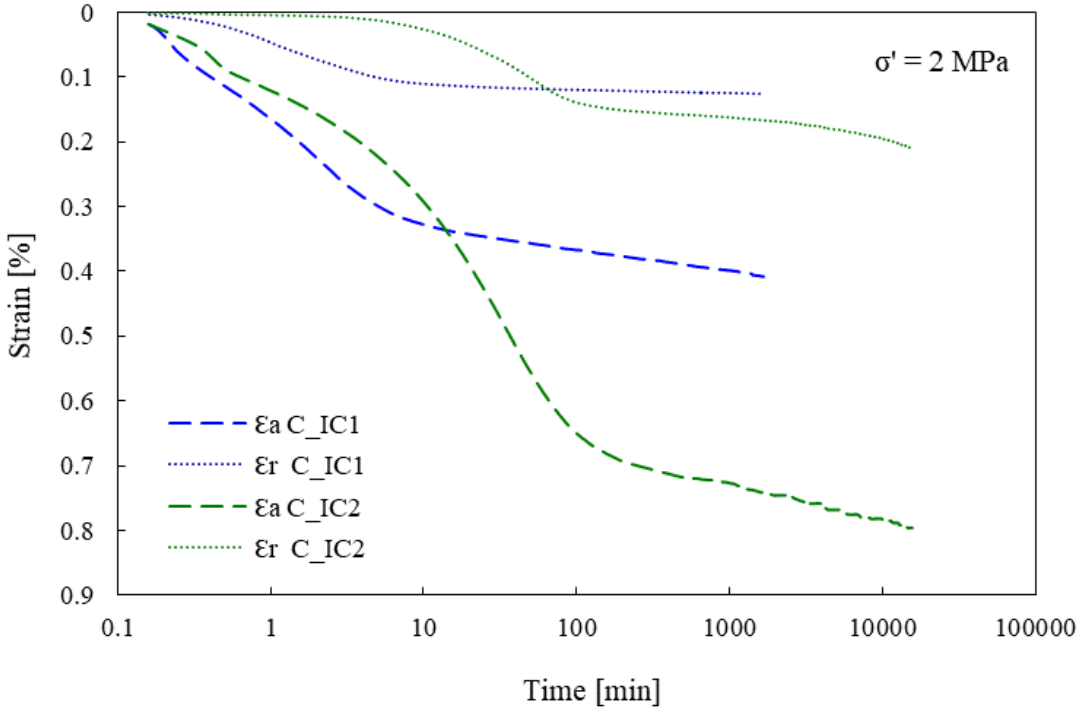

Figure 4.12: Axial and radial creep strain behavior for isotropic tests at 2 MPa

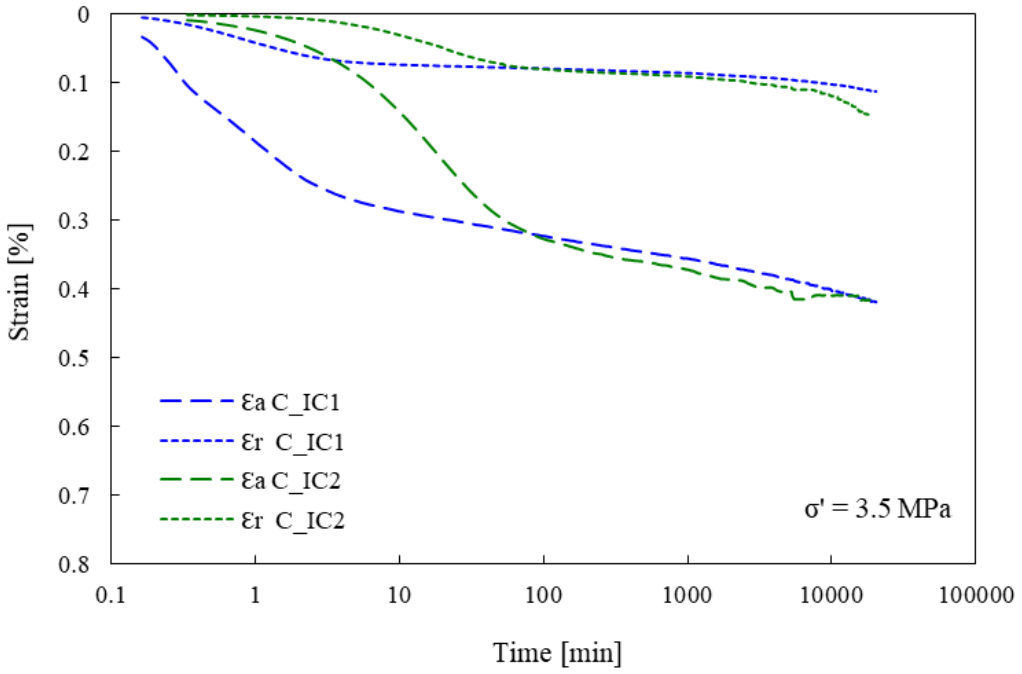

Figure 4.13: Axial and radial creep strain behavior from isotropic tests at 3.5 MPa.

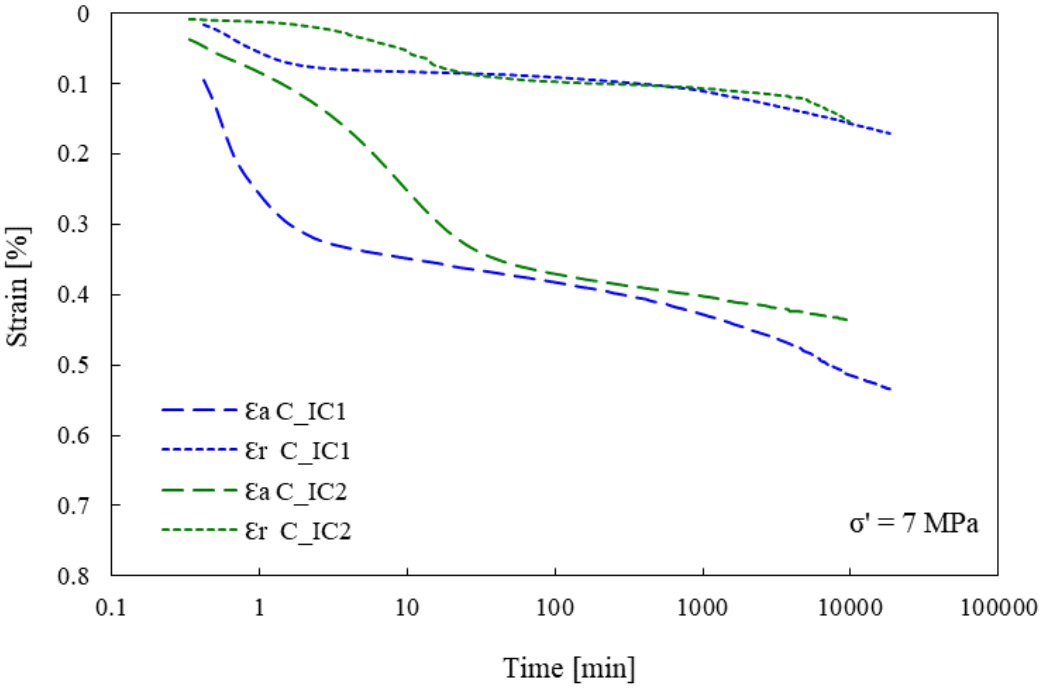

Figure 4.14: Axial and radial creep strain behavior from isotropic tests at 7 MPa.

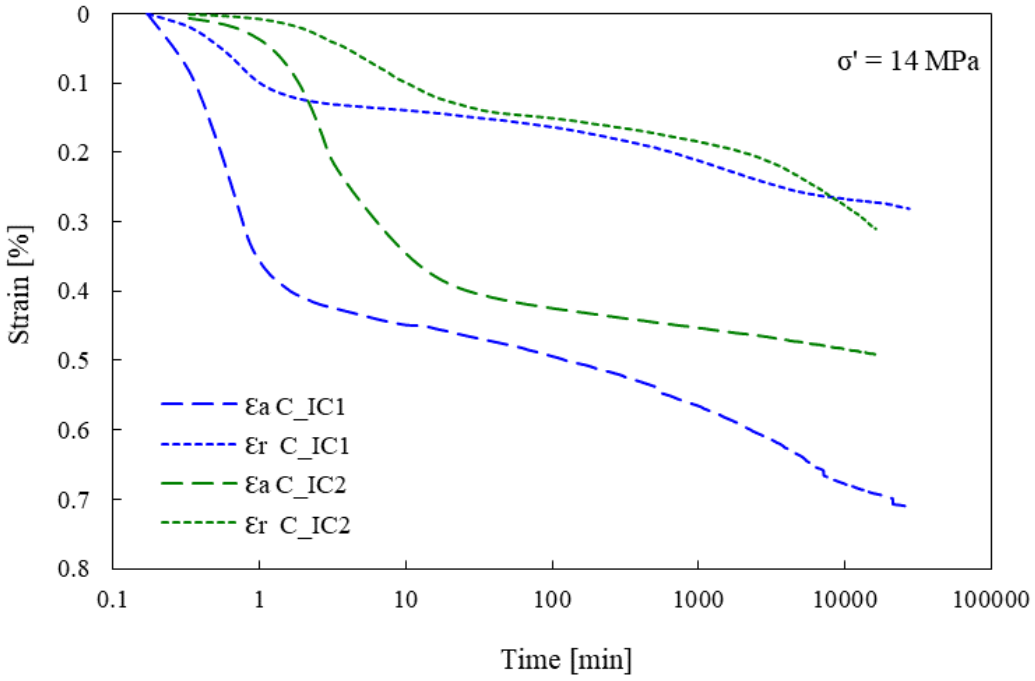

Figure 4.15: Axial and radial creep strain behavior from isotropic tests at 14 MPa.

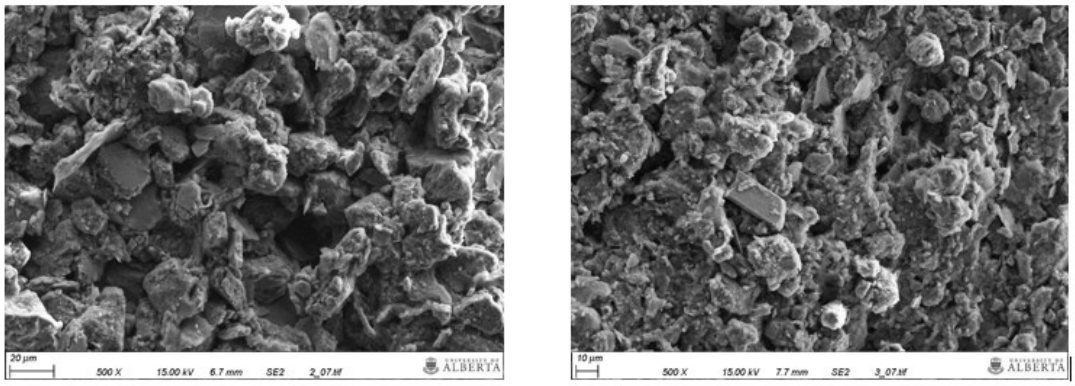

a) b)

Figure 4.16: SEM images (550x magnification) from isotropic creep test CI_Is1: a) Pre-test and b) post-test.

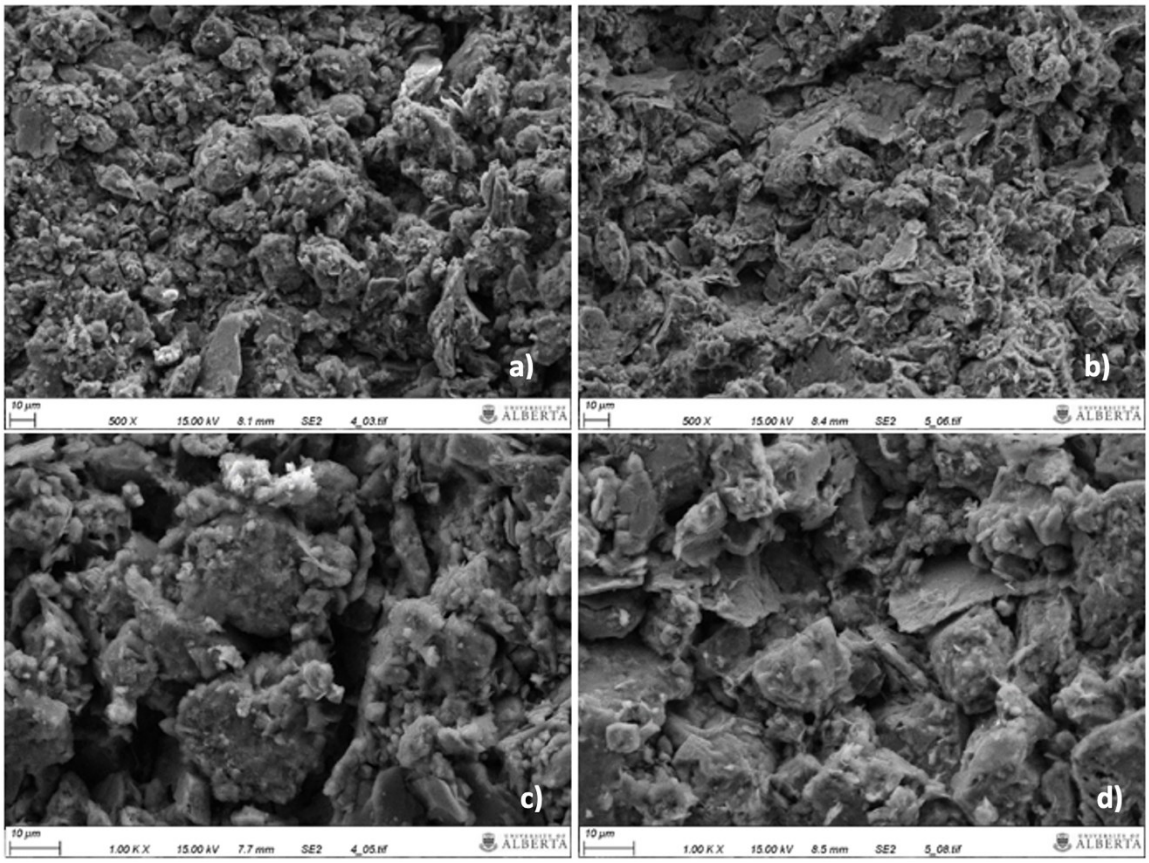

Figure 4.17: SEM images from oedometer creep test CI_Od2: a) 500x Pre-test , b) 500x Post-test , c) 1000x Pre-test and d) 1000x Post-test.

4.4.1.4 Creep Strain Comparison from Isotropic and Oedometer Tests

Isotropic and oedometer $\varepsilon_v - \log t$ results over the same effective stress step are plotted together to study the creep behavior under the two different testing methods (

Figure 4.18). It is possible to compare creep magnitudes and behaviors since the loading steps and stage duration are the same or very similar for all tests. As well, even though CI_Is1 and CI_Is2 tests have different loading rates, their behaviors can be compared successfully as explained in §4.4.1.2.

From the results shown in

Figure 4.18, it is evident that the EOP occurs rapidly in all samples, in every stage. This is indicative of how quickly the onset of creep deformations can occur in Clearwater clay shales. After t_p, all the measured strain comes from the material's viscous behavior

causing compression at different creep rates $C_{\alpha\varepsilon}$. Creep rate remains constant with time during each σ'_V stage for the oedometer tests but for the isotropic tests $C_{\alpha\varepsilon}$ increase with time. According to Mesri (2005), C_α can remain constant, increase or decrease with time, and lead to completely reasonable magnitudes of secondary compression. It can also be noticed that secondary compression index $C_{\alpha\varepsilon}$ is stress dependent. The relation of $C_{\alpha\varepsilon}$ with time can be observed in Figure 4.19, where $C_{\alpha\varepsilon}$ values at different t/t_p are plotted. The results show how $C_{\alpha\varepsilon}$ remains constant until σ'=3.5 MPa (approximately the in-situ stress state of the specimens) and the increases with time. According to Mesri (2001) this is the correct trend for effective stresses inside the destructuration zone. The results shown in Figure 4.19 also provide evidence that at effective stresses of 14 MPa, the specimens have not reached the normal compression line (NCL) since $C_{\alpha\varepsilon}$ is continuing to increase. If the NCL had been reached, the value of C_a should tend to remain relatively constant. These creep strain results are also consistent with the results obtained in Chapter 3.

Comparison of the strain behavior also reveals that samples tested under one-dimensional condition exhibit higher strain response when compared to the isotropic test results. The difference in volumetric strain between the oedometric and isotropic conditions increases as effective stress is increased, likely the result of evolving states of anisotropy in the specimens. The samples in an oedometer test are loaded under an axisymmetric strain condition that generates additional anisotropy while for the samples tested under isotropic stress conditions, creep processes lead to a reduction in anisotropy as effective stress is increased. It is also important to remember that 1-D oedometer loading under high effective stress conditions in stiff material can cause ring friction and significant fluctuation of lateral stress, adding to the anisotropic behavior in oedometer tests. During isotropic loading it is possible to maintain a well known stress condition over extended periods of time, while this is not the case for the oedometer test, where lateral stress is always unknown. The different compression behaviors from isotropic and 1-D loading can also be observed in the $\varepsilon - \log \sigma'_v$ behaviour, as discussed in the next section.

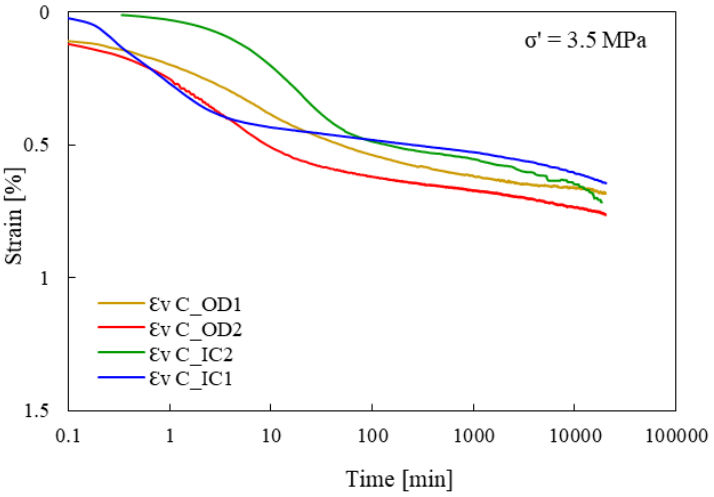

a)

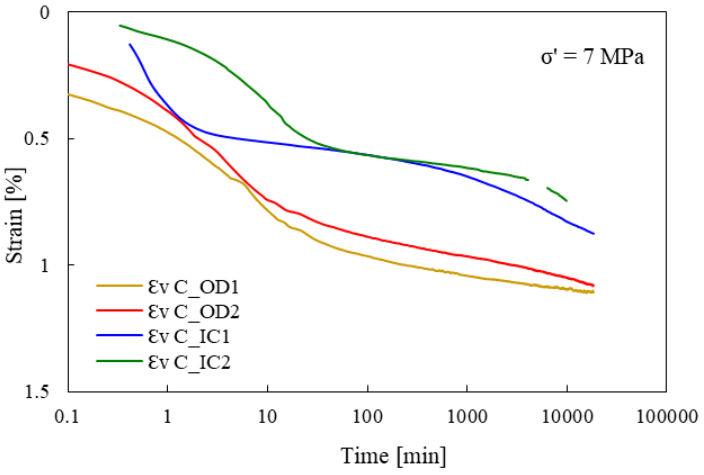

b)

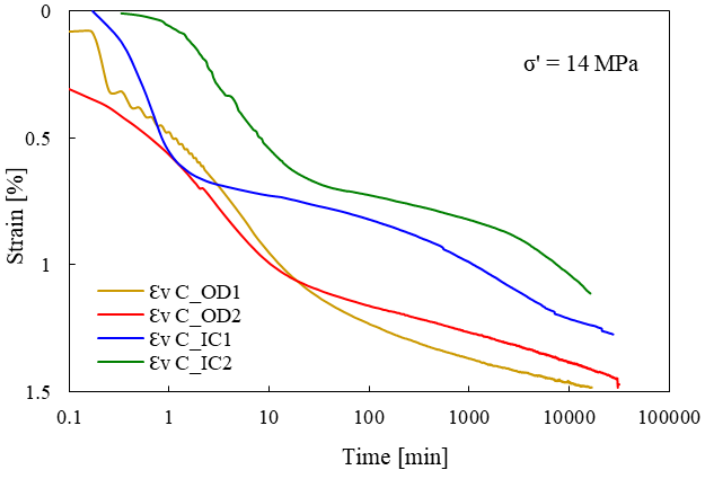

c)

Figure 4.18: Volumetric creep strain comparison. Oedometer and isotropic creep tests at a 3.5 MPa, b) 7 MPa and c) 14 MPa.

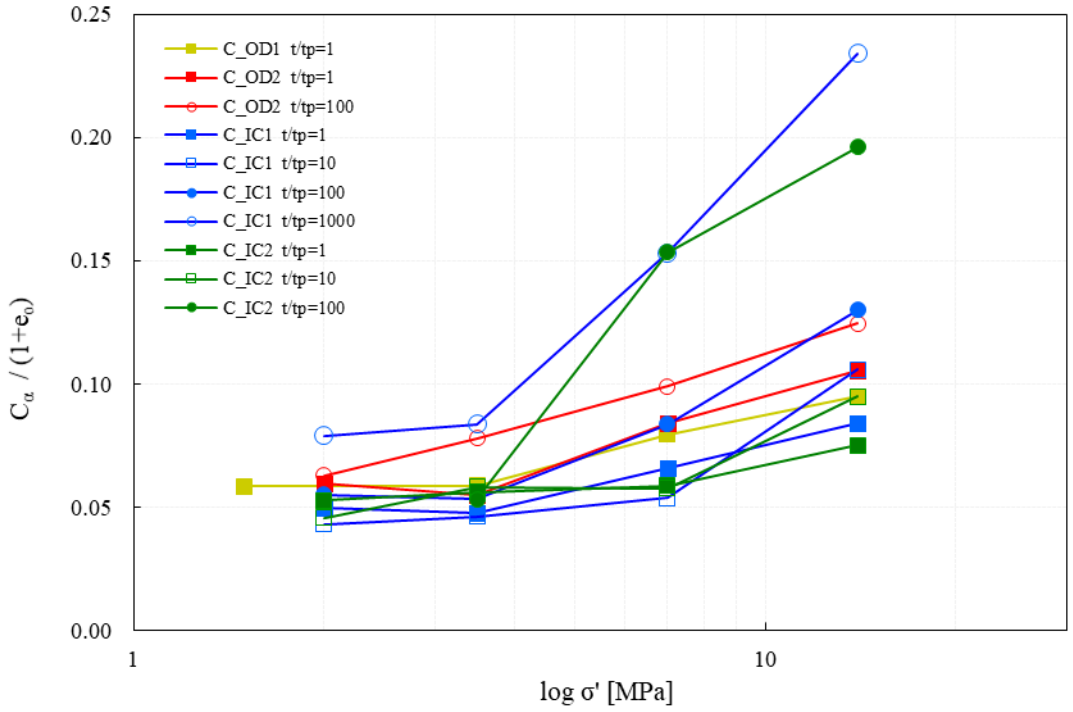

Figure 4.19: Secondary compression index – effective stress – time relationship.

4.4.2 Strain-Effective Stress Relationship

From $\varepsilon - \log t$ curves for different stress states at different times, compression behavior can be further studied. The results from compressibility tests are usually presented in volume change-stress space. For the present creep tests, conventional volumetric strain versus log effective stress plots are used to define compression indices and compression curve C_c for 1-D and 3-D conditions as follows:

$$C_{c\varepsilon} = \frac{\Delta \varepsilon_v}{\Delta \, log \, \sigma'_v} \tag{3.6}$$

It is common for drained isotropic stress conditions that the compression curve is represented in terms of specific volume ($v = 1 + e$) and the natural logarithm of mean stress ($p' = \sigma'_1 = \sigma'_3$), where the compression slope is defined by λ. However, in order to obtain comparable results for the isotropic and 1-D compression test, C_c will be used and it can be easily converted to λ using the relationship:

$$C_c = ln(10)\,\lambda \tag{3.7}$$

Moreover, when void ratio is required for calculations, such the case of C_α/C_c law of compressibility, it is related to strain by the following expression:

$$\Delta e = \varepsilon_v(1 + e_i) \tag{3.8}$$

Therefore,

$$C_{c\varepsilon} = \frac{\Delta e}{(1 + e_I)\,\Delta\, log\, \sigma'_v} = \frac{C_c}{1 + e_i} \tag{3.9}$$

4.4.2.1 EOP $\varepsilon - \log \sigma'$ Curves

The most widely used method for defining deformation at the end of primary consolidation is based on the theory that EOP strain versus effective stress is independent of t_p (Leonards 1972, Ladd et al. 1977, Mesri 1977, Mesri and Choi 1985a, Jamiolkowski et al. 1985, Mesri et al. 1994, Leonards and Deschamps 1995, Mesri et al. 1995). Observations to imply this theory include reliable results of consolidation tests on samples with different thickness that showed different t_p's gave similar curves (Aboshi, 1973; Mesri et al. 1985, 1995, 2001). In addition, empirical evidence from field and laboratory studies led to the matching predictions of mobilized preconsolidation pressure and settlement analysis. Finally, mathematical analysis of compressibility parameters suggests the same hypothesis. The theory does not state that creep acts as a separate phenomenon during primary compression. In fact, creep behavior contributes during primary compression. However, soils have only one structure which controls both compressibility's with effective stress and compressibility with time and EOP $\varepsilon - \log \sigma'_v$ relation carries information about the relation between strain and time.

In this research, four EOP consolidation curves are built based on EOP nominal strains at each consolidation pressure, thus taking into account previous compression

history. Misleading results can be obtained if the relation is built by adding EOP strains of pressure increments. Figure 4.20 compares the results of the EOP consolidation curves from CI_Od1, CI_Od2, CI_Is1, and CI_Is2. Results show that the EOP is the same for the two samples tested in the oedometer cell and very close for the two samples tested in the isotropic cell. However, the curve is different between the oedometer and isotropic tests. Since Clearwater clay shale is anisotropic with a tendency towards horizontal planes, the oedometer curves show less resistance to deformation than the curves from the isotropic cell; therefore, oedometer curves show a steeper behavior. As discussed above, potential ring friction and lateral stress variations in the oedometer tests creates some uncertainty in the results.

The compression coefficient $C_{c\varepsilon}$ is increasing with effective stress even at the last loading increment, indicating that the normal compression line NCL has not been reached at 14 MPa. Reaching the NCL would have offered an opportunity to assess a more advanced characterization of the material but for practical purposes, at the in-situ stress of approximately of 3.5 MPa, the clay shale is at a state below the preconsolidation stress, beyond which the material would display higher compressible behavior. And even for 14 MPa stress conditions, the clay shale remains below the yield stress, which marks the abrupt onset of increased compressibility. In retrospect, it would have been valuable to test at stress conditions where the NCL was reached in order to better characterize the full compression behaviour of the clay shale and to determine the yield stress, which is usually estimated from the EOP ε_v-log σ' curve.

In Chapter 3, compression curves were analyzed together with curves from reconstituted samples where it was possible to conclude that Clearwater clay shale developed strong structure not only from geological unloading but also from processes like creep and diagenesis, indicating that the Clearwater Formation caprock from this well location appears to be well below the point where destructuration conditions would impact the behaviour of these materials.

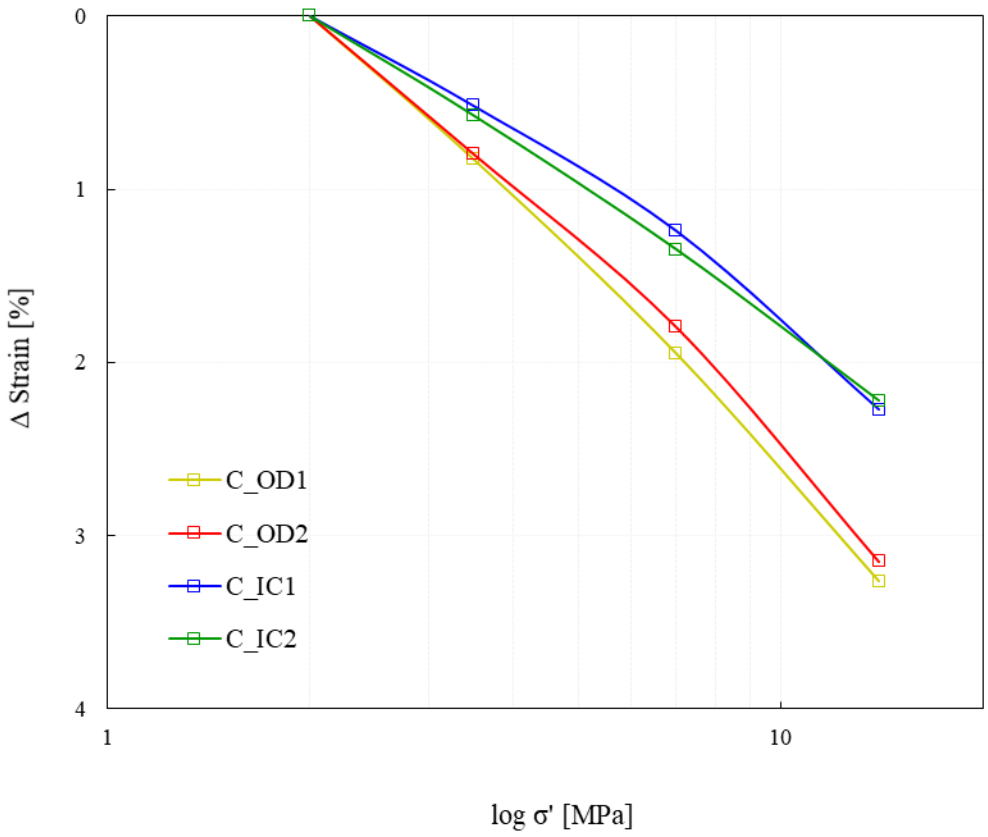

Figure 4.20: EOP consolidation curves from 1-D and isotropic tests.

4.4.2.2 $\varepsilon - \log \sigma'$ curves for $t/t_p > 1$

It is crucial to identify the EOP $\varepsilon - \log \sigma'$ curves, however, when the region of interest to study is within effective stress values around the recompression range, primary consolidation has a short duration and the compressive behavior of the material over time is mainly controlled by its creep potential $C_{a\varepsilon}$. For a structured material like the Clearwater clay shale, which has been shown to experience significant creep strains after t_p, it is necessary to characterize long-term creep behavior since it dominates the material's volume change.

While there is a unique EOP $\varepsilon - \log \sigma'$ curve for each loading method, infinite compression curves can be obtained from times greater than the time to reach primary consolidation, t_p. EOP $\varepsilon - \log \sigma'$ curve corresponds to $t/t_p = 1$, therefore, for creep strains at any time after t_p, $\varepsilon - \log \sigma'$ curves for different t/t_p values can be obtained, and the

effects of creep strain over time can be analyzed in more detail. To build the $t/t_p > 1$ curves, strain values corresponding to the same t/t_p are identified on each pressure increment, and the results are plotted for each t/t_p, similar to EOP $\varepsilon - \log \sigma'$.

For the oedometer tests, only one $C_{a\varepsilon}$ value was observed for each pressure increment, and this value was increasing with stress, as shown in Figure 4.21 and Figure 4.22. Strain-time relations of CI_Od1 and CI_Od2 were very similar, including $C_{a\varepsilon}$, thus, curves for $t/t_p > 1$ are also virtually the same. Constant $C_{a\varepsilon}$ values are not consistent with creep behavior inside a destructuration zone. This leads us to believe that oedometer tests are not giving the correct information about the creep behavior of Clearwater for long testing times.

For the isotropic tests, Figure 4.23 and Figure 4.24 show the strain data for different t/t_p values, plotted against the logarithm of effective stress. These results illustrate the strains resulting from consolidation and creep at any consolidation pressure σ' and at any time equal or greater than t_p. The values of $C_{a\varepsilon}$ during isotropic tests have a more complex long-term nature over time due to anisotropy as can be seen on $\varepsilon_v - \log t$ curves. $C_{a\varepsilon}{}'s$ show a significant increase of magnitude with time after some time of secondary compression, and as explained before, $C_{a\varepsilon}$ and $C_{c\varepsilon}$ are related to each other consequently, the $C_{c\varepsilon}$ index is increasing with time shown in Figure 4.23 and Figure 4.24.The results from the isotropic tests show increasing $C_{a\varepsilon}$ and $C_{c\varepsilon}$ values, which complies with the destructuration behavior for pressure increments near the preconsolidation pressure σ_p'.

Finally, from $\varepsilon - \log \sigma'$ curves for different t/t_p it can be clearly noticed that creep strains have a similar effect of over consolidation caused by aging. Creep reduces the amount of primary consolidation on the next loading and mobilizes preconsolidation pressure. These results may indicate positive news for Clearwater strength because over time creep is creating a new yield surface, and the constant effective stress sits further from it.

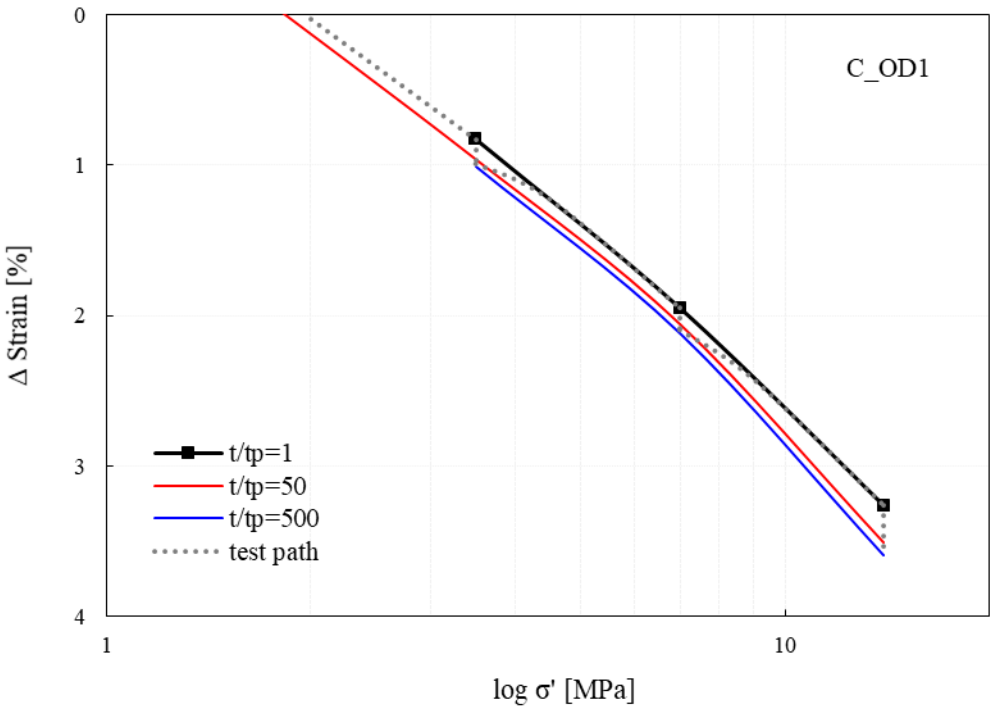

Figure 4.21: Compression curves from CI_Od1 for $t > t_p$.

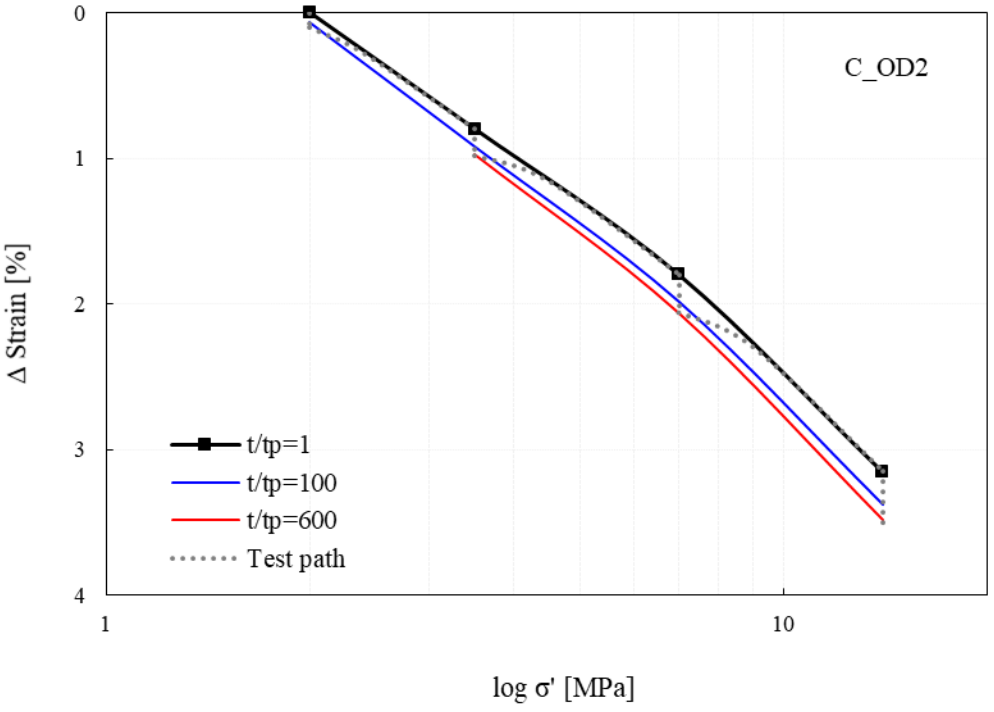

Figure 4.22: Compression curves from CI_Od2 for $t > t_p$.

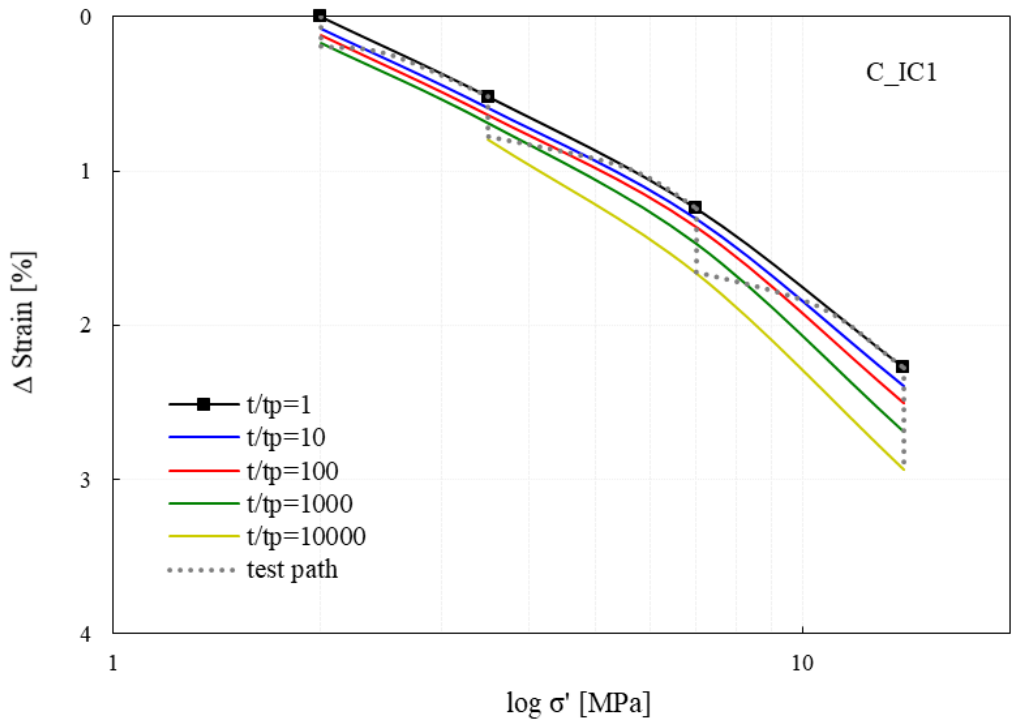

Figure 4.23: Compression curves from CI_Is1 for $t > t_p$.

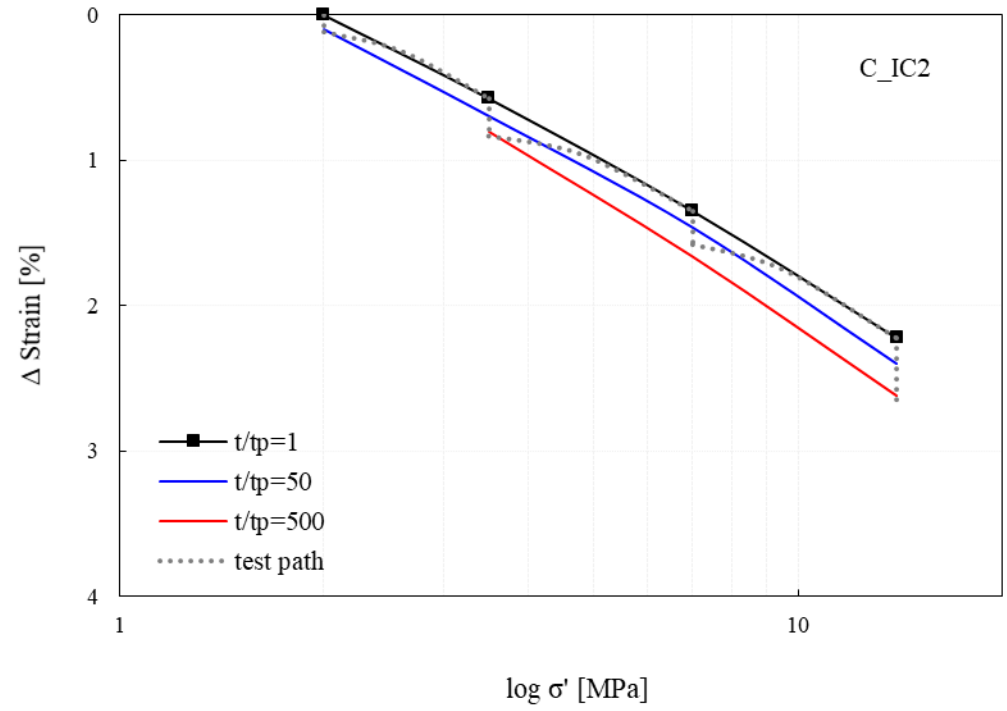

Figure 4.24: Compression curves from CI_Is2 for $t > t_p$.

4.4.2.3 Creep influence on yield stress

Determining the preconsolidation/yield stress of any geomaterial is one of the most challenging geotechnical problems and yet is one of the most important characteristic of clayey materials. When a load is applied, the preconsolidation pressure or yield stress (Burland, 1990) defines the yield point that determines a stiff or soft mechanical response of the material that will result in the change from small deformation to large deformation.

Several methods have been proposed to determine and the most used and accepted are based on simple graphical procedures considering the principle that the material response changes from stiff to soft as it passes the yield stress. According to Mesri & Feng (2014), since the EOP $\varepsilon - \log \sigma'$ relationship is independent on the duration of primary consolidation, preconsolidation pressure mobilized in the field would be the same or nearly the same from the one determined from laboratory tests on undisturbed specimens. Many studies from laboratory tests of samples with different specimen size, field tests, monitoring data, and mathematical investigations supports this theory.

From the stress-strain time relationships determined for Clearwater clay shales, there is some sense of the preconsolidation pressure conditions. The effective stress loading steps were selected according to the actual in-situ conditions and potential maximum effective stresses a steam chamber may induce within a clay shale caprock under safe operations. At the depth in the well where the samples were obtained, the in situ effective stress is 3.5 MPa, whereas the maximum effective stress in the test is 14 MPa. At 14 MPa, the samples still does not show a clear yield point in the $\varepsilon - \log \sigma'$ compression curve and exhibited behavior that indicated the stress state remained inside the destructuration zone and below the yield stress. It is important to recall that yield stress is not only caused by the maximum stress to which the sample has been subject in the past, but also to other conditions like aging, structure and as indicated in this chapter, creep. From the results presented in this chapter, it is clear that we did not reach the normal consolidation line NCL and therefore, we cannot make a conclusion on a definite value of yield stress. Additional consolidation tests at higher effective stresses are required to characterize Clearwater's yield stress accurately. The positive outcome of this result is that at 14 MPa, the Clearwater clay shale is still below the yield point when large volumetric strains start to occur.

Additional analysis comparing the results from this chapter to the compression behavior of reconstituted samples according to the intrinsic compression line theory (Burland, 1990) were presented in Chapter 3 and support these beliefs. Finally, creep progressively increases the yield surface because the size of the yield surface is dictated by the magnitude of the preconsolidation/yield pressure, which is constantly increasing due to the irreversible strain accumulated under creep. As was seen on Figure 4.21 to Figure 4.24, preconsolidation pressures are time-dependent and the samples developed an apparent increase in the preconsolidation/yield stress by letting them creep. This effect is referred to as "quasi-preconsolidation effect" and was first described by Leonards and Ramiah (1960).

4.4.3 C_α/C_c Relationship

It is well established that for any geomaterial, including shales, a unique relationship between C_α and C_c exists in the recompression and compression range, as explained before.

In order to examine the C_α/C_c law of compressibility on Clearwater clay shale, data pairs of C_α and C_c are carefully selected at specific times t/t_p and plotted in a $C_\alpha/(1+e_o)$ versus $C_c/(1+e_o)$ plot (Figure 4.25). The plotted data pairs correspond to oedometer and isotropic tests on intact and reconstituted samples. We can see that most of the data follow a linear trend giving a C_α/C_c coefficient of 0.021. The fact that intact and reconstituted samples for one-dimensional and isotropic loading conditions share the same coefficient gives us confidence in the results. Besides, this number is entirely in agreement with C_α/C_c values for geotechnical materials (*Table 4.1.* Values of C_α/C_c for geotechnical materials (Terzaghi et al. 1996)., which states that the index range for shales is 0.03 ± 0.01 and for granular materials is 0.02 ± 0.01. XRD analysis discussed in Chapter 2 showed that Clearwater clay shale has granular material, so, 0.02 is a very reasonable result. However, data pairs from late times on each effective stress stage of isotropic tests do not follow the same trend. Those pairs were carefully revised and it was found that in order to compute logical C_α/C_c values, late time slopes $C_{\alpha\varepsilon}$ should be paired with irrational $C_{c\varepsilon}$ values. While it is correct that $C_{\alpha\varepsilon}$ increases with time in the destructuration zone, the rate at which

it is increasing does not follow the typical secondary compression that characterizes C_α/C_c. Thus we believe that until a certain time, creep is governed by particle reorientation and then, creep rate acceleration is caused by a destructuration zone with complex forms of creep coming from the high anisotropy and structure of Clearwater. However, the test with the longest testing time stage, CI_Is1 28000 min at 14 MPA, shows that the accelerated creep is followed by a decrease in creep rate and the final $C_{\alpha\varepsilon}$ joins again C_α/C_c trendline of 0.021. CI_Is2 7 MPa is also showing a slight creep rate decrease at the end but not as significant as 14 MPa. This might indicate that at higher effective stress creep stability is reached faster.

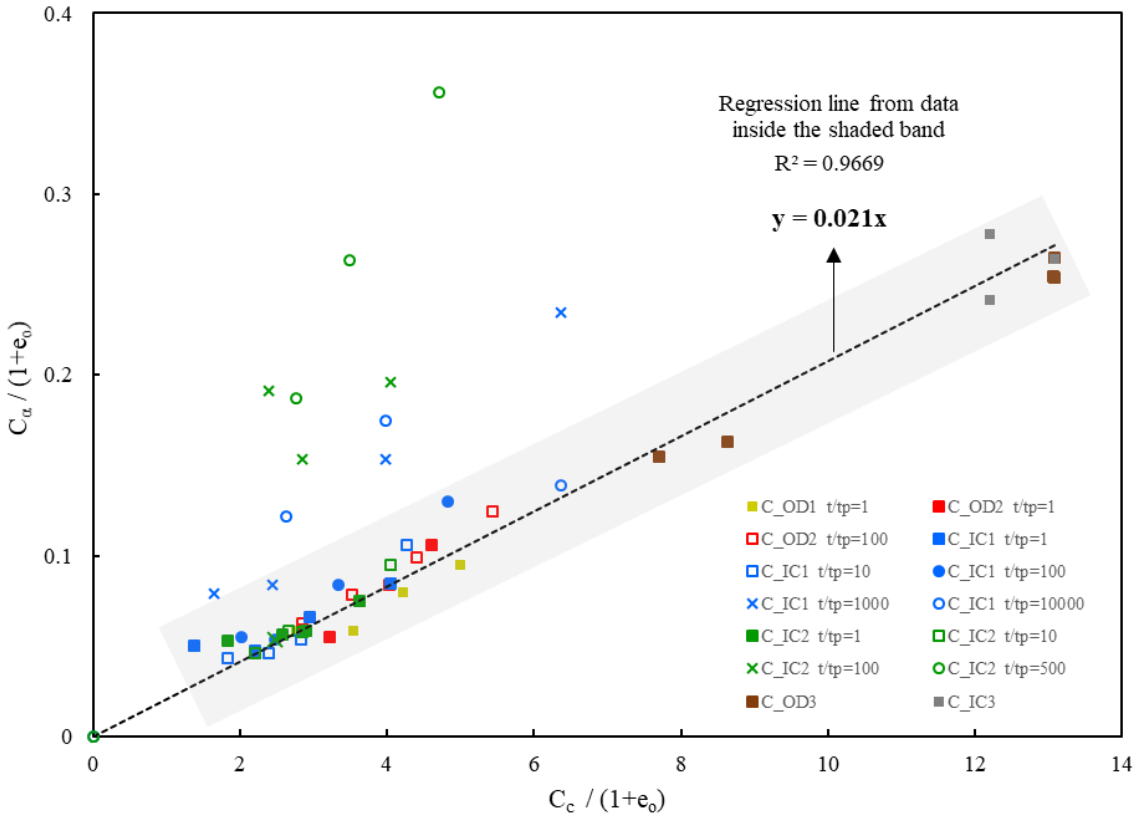

Figure 4.25: C_α/C_c relationship for Clearwater material.

4.4.4 Potential Effects of Creep on Caprock Integrity

With the exception of the work by (Li, 2017), there are no available studies on the creep behavior of Clearwater clay shales. Lithification and diagenetic processes have resulted in a hard soil – soft rock classification for these clay shales which display complex constitutive behavior that manifest as complex long-term strain responses for various loading conditions. Creep tests for shales found in the literature are generally oriented towards studying creep under the influence of deviatoric stress and its impact on strength. Irrespective of the paucity of data specific to conditions related to caprock integrity, the results of the testing performed in this research allows several observations to be made.

In general, the time-dependent response of geomaterials could be classified as volumetric creep (secondary compression) from isotropic tests, or as deviatoric creep from triaxial stress tests. The definite effect of creep on geomaterials depends on the shear stress to strength development ratio. Thus, it is important to understand the mechanics behind creep since it can cause either a positive or a negative impact on caprock integrity by strengthening or weakening the material. First, it is well known that the mechanical behavior of shales is largely controlled by their microstructure (Josh et al., 2012), and we believe that the accelerated viscous behavior observed in our isotropic tests is microstructure related.

According to Ter-Stepanian (1992) there are four levels of deformation: the molecular level, mutual displacement of particles as a result of bond failures, but without rearrangement, the structural level of soil deformation involving mutual rearrangements of particles, and deformation at the aggregate level. Mitchell & Soga (2005) discussed the behavior of the latter two and described five time-dependent deformation-structure interactions, including particle rearrangement, particle breakage, aging or strengthening of the material, changes in soil fabric, and changes in the physicochemical interaction of clay and pore fluid. The time-dependent process of particle rearrangement is originally related to the ratio of tangential to normal forces at individual contacts that can lead to rearrangement into more stable configurations and frictional equilibrium. Particle breakage or yield of asperities from creep increase with load duration, and the new fines fill the voids and rearrange gradually. Time-dependent strengthening of the structure by aging causes an

increase in material stiffness, and consequently, an increase in preconsolidation pressure, it strengthens the fabric by causing changes in shear modulus with time. However, this effect cannot be described with change in volumetric strain. Time-dependent change in the fabric is regarded as the final step of kinematic restraint; it influences the structure stability due to movements of particles that generate dense interlocking zones resulting in a more isotropic fabric with stiffer structure.

Analysis of microstructure SEM pictures (Figure 4.16 and Figure 4.17) and observational inspections before and after the creep tests show that the material becomes denser and stiffer after creep tests. It was observed that sample features that were noticeable during sample preparation as hairline fissures and discontinuities were not visually perceptible after the test. Moreover after-test SEM images show fewer clusters, finer materials, more voids filled, and in general, a more compact microstructure than before-test pictures for all of the tests. Isotropic and oedometer creep tests show slightly different after-test microstructures; sample tested under 1-D conditions seem to preserve horizontal clayey laminations and angular contacts better than samples of isotropic tests.

Accelerated creep behavior of geomaterials are frequently attributed to tertiary creep response and failure. Viscous deviatoric (shear) strains always tend to degrade structure and strength in a way analogous to damage by plastic strains in inviscid structured soils, sometimes causing failure. However, it is important to remember that the stability of a material exposed to creep strains only depends on the shear stress to strength ratio. And, volumetric or isotropic creep tends to increase structure and shear strength by reducing shear stresses due to rearrangement, interlocking, and aging, developing an apparent pre-consolidation (Schmertmann, 1992), as showed in from Figure 4.21 to Figure 4.24. Thus, we can suggest that accelerated creep observed in our Clearwater samples is not leading to failure, but to a more compact and stronger material with fissure healing properties. Although strength tests are required to investigate this hypothesis, the data, coefficients and properties given in this chapter provide a basis to understand Clearwater caprock viscous compression behavior. The results also serve as a guide to future research and characterization of Clearwater creep behavior under different scenarios.

CHAPTER 5: THERMAL CREEP TESTS ON CLEARWATER

5.1 INTRODUCTION AND THEORETICAL BACKGROUND

Recent success in producing from unconventional Canadian oils sands reservoirs is made possible by thermal recovery applications like steam-assisted gravity drainage (SAGD) and cyclic steam stimulation (CSS). In this extraction method, effective production not only involves reservoir engineering processes but geomechanical challenges of maintaining the integrity of the sealing caprock and casing for steam injection at high operating temperatures that could easily reach 200 to 350°C.. And these geomechanical challenges are made even more challenging in some case due shallow reservoir depths and temperature-induced alterations including reservoir and caprock deformations.

Over the life of a thermal project, the steam chamber can reach the caprock and by both convective and conductive heat transfer, increase the temperature within the caprock (Aghabarati & Chalaturnyk, 2017). Many laboratory studies have concluded that creep strain rates are extremely susceptible to the environmental conditions with temperature being a major factor that produces a significant acceleration in creep strain rate (Malik Belmokhtar et al., 2017; Brantut, Heap, Meredith, & Baud, 2013; Delage, Sultan, & Cui, 2000; Jarad & Masrouri, 2016; Khosravi & Ghassemi, 2017; Hiroki Sone & Zoback, 2013). These thermal creep strains can result in positive effects such as increased strength, fissure healing and closure of shale-cement interface cracks (Fjaer, Folstad, & Li, 2016; Horseman, 2001) but can also lead to negative effects such as decreased strength.

Temperature can weaken or strengthen shales depending on the relation between the thermal compaction process and thermally induced pore pressure increase (Xu, Yuan, & Wang, 2011). Understanding the influence of temperature on creep deformation is also important for reservoir and caprock integrity simulations and history matching to ground surface deformation monitoring data. Research has been conducted to investigate the oil sands deformation response to the effects of increasing temperature but to the author's knowledge, there is a limited number of studies about caprock properties under elevated temperatures (Chalaturnyk, 1996; Kosar, 1989; Oldakowski et al., 2016; Xu et al., 2011). With the exception of confidential experimental programs, no data was found in the public literature about Clearwater caprock thermal-induced volumetric change.

Consequently, this chapter provides test results on the temperature effect on long-term deformation of Clearwater clay-shale at in-situ effective stress conditions. Long-term multi-stage tests similar to the tests in Chapter 4 are conducted but, in the present case, instead of increasing the effective stress, the latter is left constant and only the temperature is increased. Temperature is increased stepwise; the desired temperature of each stage is achieved using a very low heating rate. After thermal equilibrium is reached on each stage, the sample is left under constant temperature for around 10,000 min. The tested samples correspond to three contiguous Clearwater samples from the North Athabasca zone that share similar properties. The experiments were performed using two oedometer cells and one isotropic cell, resulting in one dimensional and triaxial deformations, respectively. We analyzed the experimental data gathered from the tests in this section and studied some fundamental effects of temperature on the overall creep behavior of Clearwater. The results obtained from the two different stress path tests were compared and analyzed.

The execution of this experimental study was a challenging one due to the high temperatures reached during the tests (200ºC). These elevated test temperatures affect many properties of the testing equipment and additional components. The specification sheets of the equipment/instruments should be carefully reviewed, and any potential effect induced by high temperature in the mechanical and electrical configuration of the system should be considered and if deemed to be significant, should be addressed.

The experimental studies of the time-dependent behavior of Clearwater clay-shale presented in Chapter 4 show that a significant amount of creep deformation is happening in Clearwater clay shale and should not be neglected when analyzing issues of caprock integrity or well integrity.

5.1.1 Temperature Reaching the Caprock

Steam temperature can be conducted to the caprock through the steam injection well, and, in some cases, from the steam chamber reaching the caprock. In addition, the possibility of temperature convection from fluid moving through the reservoir to the overlying caprock cannot be ignored. Aghabarati & Chalaturnyk (2017) studied the contributing heat transfer mechanisms above the steam chamber and the major factors affecting the measurement of true temperature distributions in the formation from observation wells and their corresponding temperature profiles. In this study, they concluded that depending on the geology of the area, the injected steam could experience three major propagation scenarios: 1) propagate to the top of the pay zone, 2) be stopped by a thick impermeable layer, and 3) detour around impermeable layers or interbeds and grow vertically again until eventually reach to the formation top. 1D and 2D simulations completed by Aghabarati & Chalaturnyk (2017), together with field data, showed that interpretation of the observation well data and temperature profiles, including the contribution of convective flow, is dependent on the permeability, injection pressure and the monitoring location of the observational well. Considering the possibility of heat transfer to the capping shale, temperature effects should be addressed in any behavioral study of caprock.

5.1.2 Effect of Temperature on Clayey-Shale

According to Abuel-Naga, Bergado, Soralump, & Rujivipat (2005); Jarad & Masrouri (2016) the main factors influencing the thermal properties of soil are soil mineralogy, moisture content, and dry density. Previous research works show that when temperature changes are induced in fine-grained soils, volumetric strain and shear stress

change. It has been widely accepted that this thermo-mechanical behavior is caused by thermally induced changes in physicochemical forces between the clay particles (Graham, Crooks, & Bell, 1983; Mitchell & Soga, 2005). Laloui (2001) research work on thermo-mechanical behavior of saturated fine-grained soils summarized the main experimental observations concerning thermally induced effects on thermal behavior. He concluded that when a saturated soil is heated, all of its constituents dilate (skeleton and fluid), producing a decrease in the strength of the adsorbed layers and a modification in the distance between the clay particles. This disturbs the equilibrium between the Van der Waals attractive forces and the electrostatic repulsive forces. Also, stress history condition plays a key role in thermally induced volumetric changes. Thermoelastic expansion in overconsolidated clays and thermoplastic contraction in normally consolidated clays occurred in most studies. As explained by Hueckel & Borsetto (1990); T. Hueckel and G.Baldi (1990) thermal sensitivity of the elastic domain was found to be different in overconsolidated and in normally consolidated clays. Many published papers on the thermal behavior of clayey soils have shown that an increase of temperature in drained conditions produces a volume reduction of the soil (Campanella and Mitchell 1968).

5.2 THERMAL CONSOLIDATION AND THERMAL CREEP

Stress-induced volume changes in fine-grained, low permeability geomaterials, tend to generate an excess pore pressure that dissipates with time. The increase of effective stress in soil particles from the dissipating pore pressure is known as consolidation or primary consolidation. The popular thermally induced volume change in water-saturated materials, known as thermal consolidation, relies on the same consolidation physics as stress-induced consolidation. When a fine-grained material is heated under drained conditions, a positive excess pore water pressure can be generated if the heating rate is not slow enough, turning into a temporary undrained process. If for a specific heating rate the thermal expansion of soil particles and pore water is higher than the rate of pore pressure dissipation, thermally induced excess water pressure is generated; a consolidation process follows it where all the pore water pressure is dissipated. This case is appropriate for immediate or nearly immediate heating sources, but for SAGD processes, heat transfer to

the upper part of the pay zone and the caprock is a slow process that most likely follows drained conditions.

Leonards (1977) provided further clarification on the meaning of consolidation and compression. They stated that based on Terzaghi's definition, the term compression is attributed to any kind of volumetric reduction, and the term consolidation is a form of compression characterized by an increase in the effective stress caused by a gradual reduction in the pore pressure. Thus, it is not appropriate to use the term consolidation if volume change is not caused by pore pressure dissipation. On the other hand, the continued compression with time under constant effective stress and temperature conditions is controlled by the rate at which the structure of the material can creep or deform at those conditions after excess hydrostatic pressures are dissipated and are commonly referred to as creep behavior, as explained in Chapter 4. With this in mind, the term *thermal creep* is adopted in this research since the experimental studies involve low heating rates that result in drained conditions and no excess pore pressures.

5.3 EXPERIMENTAL METHODS

When conducting high-temperature tests, great care must be exercised, and additional considerations must be taken, including a correct selection of test parameters like heating rate and pore fluid vapor pressure calculations, and equipment calibrations, which is a critical step in achieving representative results.

5.3.1 High-Temperature Test Parameters

5.3.1.1 Pore Fluid Vapor Pressure

The vapor pressure of a liquid varies with its temperature. Thermal creep is dependent on the water content and saturation condition of the sample. The specimen should be saturated with liquid pore fluid at all times; this ensures that strains of the soil

structure are linearly related to the stresses (effective stress) and that vibration due to bubbling of the pore fluid does not cause disturbances.

The pore fluid used in the tests corresponds to a brine solution of 3000ppm NaCl. For this fluid, the concentration of water molecules in the solution is less than that of pure water, which means that the vapor pressure is lower than that of pure water. Being conservative, the vapor pressure of 100% H2O is calculated at the maximum temperature reached during the tests, 200°C. There are many different formulas to calculate the vapor pressure of water, among the most popular for higher temperatures is the Antoine equation given below:

$$\log_{10} P = A - \frac{B}{C + T} \tag{5.1}$$

where T is in °C and P in mmHg. The constants for temperatures up to 374 °C are:

A	B	C
8.14019	1810.94	244.485

The vapor pressure at 180°C was calculated to be 995 kPa with the Antoine equation and 970 kPa with the Buck equation. This number is below the average in-situ pore pressure of the studied material, which is 1000 kPa.

5.3.1.2 Heating Rate for Drained Conditions

The rate of temperature increase has a dominant effect on the drainage condition of clayey materials, including clayey-shale (Burghignoli, Desideri, & Miliziano, 2011; Campanella & Mitchell, 1968; Cui, Le, Tang, Delage, & Li, 2009; T. Hueckel and G.Baldi, 1990; Xu et al., 2011). Most of the thermal-induced volume change tests in low hydraulic conductivity clayey materials presented by literature illustrate partially drained behavior. Even though drained conditions were prescribed for these tests, materials like clayey shales

have low hydraulic conductivity compared to their thermal diffusivity and so reach heat equilibrium prior reaching pore pressure equilibrium. In situations where the heating rate is very high, the rapid increase in soil temperature leads to the development of excess pore water pressure due to the difference in the coefficient of thermal expansion of the pore water and the mineral solids (Campanella & Mitchell, 1968). Hueckel and Baldi (1990) concluded from their experimental heating drained tests that this fast build-up of excess pore pressure leads to an effective stress drop that affects shale's mechanical properties. An eventual failure at the critical state line in clays is caused. All the authors agree that faster heating decreases the strength properties of the material due to cracking and weakening of the structure.

In the present study, we used a very slow heating rate of 0.04 °C/min based on (Xu et al., 2011) Xu et al. 2011. He studied the thermal impact on mechanical properties of low-permeability shales for reservoirs in Alberta, Canada, and obtained a strengthened material using a heat rate of 0.04 °C/min. With this thermal loading rate were looking for drained conditions with no mechanical damage.

5.3.2 Equipment Calibration for High-Temperature Tests

5.3.2.1 Cell Temperature Effects

Thermal deformation of the cell and mounting parts, generate a shift of the LVDT core relative to the housing part, inducing output errors on the measured deformation. To correct these errors, compliance tests for temperature increments were carried out in the oedometer cells A and B, and in the isotropic thermal cell using an aluminum alloy 6061 cylinder with same diameter and similar height as the tested specimens. Aluminum is linear elastic in the working temperature range (200°C) and has an average coefficient of thermal expansion ($\alpha_{al,}$ CTE_{al}) of 2.34 x 10^{-5} $°C^{-1}$. Different CTE_{al} were tested for different temperature ranges but from 20 to 200°C the scale of the coefficient does not change, thus, it caused negligible effects and the average coefficient of thermal expansion is well suited for the test scale of this work.

Both, the isotropic cell and the oedometer cell follow the same procedure for the compliance test. The aluminium sample is mounted in the cell as if it was the actual sample, with all the instrumentation installed, then, it is heated up in steps until reaching 200 °C; waiting between each step for the temperature and LVDT readings to stabilize.

Calculation of the Cell Correction Factor

Assuming that the dimensions of the equipment vary linearly with temperature and that the sample expands simultaneously with the cell, the actual length change of aluminum specimen during temperature change is:

$$\Delta L_{\alpha} = \Delta L_m + \Delta L_f \tag{5.2}$$

If the coefficient of linear thermal expansion (CTE, α) is defined as:

$$\alpha = \frac{\Delta L}{L_o}\left(\frac{1}{\Delta T}\right) \tag{5.3}$$

Then,

$$\alpha_{al} = \frac{\Delta L_{al}}{L_o \times \Delta T} \tag{5.4}$$

And,

$$\Delta L_{al} = \Delta L_m + \Delta L_f \tag{5.5}$$

Therefore,

$$\alpha_{al} = \frac{\Delta L_m + \Delta L_f}{L_o \times \Delta T} \tag{5.6}$$

$$\alpha_{al} = \frac{\Delta L_m}{L_o \times \Delta T} + \frac{\Delta L_f}{L_o \times \Delta T} \tag{5.7}$$

$$\alpha_{al} = \alpha_m + \alpha_f \tag{5.8}$$

Then,

$$\alpha_f = \frac{\Delta L_f}{L_o \times \Delta T} \tag{5.9}$$

Consequently, the correction factor accounting for apparatus deformations due to the temperature variation is:

$$C_f = \alpha_f \times L_o \left[\frac{mm}{°C}\right] \tag{5.10}$$

The correction factor of the cell comes from the difference between the thermal expansion measured and the theoretical expansion of the aluminium cylinder. The above-mentioned equation can be used to calculate ΔL_f in the intact sample tests as long as the original length of the intact sample is the same or close to the length of the calibration sample as follows:

$$\Delta L_f = C_f \times \Delta T \tag{5.11}$$

where:

α : Coefficient of thermal expansion, CTE, [°C^{-1}]

α_{al} : CTE of the aluminium sample, [°C^{-1}]

α_m : CTE of the measured length change, [°C^{-1}]

α_f, C_f : Fake CTE caused by the apparatus, [°C^{-1}]

L_O : Original length of specimen, [mm]

ΔL_α : Actual length change of specimen due to the temperature variation, [mm]

ΔL_m : Measured (LVDT) length change of specimen due to the temperature variation, [mm]

ΔL_f : Fake/additional length change caused by apparatus deformation due to the temperature variation, [mm]

ΔL_{al} : Measured length change of aluminium calibration specimen, [mm]

ΔT : Measured temperature change, [°C]

Oedometer Cell Temperature Calibration

Compliance tests were performed on both high temperature oedometer cells. System A used an aluminum sample with original length of 76 mm and the correction factor, C_f, was computed to be 9.59E-04 [mm /°C]. System B tested an aluminum sample with 70 mm of length and the calculated correction factor was 5.55E-04 [mm /°C]. The test results of system A and B are illustrated in Figure 5.1 and Figure 5.2, respectively. The results of the tests are summarized in Table 5.1.

Table 5.1: Summarized results of oedometer A and B compliance tests

Parameter	System A	System B
Lo [mm]	76	70
α Aluminum [/°C]	2.34E-05	2.34E-05
α Measured [/°C]	1.08E-05	1.56E-05
α False [/°C]	1.26E-05	7.87E-06
C_f [mm/°C]	9.59E-04	5.55E-04

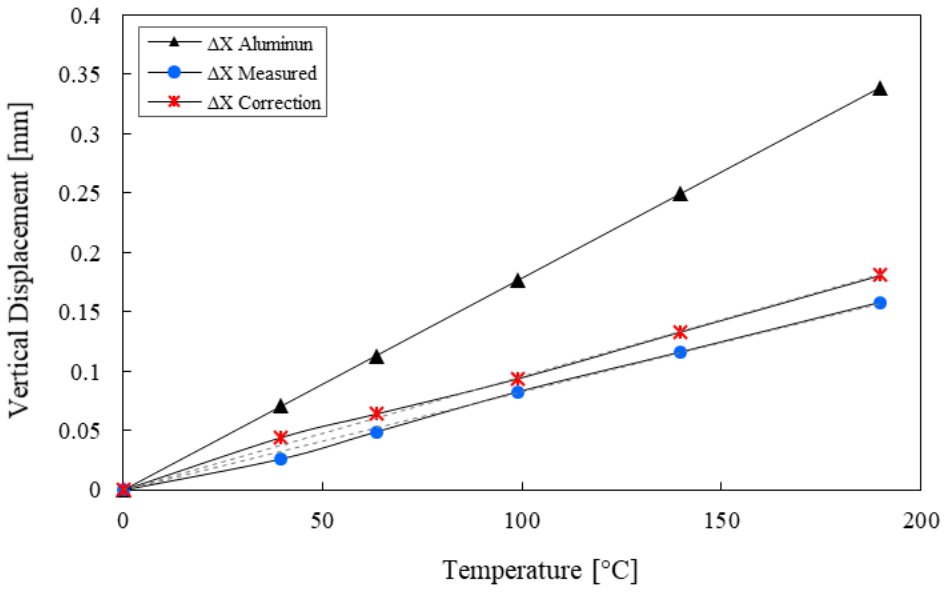

Figure 5.1: Compliance test of the Oedometer system A.

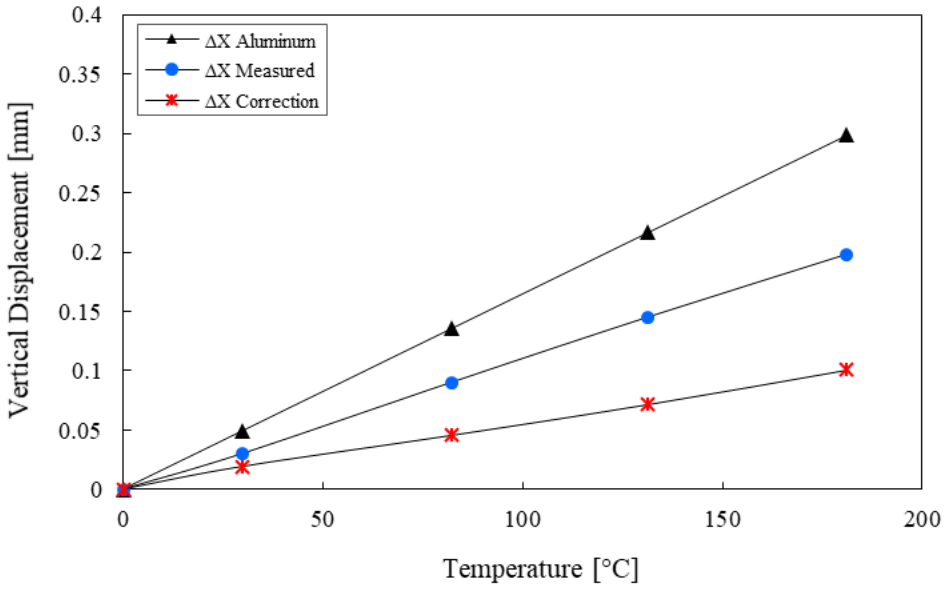

Figure 5.2: Compliance test of the Oedometer system B.

Isotropic Cell Temperature Calibration

The aluminum sample was mounted on the cell using the same set up parts and devices described in the Clearwater sample test. To record the radial strain, one *short* MHR-T LVDT was installed, and for the axial strain, one *long* and one *short* MHR-T devices were used; as described in Chapter 2, *short* LVDT refers to a device with a range of displacements of about 8 mm, and *long* LVDT denotes a device with displacement range of 20 mm.

Before analyzing the compliance test data, it is important to understand the sign convention of the voltage and LVDT reading related to the core position, which is function of the electric connexion of the cables and the calibration factor. Figure 5.3, present the results obtained for the two LVDTs of the axial component, Axial 1 measurements were recorded with a *long* type LVDT and Axial 2 with a *short* type. Figure 5.4 shows the radial component. In a normal fashion, the calibration of the cell is calculated by comparing the theoretical aluminum strain to the measured strain, as previously shown in the oedometer cell calibration. However, the compliance test of the isotropic cell turned out to be more complicated than the oedometer compliance test since the LVDT devices are located inside the cell, completely exposed to induced heat.

In Figure 5.3, it is important to note how the correction required for the *short* LVDT is smaller than for the *long* one despite the fact that the two axial LVDTs have exactly the same mounting pieces and the LVDT core and head are supposed to expand symmetrically. Both axial LVDTs should have measured the same, but that was not the case, the difference between both measurements was significant. According to the LVDT manufacturers, temperature should not affect high-temperature MHR-T LVDTs readings and performance. Nevertheless, it was decided to re-calibrate the LVDTs for displacement measurement and the computed calibration factor turned out to be the same as the initial factor with a regression of 1. That leads to believe that, indeed, the LVDTs experience some kind of temperature sensitivity and, what is more, it could be influenced by the type/size of LVDT. Further investigation was required to explain and deal with this discrepancy, which led to carry on some LVDT temperature sensitivity experiments explained in the following section.

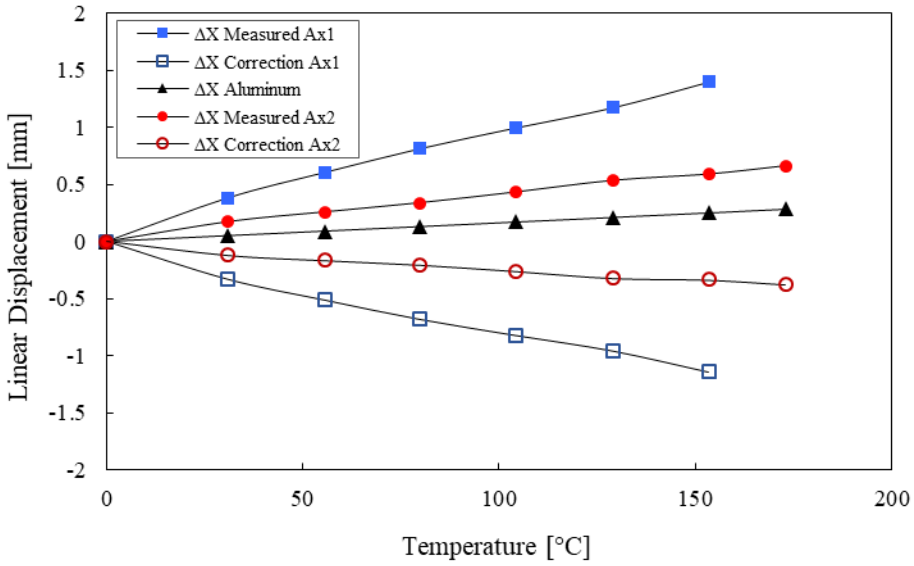

Figure 5.3: Compliance test of the axial LVDTs of the isotropic cell.

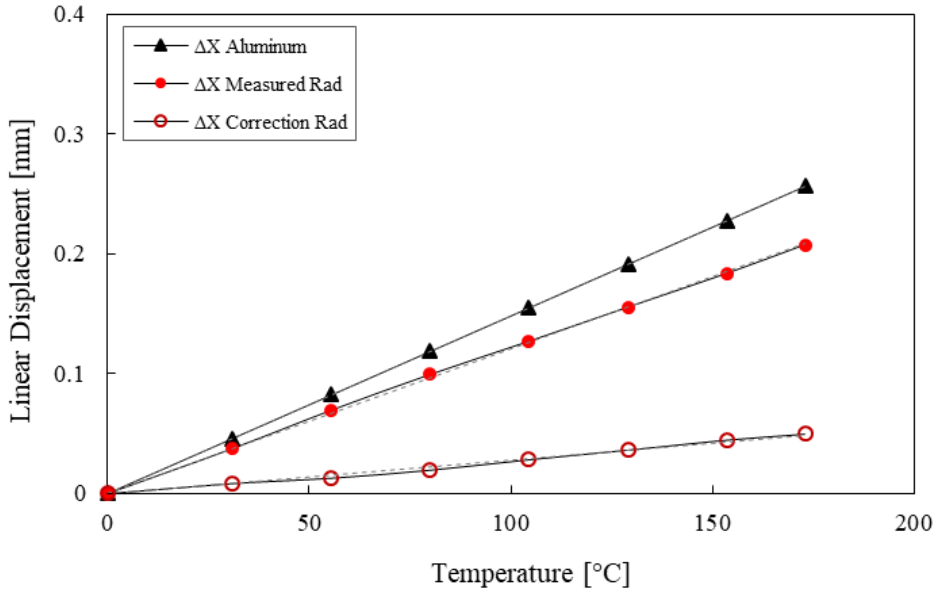

Figure 5.4: Compliance test of the radial LVDT of the isotropic cell.

5.3.2.2 LVDT Temperature Sensitivity

Sensitivity Tests

A series of temperature sensitivity tests were performed in the MHR-T 100 and MHR-T 250 LVDTs, corresponding to the *short* and *long* type respectively, to investigate the relationship between temperature change and voltage output, looking for an explanation of such unexpected behavior.

For each sensitivity test, the base of the cell (including LVDT connection pins) was taken to the heat chamber and the testing LVDT device was connected. Then, the LVDT was placed horizontally in a flat cell surface and the core was positioned inside the housing at a static position and initial voltage output (V_i). Finally, the temperature of the chamber was raised in steps. The temperature and reading output were left to stabilize before moving to the next temperature step. Since during the tests, the positions of the core and housing are not changing; any change in the voltage output during heating must be caused by electric properties alterations. In the first test, two short LVDTs were positioned with the core at similar initial voltage outputs and the heating process was carried out, it can be seen in Figure 5.5 that the response is quite similar and. In a second test, the same LVDTs were tested with the core at a different voltage value, higher than first test, the results in Figure 5.6 show that the behavior is very different comparing to the first test. Then, long LVDTs were tested (Figure 5.7) to compare the behavior with the short type LVDTs and as expected, the behavior was significantly different between the two different types.

Looking at these results, it was evident that temperature sensitivity effects depend on the type/size of LVDT. For the next test, the same LVDTs were tested but this time the cores were placed at different initial voltage values and different results in all the LVDTs were obtained. At this point, it was possible to conclude that LVDTs heat sensitivity depends not only on the model of the device but also on the position of the core relative to the zero voltage value (when the core is located exactly in the center of the head) where temperature effects are minimum.

To adequately characterize the temperature sensitivity behavior of each type of LVDT, complementary tests were conducted for a wide range of initial voltage values and also an entirely different set up/cell was used to compare the results. In Figure 5.8 and Figure 5.9 all the results are plotted together as a relation of voltage change versus temperature change for different initial voltage values (Vi) for the two type of sensors.

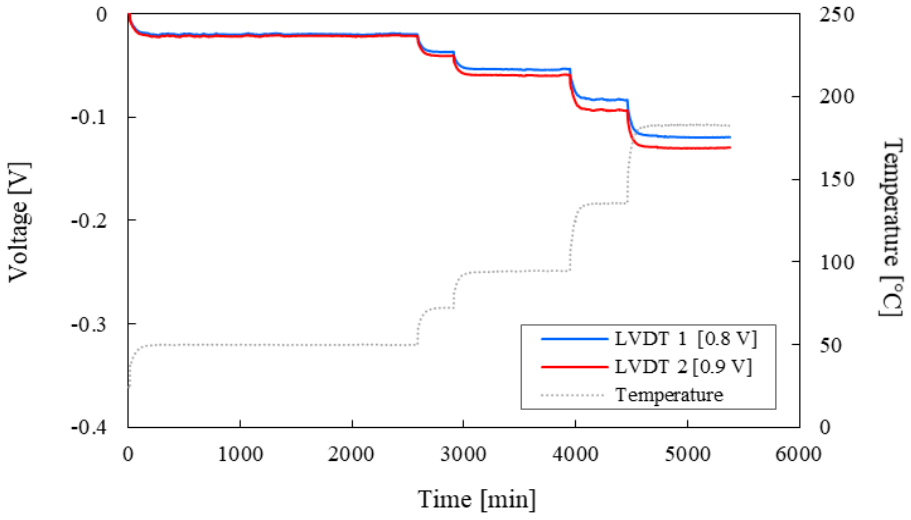

Figure 5.5: Short type LVDT sensitivity test at 0.9 V average voltage.

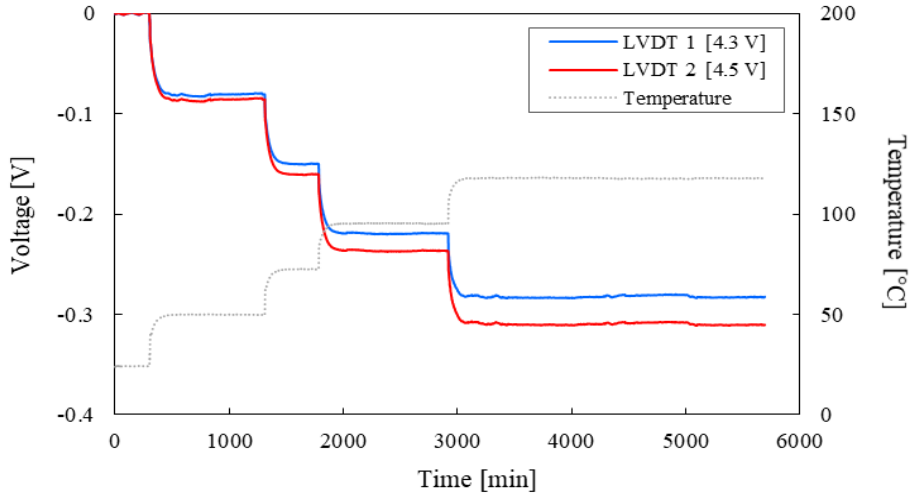

Figure 5.6: Short type LVDT sensitivity test at 4.4 V average voltage.

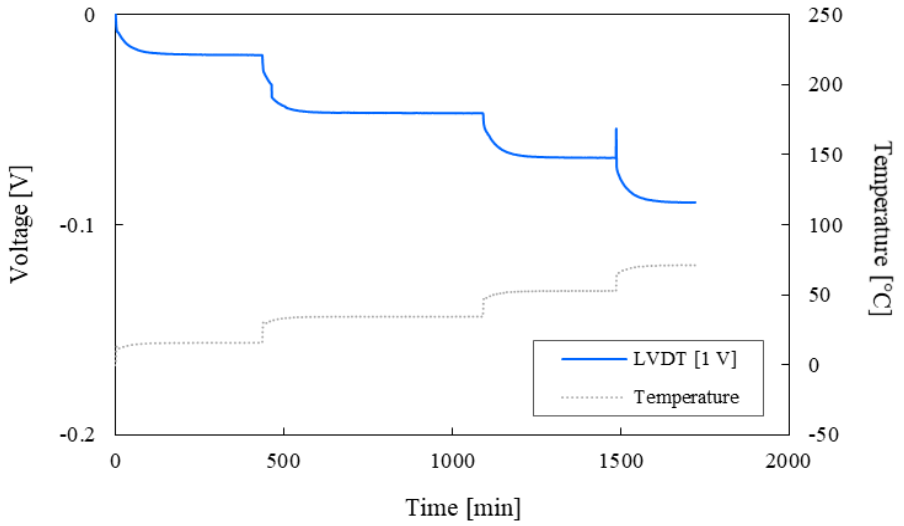

Figure 5.7: Long type LVDT sensitivity test at 1 V average voltage.

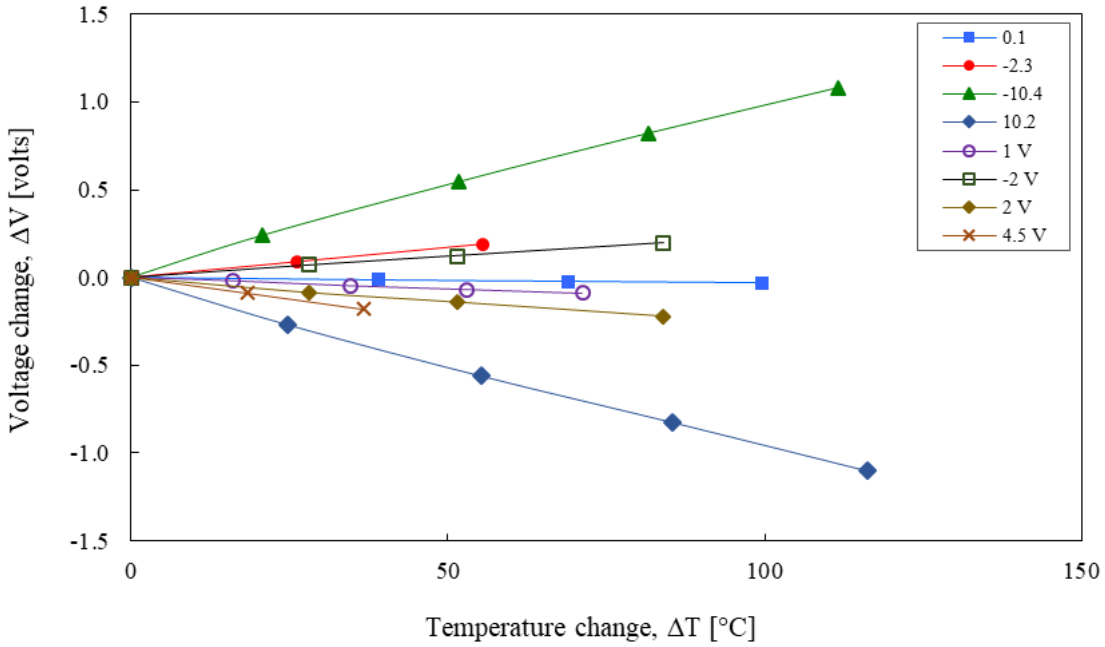

Figure 5.8: Temperature sensitivity tests for different initial voltage values in the long type LVDT.

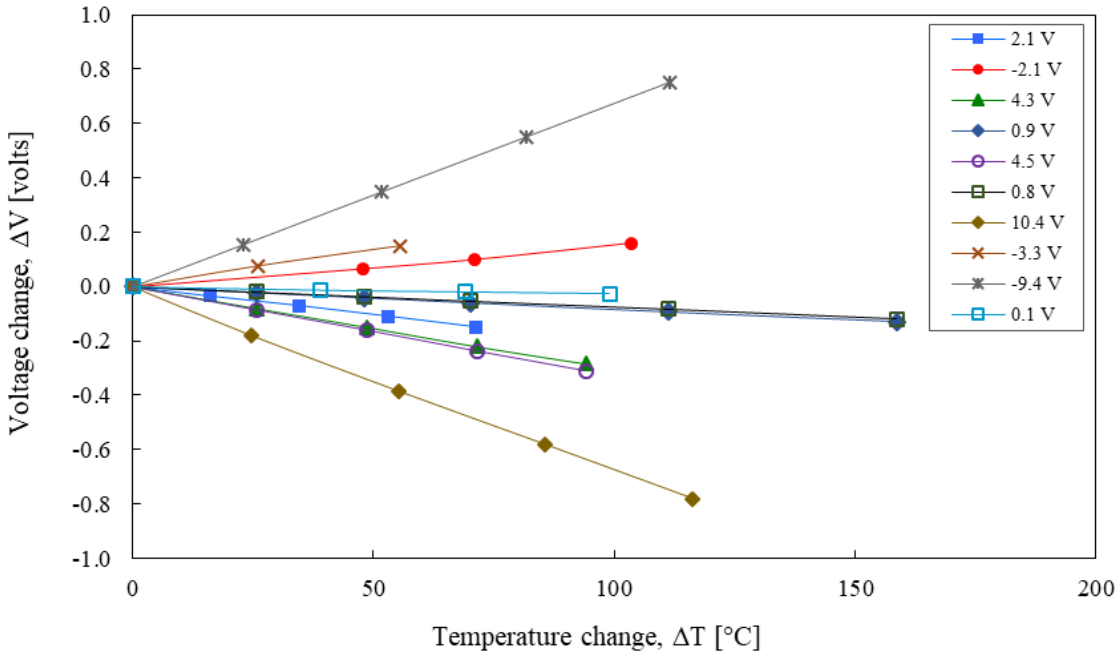

Figure 5.9: Temperature sensitivity tests for different initial voltage values in the short type LVDT.

In order to find a correlation between initial voltage and temperature effect, Figure *5.10* was generated using the different moduli values ($\Delta V/\Delta T$) calculated above. The results of both devices showed a consistent trend and exhibited a good approximation to a linear regression, indicating that linear functions of slope -0.00068 (η_{short}) and -0.00095 (η_{long}) describe the temperature sensitivity behavior of each LVDT type and are independent of the set up used and the LVDT mechanical displacement calibration. The linear functions can be used to find the thermally induced voltage output for a specific core position.

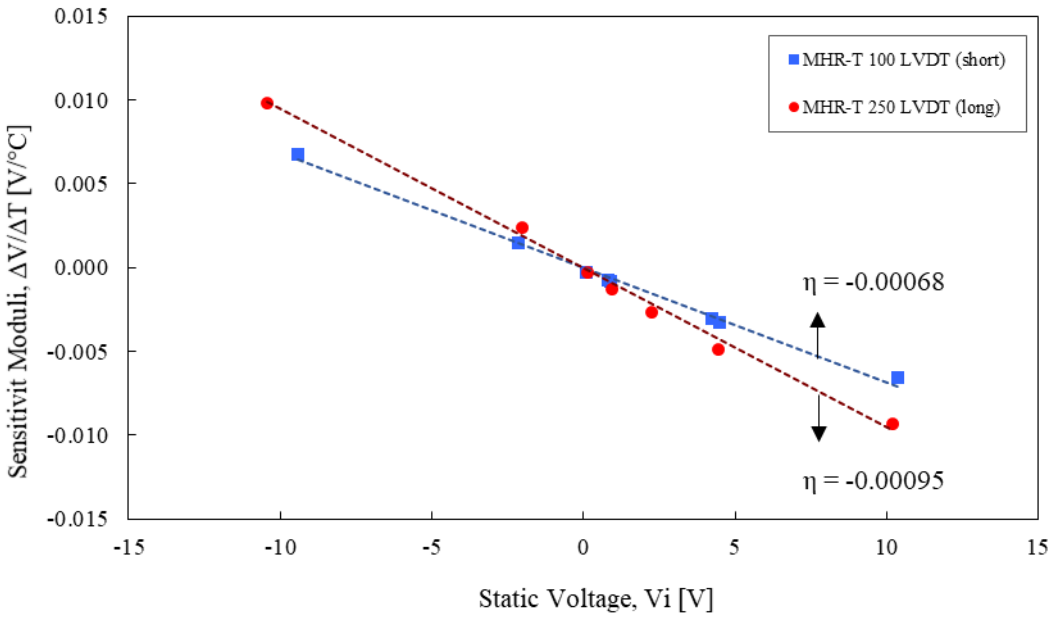

Figure 5.10: Temperature sensitivity moduli, η, of LVDTs MHR-T 100 and MHR-T 250.

To conclude, it is important to be aware of the many ways temperature can affect the testing process. We recommended testing every device and mechanical set up parts exposed to the high temperatures regardless of the manufacturers' specifications. In this case, the output signal of the LVDTs is affected by temperature variations in two ways: change in electrical properties and mechanical expansion. The alteration in electric properties caused by resistance variations in the coil of the LVDT causes a scale-factor change or span-shift error. The expression to find the induced electrical parasite voltage in the LVDT can be expressed as:

$$\Delta X_{electrical} = \eta \times V_i \times dT \times A_{LVDT} \tag{5.12}$$

where η is the correction factor for the specific LVDT type, V_i is the initial voltage, dT is the temperature change and A_{LVDT} is the displacement calibration coefficient of the LVDT for the specific system and pin port where it is connected in the test.

The mechanical expansion of the set up and LVDT holding parts causes a relative movement between the core and the head of the LVDT, generating a zero shift error in the recorded output. The correction factor due to mechanical thermal expansion effects can be obtained with a compliance test of the cell, if the initial voltage and therefore η are known.

As a reference, the LVDTs used in the high temperature isotropic system test are summarized in Table 10, where the subscripts L and S stand for long and short, respectively.

Table 5.2: LVDTs used in the high temperature isotropic system

TEST	LVDT used to measure deformation:		
	$Axial_1$	$Axial_2$	Horizontal (from radial)
Aluminum (calibration)	*Long* ($LVDT_{A1\text{-}L}$)	*Long* ($LVDT_{A2\text{-}S}$)	*Short* ($LVDT_{R\text{-}S}$)
Clearwater	*Long* ($LVDT_{A1\text{-}L}$)	*Long* ($LVDT_{A2\text{-}L}$)	*Short* ($LVDT_{R\text{-}S}$)

Isotropic Cell LVDT Temperature Sensitivity Calibration

The measured linear change can be described as the sum of mechanical deformation and electrical alterations as expressed below:

$$\Delta X_{measured} = \Delta X_{mechanical} + \Delta X_{electrical} \tag{5.13}$$

Where the electrical alterations come solely from electrical errors and mechanical deformations are caused by the real deformation of the tested sample and mechanical deformation of the system:

$$\Delta X_{mechanical} = \Delta X_{real} + \Delta X_{mechanical\ error} \tag{5.14}$$

Therefore, the measured metric change is now defined as the sum of the actual sample's linear deformation plus false or error readings caused by mechanical and electrical alterations generated from temperature shifts as expressed below:

$$\Delta X_{measured} = \Delta X_{real} + \Delta X_{\substack{mechanical \\ error}} + \Delta X_{\substack{electrical \\ error}} \quad (5.15)$$

In the above expression, electrical and mechanical errors are unknown and they are computed using η_{short} or η_{long} for each time step using the equation presented in the previous page. The ultimate purpose of the compliance test is to find the mechanical error or mechanical correction factor of the cell on each axis, radial and axial. Figure 5.11 and Figure 5.12 show the results of the displacement output in the axial component for the two different LVDT types. It can be observed that total error is dominated mainly by electrical span error, which is almost equal to the correction factor while the mechanical correction is very small. It seems that the LVDT mounting system, pedestal, and top cap are expanding simultaneously, resulting in a small mechanical deformation error. Comparing the system's mechanical error for each LVDT type in the axial axis, the difference is very small and we believe it is caused by the different LVDT sizes, thus, two different axial mechanical correction factors are calculated. Figure 5.13 shows the radial component, the errors have a different conduct due to the physical configuration of the pieces holding the radial LVDT. In this scenario, mechanical expansion has a big influence in the displacement output and has larger correction factor. The expansion of the radial chain generates a false contraction signal that tends to compensate the false displacement expansion output induced by temperature increase in the electrical performance of the LVDT resulting in underestimation of measured deformation. It is worth stating that while thermally induced mechanical error is a constant for every test using the same set up configuration, the electrical error is unique for every test and is function of the initial voltage, temperature change and mechanical deformation (error and sample) of each time step.

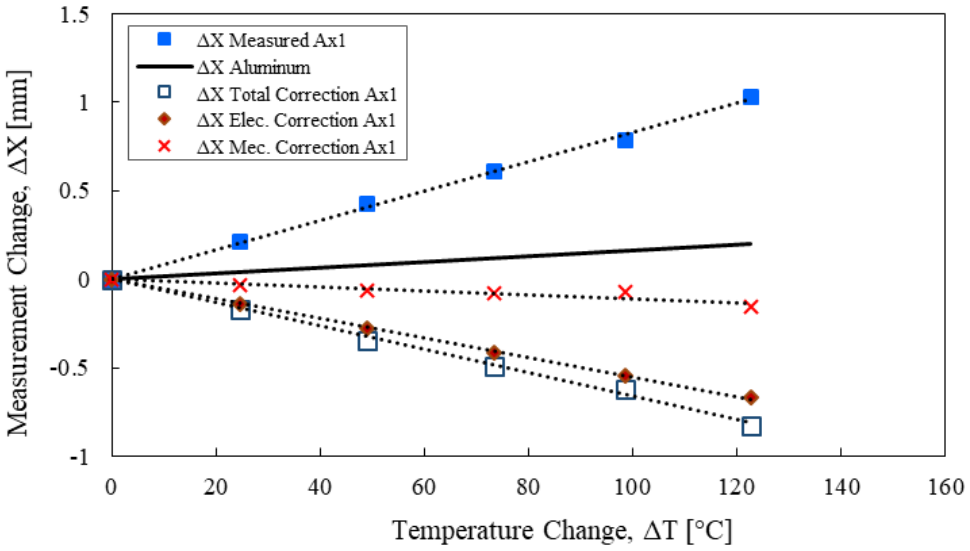

Figure 5.11: Isotropic cell mechanical calibration. Axial axis#1 (MHR-T 250 LVDT).

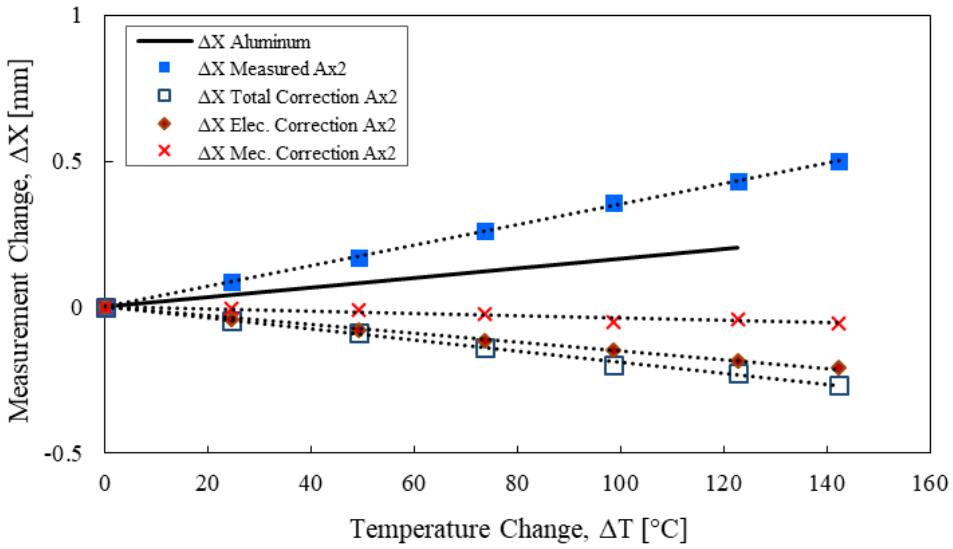

Figure 5.12: Isotropic cell mechanical calibration. Axial axis#2 (MHR-T 100 LVDT).

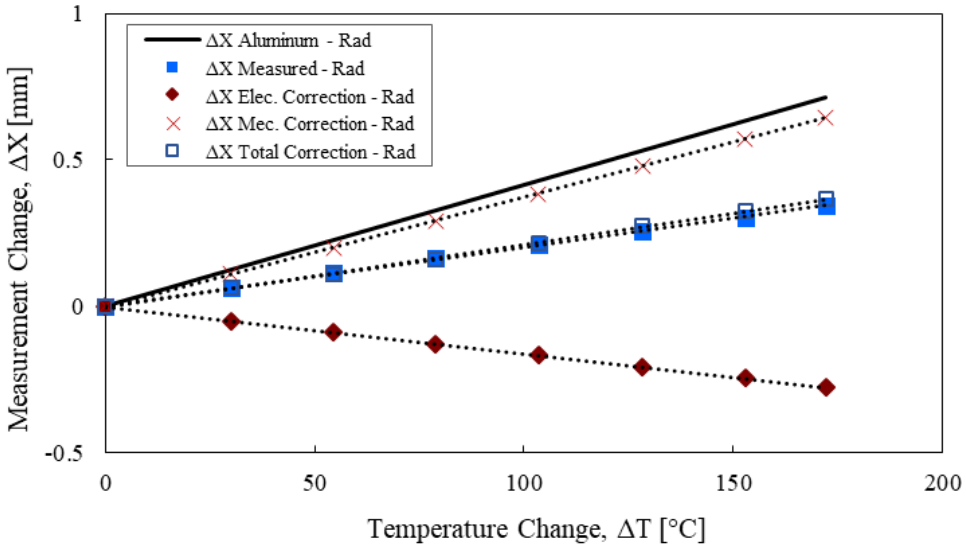

Figure 5.13: Isotropic cell mechanical calibration. Radial axis#1 (MHR-T 100 LVDT).

5.3.3 One-Dimensional Thermal Creep Tests

The most common equipment used to measure thermally induced volumetric strains is the oedometer cell. As explained before, the oedometer cell is the popular choice for compressibility tests, since it simulates axisymmetric strain conditions similar to in-situ deformations in relatively shallow depths.

The set-up of the high-temperature odometer system is shown in Chapter 2. After the system was assembled, the coolant system was turned on until the system's temperature was stable. Two intact Clearwater samples T_Od4 and T_Od5 described in Chapter 2 were tested but results from T_Od4 are discarded since the LVDT was very unstable and it was not possible to define a consistent trend. The sample of T_Od5 was consolidated to its in-situ effective stress state ($\sigma v'$ = 3.5 MPa), creep was allowed at this condition until a representative secondary compression line was observed. From this point, a drained multi-stage thermal loading test from 15°C to 180°C was performed, while the in-situ effective stress conditions were maintained constant. The thermal loading stages were 15°C, 50°C, 100°C, 150°C, and 190°C. The heating rate was set up as 0.04 °C/min using a ramp function, the same rate was used for every temperature increment, and the average duration

of each stage was 10,000 min (one week). With these long testing times, sufficient time elapsed to capture the thermal creep behavior of the specimen.

5.3.4 Isotropic Thermal Creep Tests

A multi-stage isotropic heating test from 25°C to 150°C was performed under in-situ effective stress conditions ($\sigma v'$ = 3.5 MPa) on sample #43-1 stopping at 25, 50, 100, and 150 °C. The idea was to reach 180°C, but the axial LVDTs failed after they were heated to 150°C. The details of the equipment were provided in Chapter 2. The sample set-up was the same as the one used for creep tests in Chapter 4, except that instead of using a latex membrane, a heat-resistant Teflon shrink membrane was used.

The sample was saturated and loaded to in-situ conditions at room temperature (23°C +- 0.5°C) and was allowed to creep for a significant amount of time to obtain a creep index magnitude. Then, we increased the temperature in stages to 25°C, 50°C, 100°C, and 150°C controlling the heat rate with a ramp function for a temperature increase of 0.04 °C/min. The idea was to reach 180°C but the axial LVDTs failed after they were heated to 150°C even though they were high-temperature LVDTs. At each stage, the temperature was allowed to stabilize; afterward, the deformation was recorded for at least 10,000 minutes per stage.

5.4 EXPERIMENTAL RESULTS AND DISCUSSION

Using equations 3.5 and 3.6, volumetric strain was calculated for the multi-stage thermal creep experiments T_Od5 and T_Is4, respectively. On every stage of both test conditions (isotropic and one-dimensional), a compression behavior was observed. Results from heating tests (Cekerevac, C.; Laloui, 2004; Cui et al., 2009; T. Hueckel and G.Baldi, 1990) showed an interesting phenomenon where the specimen would change from contraction to expansion as the overconsolidation ratio increases thus demonstrating that heat-induced volumetric strain is dependent on the OCR of the material.

5.4.1 Thermal Creep Oedometer Tests

After applying the adequate corrections of parasite thermal strains of the system, the volumetric strain was calculated for each temperature stage of T_Od5 test. The results of the axial strains, in this case the volumetric strains, are shown from Figure 5.14 to Figure 5.17. Working with elevated temperatures and LVDTs can be challenging since the electromagnetic field is greatly affected by heat, and even though extensive precautions are taken, sometimes it has unexpected reactions. For this reason, we can observe some data gaps in 50°C and 100°C stages, but in this case, the analysis was not affected at all.

It can be noticed from the figures that minimum to zero expansion occurred during initial times. On the contrary, compression and thermal creep behavior occurred at all stages, where temperature acts as the loading component.

Many concepts of conventional multi-stage creep tests can be noticed here. When the temperature is increased, the sample experiences compression behavior at every stage at the highest compression rates of the test. Once the temperature reaches a constant value, the compression rate decreases and follows a constant rate. Since temperature and effective stress are constant, the compression behavior that follows temperature stabilization is pure thermal creep. It can be inferred from the plots that pore pressure dissipates when the slope breaks, and it happens almost right after temperature stabilizes. This means that the temperature loading rate was indeed adequate, and pore pressure was able to dissipate quickly. In the 100°C stage, the temperature controller was not responding correctly. As can be seen from the temperature curve, the ramp function was not the same constant 0.04°C/min used in the other stages. This change caused a different behavior in the curve, and it was not possible to identify when pore pressure dissipates, and pure thermal creep starts. Similar to the creep behavior of a stress increase stage where the loading rate is too slow, or the step increase is very small, pore pressure dissipation is so small that creep dominates the compression behavior.

The limitations of the oedometer apparatus for thermal expansion/compression tests have been discussed before. The expansion of the oedometer ring and the impossibility to measure an accurate lateral effective stress are the most critical issues. The

main consequence is a higher strain allowed in the horizontal direction; thus, we must be aware that the results might indicate higher volumetric compressions.

Temperature and stress have a time-dependent component in the deformation of Clearwater clay-shale, and likewise, the time has a critical role in every calculation. To calculate the thermal expansion coefficient of materials that do not experience creep, arbitrary times can be used. However, to calculate the thermal compression coefficient of Clearwater, careful attention to the time chosed for the calculation. Figure 5.18 shows two thermal compression lines calculated for Clearwater, on both cases, the strain was normalized to the 3.5 MPa stage, but we cannot use the strain difference from room temperature to 50°C. Points can only be plotted together if they share the same conditions of loading rate and time, this is why data points of 150°C stage do not fit the lines, and using an arbitrary point of 3.5 MPa stage at room temperature can give misleading results. It is also important to mention the importance of using nominal strains since the duration of creep affects strain of the next stage, similar to what happens in stress-induced creep tests of Chapter 4. The first line was constructed using the strains at 1,500 min, which is approximately the time where pore pressure was fully dissipated in every stage (except 150°C stage), and the second line was built from data points at 10,000 min of the test. The thermal compression coefficients obtained are -6.1E-5 [/°C] for the 1,500 min and -7.1E-5 [/°C] for the 10,000 min. Form the two lines, the importance of the time-dependent component of temperature can be recognized. Since Clearwater clay shale exhibits thermal creep, and the thermal creep index increases with temperature, the thermal compression coefficient is not unique; it is time-dependent and might have a wide range of values, similar to the compression index.

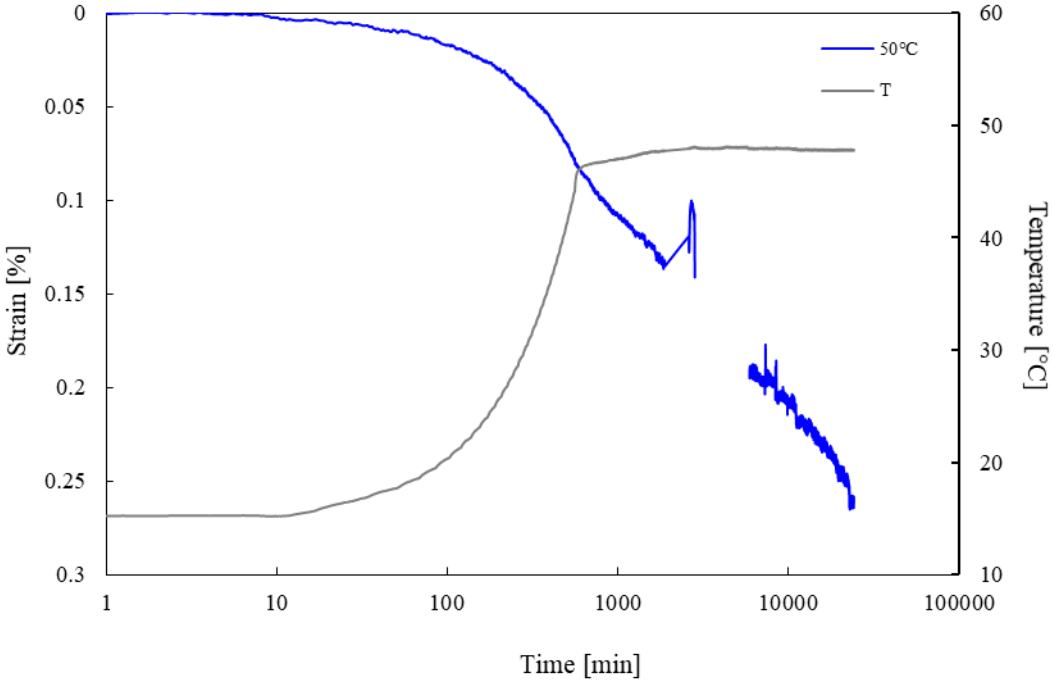

Figure 5.14: Strain from thermal creep oedometer test at 50°C.

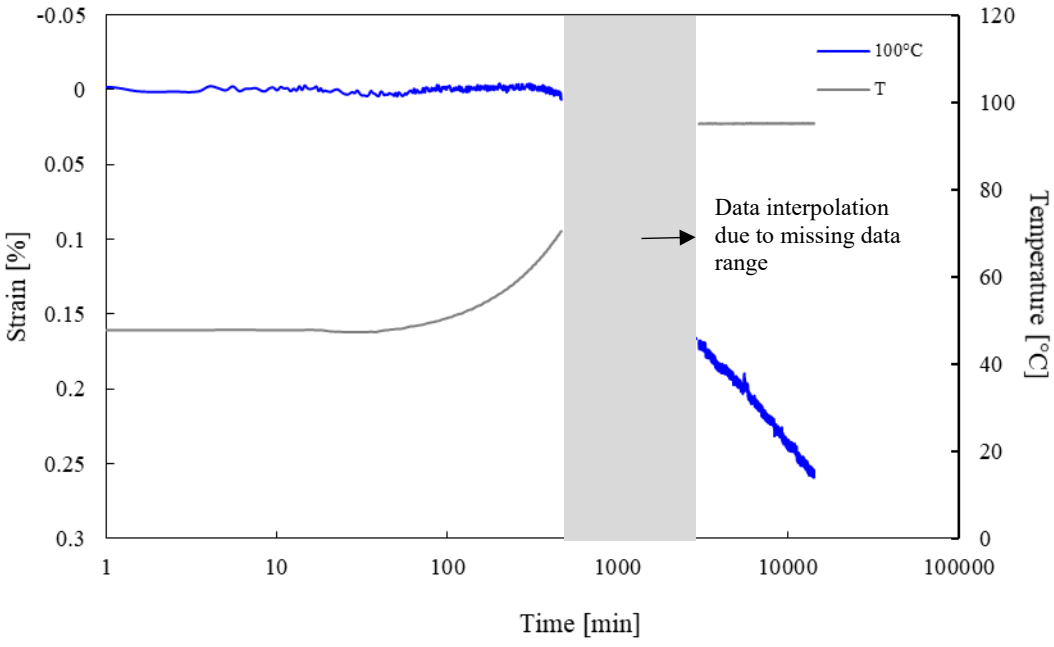

Figure 5.15: Strain from thermal creep oedometer test at 100°C.

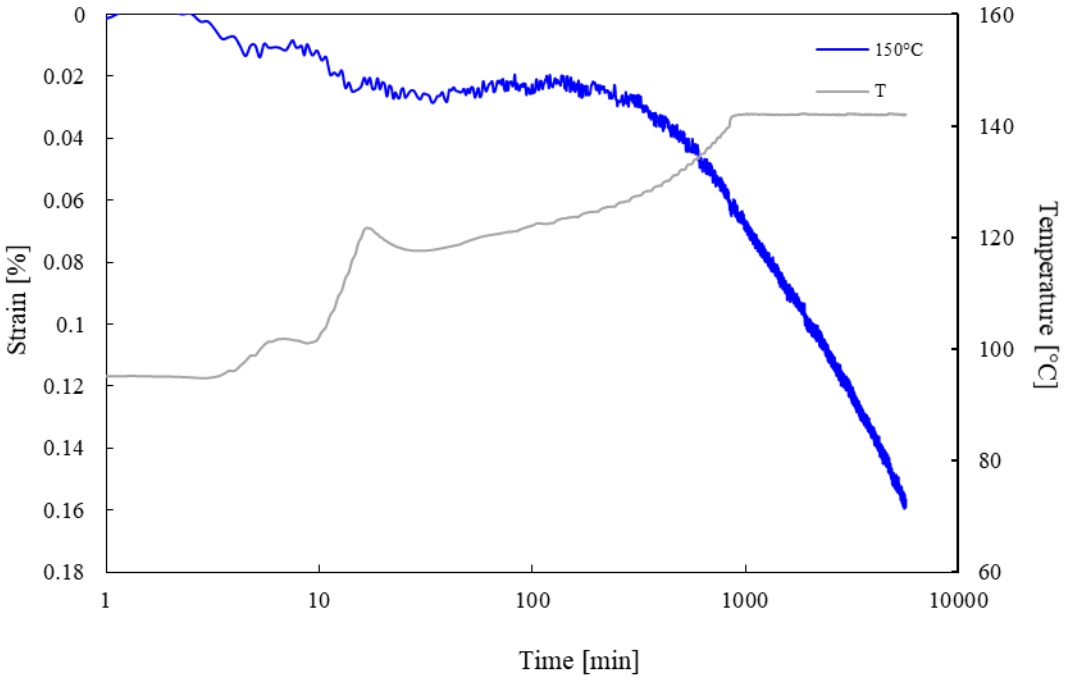

Figure 5.16: Strain from thermal creep oedometer test at 150°C.

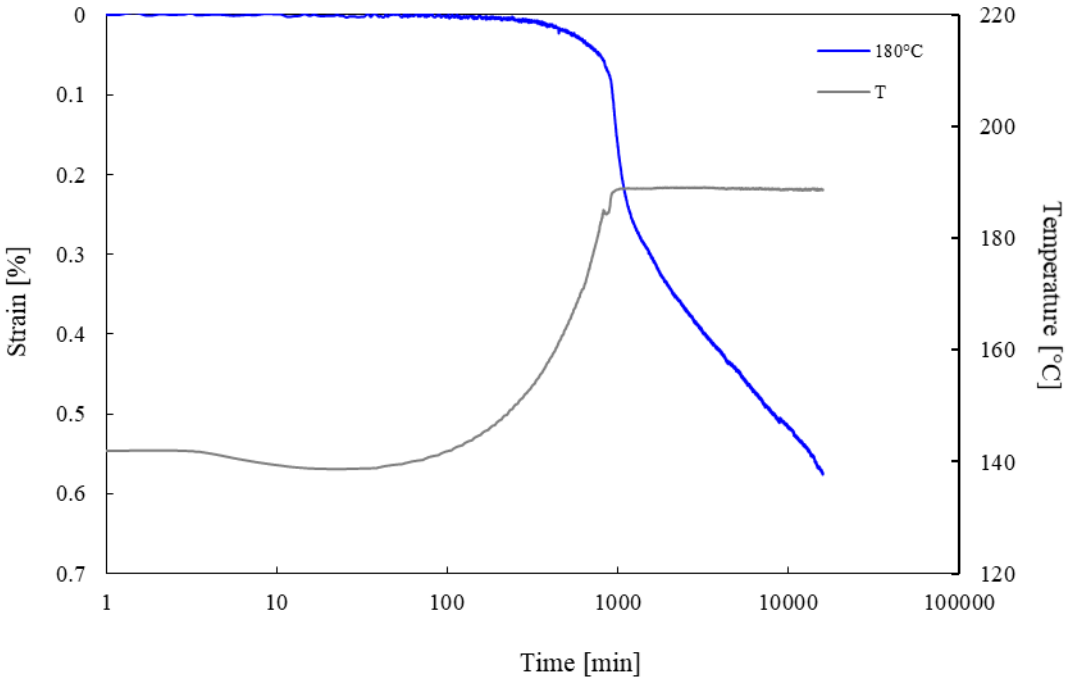

Figure 5.17: Strain from thermal creep oedometer test at 190°C.

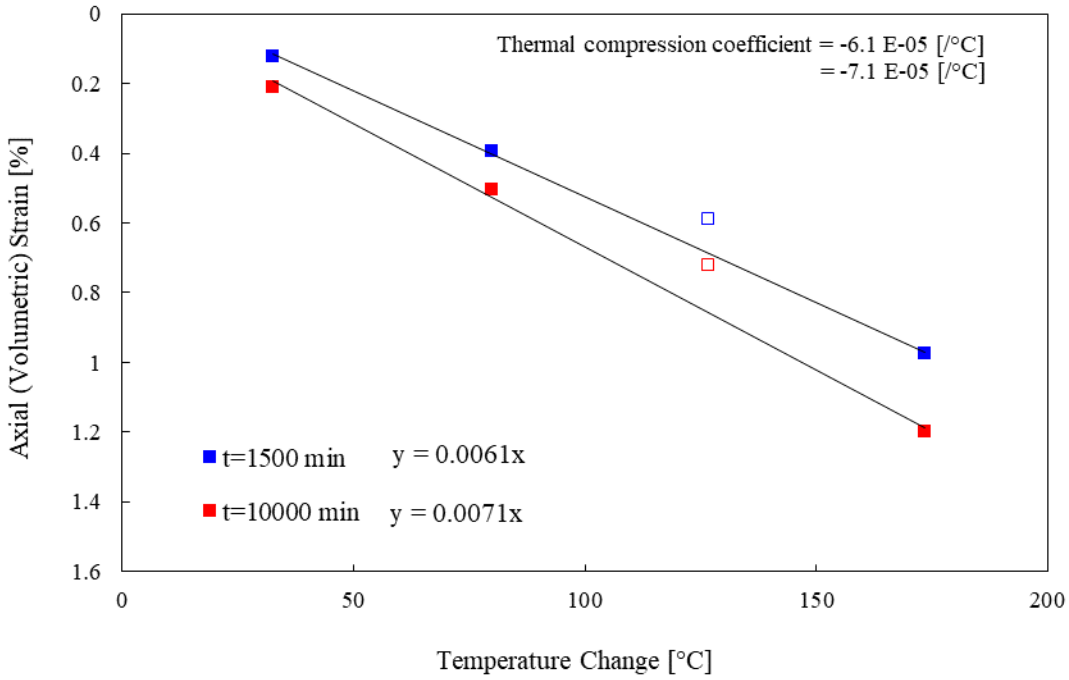

Figure 5.18: Thermal compression coefficient for different testing times.

5.4.2 Thermal Creep Isotropic Tests

Accurate volumetric strain calculations of the isotropic thermal creep test T_Is4 proved to be very challenging. The LVDTs used for the tests and described in Chapter 2, which are indeed high-temperature LVDTs, showed that the fact that the LVDTs are named high-temperature only means they can resist high-temperatures (best case scenario), it does not imply that their behavior is not affected by temperature. In §5.3.2 it was shown how the voltage high-temperature LVDTs is greatly affected by temperature, and the effects can be characterized by a sensitivity test. Different high-temperature LVDTs available in the GeoREF laboratory were tested and determined that the voltage in all of them are affected by temperature; thus, if electrical temperature sensitivity is not considered in tests where LVDTs are exposed to temperature changes, the tests will show erroneous results. Moreover, the magnitude of the corrections can exceed the magnitude of the thermal strains, which might also invalidate test results.

Figure 5.19 to Figure 5.22 show the axial, radial, and volumetric strain results of creep at room temperature, 50°C, 100°C, and 150°C. Long-type axial LVDTs failed at 150°C and it was not possible to conclude the test and reach 180°C. In the figures, gray lines represent the data affected by temperature with corrections applied, and blue, green, and red lines show results independent of thermal calibrations. It is worth noting that LVDT or strain deformation measurements take more time to stabilize after the temperature reaches a constant value compared to oedometer test results. Temperature stabilizes faster in the oedometer cell since the heating rods are closer to the sample and the heating medium was the stainless steel solid cell, on the other hand, the isotropic cell is heated inside a chamber with is air, steel, and oil as the heating medium before reaching the sample.

For this reason, curves show a sharp variation and not a smooth line after corrections are applied, but in reality, it should be a smooth trend. In our T_Is4 test, parasite readings of the LVDTs during the heating process are laree due to the set-up of the LVDTS and their exposure to direct heat, as explained previously. Challenging compliance conditions, and correction factors with a larger order of magnitude than real strain deformations take place during temperature increase and before temperature stabilized, making very difficult an accurate strain quantification; hence, just an approximation is possible. The huge correction magnitudes relative to the creep strains of the test data produce a high degree of uncertainty around the nominal volumetric strain results. Consequently, caution is urged in interpreting a thermal contraction coefficient from these results. However, after temperature stabilizes ($\Delta T = 0$) no more corrections are in effect, and thermal creep data from that point onwards is independent of calibrations. Thus, the thermal creep indexes of each temperature stage can be calculated and are revealed below. We can also observe that thermal creep is dominated by the anisotropic behavior of Clearwater; radial thermal creep rates are smaller than axial creep rates.

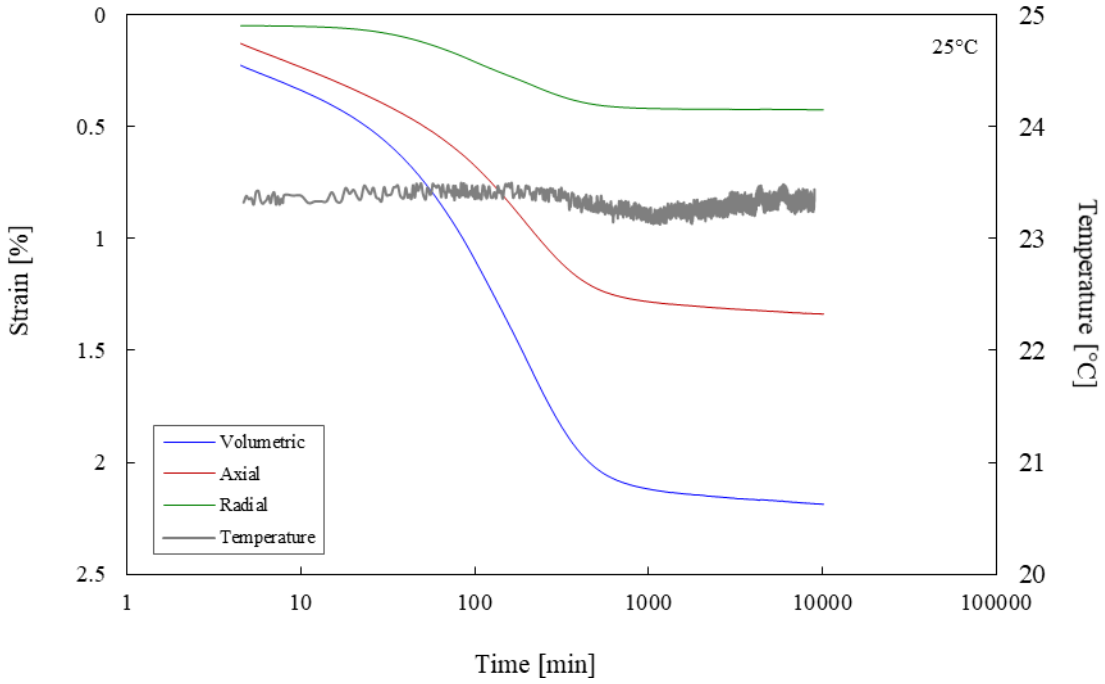

Figure 5.19: Strains from thermal creep isotropic test at 25°C.

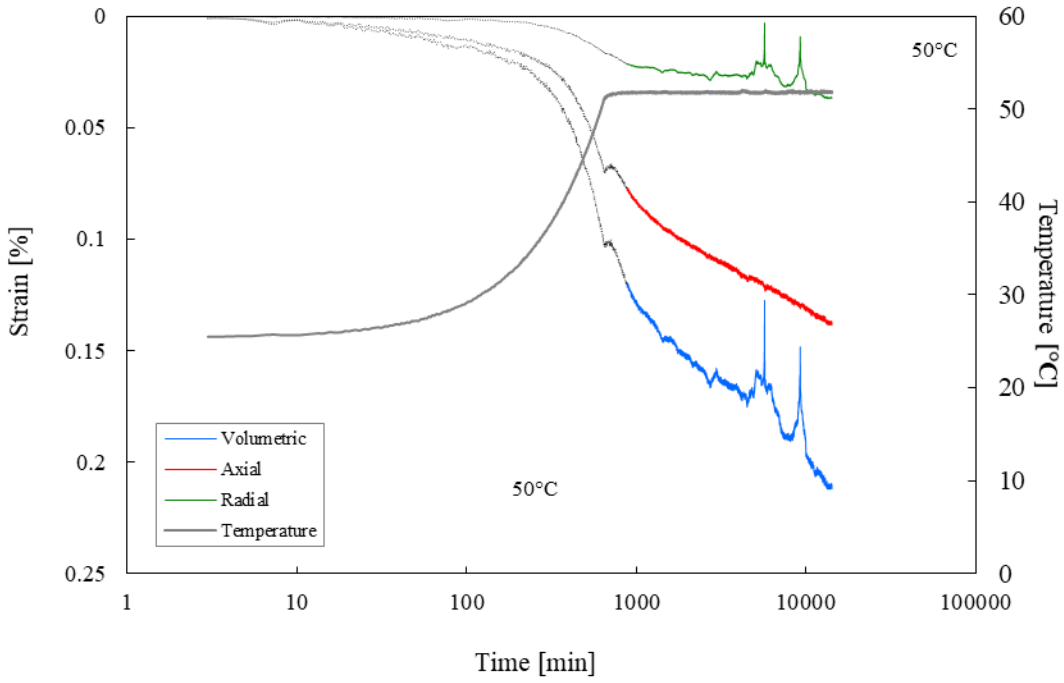

Figure 5.20: Strains from thermal creep isotropic test at 50°C.

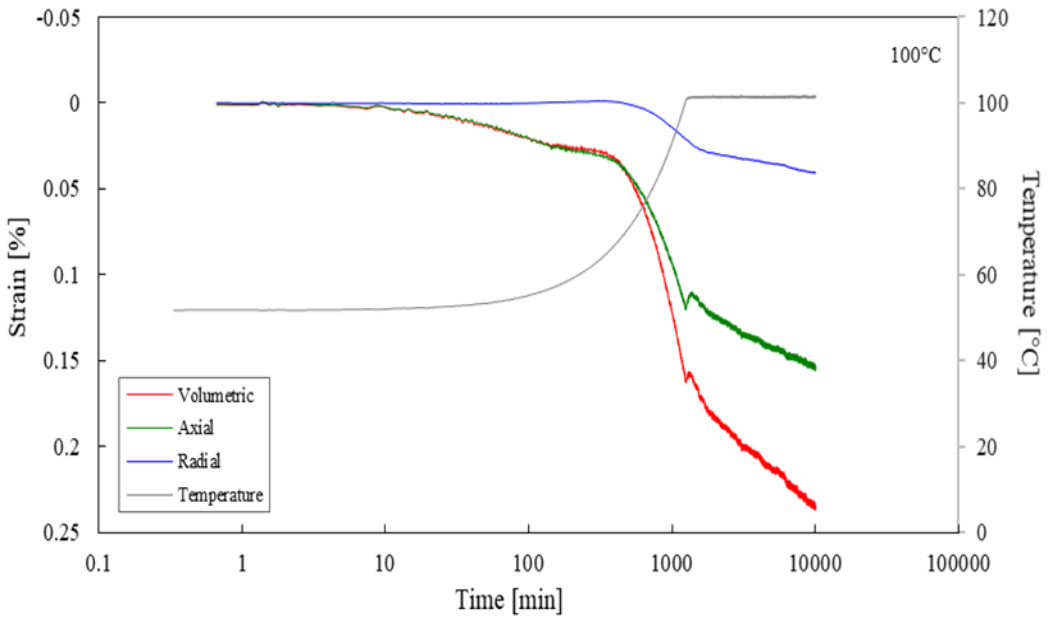

Figure 5.21: Strains from thermal creep isotropic test at 100°C.

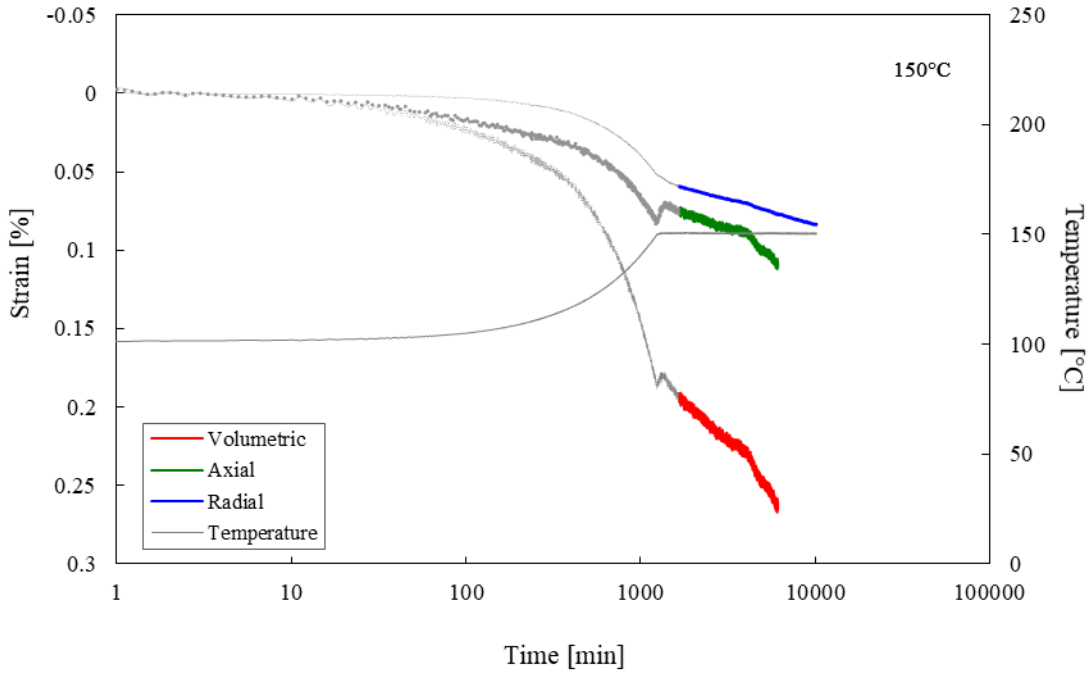

Figure 5.22: Strains from thermal creep isotropic test at 150°C.

5.4.3 Effects of Temperature on Creep Rate

In Figure 5.23, we plotted the creep indices obtained from all tests at 3.5 MPa effective stress in-situ conditions, including creep indices from CI_Od1, CI_Od2, CI_Is1, CI_Is2 and creep indices from the thermal creep tests T_Od5 and T_Is4. In the oedometer tests, as seen before, the creep rate is relatively constant on each stage after pore pressure dissipates; a chained-line show the behavior that Clearwater follow under oedometer creep conditions. For the isotropic tests, creep indices plotted for CI_Is1, CI_Is2 correspond to middle times. Creep indices of early creep stages or right after the end of primary EOP are not used since thermal loading rates are very slow compared to the stress loading rates of CI_Is1, CI_Is2. As shown in Chapter 4, slower loading rates delay EOP time and creep index after EOP corresponds to later times. In Figure 5.23 a strong correlation between temperature and thermal creep index for each test method is shown. Results indicate a significant increase in the creep rate due to increasing temperature. Comparing the two resulting trends, it can be seen that the creep index of Clearwater clay shale is also dependent on test boundary conditions. The difference between both lines increases with temperature as the creep index of the isotropic test is less affected by temperature. As explained previously, the oedometer ring expands with increasing temperature and releases the horizontal stress, allowing the sample to deform almost freely in the horizontal direction, resulting in higher volumetric creep strains for thermal creep tests performed in the oedometer.

In both scenarios, drainage was allowed to occur efficiently, and the excess pore water pressures dissipated when the temperature reached the target value, leading to a time-dependent compression of Clearwater. A thermal cycle produces effects of overconsolidation similar to those caused by creep alone, and an important consequence of thermal creep might be creep-induced closure of fissures.

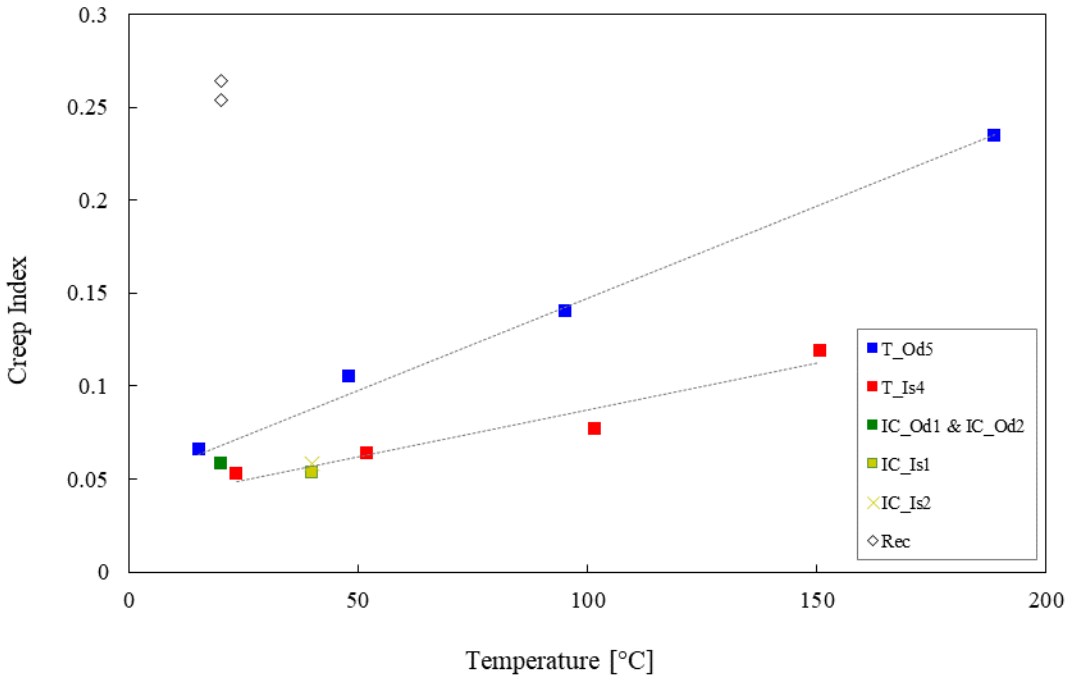

Figure 5.23: Creep index of all the isotropic and oedometer tests at 3.5 MPa effective stress and different temperatures.

CHAPTER 6: CONCLUSIONS AND RECOMMENDATIONS

CONCLUSIONS

This research aimed at improving our understanding of the behavior of Clearwater caprock relating the time-dependent compression behavior of Clearwater material under the influence of stress and temperature. Nine long-time multi-stage creep tests were performed on intact and reconstituted samples using two types of loading paths; mechanical loading at a given constant temperature, and thermo-mechanical loading where the samples were subjected to thermal loading under constant effective stress conditions. Strains were recorded using high accuracy instrumentation and calibrations. Based on the results that have been presented in this study, the main conclusions are discussed below:

- The veracity of experimental test results rely on accurate conversions of a measurement system's electrical output to engineering units. Creep tests require high sensitivity calibrations. For the tests involving temperature variations it was found that additional calibration considerations were required, like LVDT temperature sensitivity experiments proposed in this study.
- The intrinsic properties of Clearwater material are consistent with those from Burland's studies on ICL. According to the position of the in-situ effective stress of the intact compression curves relative to the ICL and SCL, Clearwater clay shale has a strong enhanced resistance due to structure (fabric and bonding) developed from processes like creep and diagenesis.

- The maximum testing pressure selected (14 MPa) was not large enough to identify a clear threshold pressure and the NCL was not reached. However, a destructuration zone was identified from the normalized intact compression lines. Consequently, $C5$ drastically increases with effective stress, and consequently, $C<$ values are actively increasing with time; the $C<$ index also exhibits a proportional behavior with the effective stress. However, in the oedometer tests $C<$ remained constant with time.

- While there was a unique EOP $\varepsilon - \log \sigma'$ curve for each loading method, infinite compression curves can be obtained from times greater than the time to reach primary consolidation, t_p, due to Clearwater's time dependent compression component. These creep strains have a similar effect to that of over consolidation caused by aging. Moreover, the analysis of after creep tests SEM pictures showed that the material becomes more compact and healed fissures.

- The C_α / C_c law of compressibility was studied for Clearwater clay shale. Most of the data successfully followed a linear trend that characterize Clearwater material.

- From isotropic tests, it was possible to identify the strong anisotropic compression behavior of Clearwater. The samples had a preferred direction of contact forces in the horizontal orientation, thus, axial strains were higher than radial strains, and the difference decreased when effective stress increased; This means reduced anisotropy with effective stress, while in the oedometer specimens there was an evolving state of anisotropy.

- Temperatures acts as a loading component in Clearwater. When the temperature was increased, the sample experienced compression behavior at every stage. Once temperature reached a constant magnitude, thermal creep preceded. This indicates that temperature have a time-dependent component in the deformation of Clearwater clay-shale, and likewise, the time has a critical role in every calculation.

- Clearwater has a negative time-dependent coefficient of thermal deformation.

- The creep index of Clearwater clay shale is dependent on test boundary conditions since a strong correlation between temperature and thermal creep index for each test method was observed. Where there's a significant increase in the creep rate due to increasing temperature.

The results from this study allow us to develop more realistic constitutive models for Clearwater clay-shale caprock, which results in more reliable predictions for reservoir containments studies in SAGD projects.

RECOMMENDATIONS FOR FURTHER RESEARCH

Recommendations based on the observations, experience, and the results of this investigation are as follows:

- Study the strength properties of Clearwater under different creep effective stresses and different deviator stresses. Analyze under which conditions creep and thermal creep operate as a hardening mechanism and what is the deviator threshold value that accelerates creep rate, leading to a potential caprock fail. Triaxial tests on samples after primary consolidation (without creeping) and samples after some period of creep can be useful to analyze how creep changes the strength parameters of the material.

- Additional consolidation tests at higher effective stresses are required to characterize Clearwater's preconsolidation pressure accurately.

- It could be useful to find how cam-clay yielding envelope (including cap) changes with temperature, if it is softening or hardening. Some results show that thermal expansion up to a certain temperature is followed by contraction investigate and explain this value.

- Study new methodologies to perform creep tests that reduce or minimize parasite measurements induced in high-temperature tests.

- Numerical simulation of creep behavior (isotropic and anisotropic creep models) aiming to achieve a good match with experimental data. Implications of creep behavior and thermal creep in numerical simulation models and how caprock integrity studies (factor of safety) are affected.
- Strain softening behavior might be happening in the caprock. The present study made available data of creep tests on reconstituted samples than can be further analyzed.

REFERENCES

Abuel-Naga, H. M., Bergado, D. T., Soralump, S., & Rujivipat, P. (2005). Thermal consolidation of soft Bangkok clay. *Lowland Technology International*, *7*(1), 13–21.

AER. (2016). Directive 086-Reservoir COntainment Application Requirements for Steam-Assisted Gravity Drainage Projects in the Shallow Athabasca Oil Sands Area.

AER. (2020). *ST98 2020*.

Aghabarati, M., & Chalaturnyk, R. (2017). *Reanalyzing Thermocouple Temperature Response for Evidence of Convective Flow: Master's Thesis*. University of Alberta.

Alberta Energy Regulator. (2016). *Directive 086: Reservoir Containment Application Requirements for Steam-Assisted Gravity Drainage Projects in the Shallow Athabasca Oil Sands Area*.

ASTM. (2005). D4318-10: Standard Test Methods for Liquid Limit, Plastic Limit, and Plasticity Index of Soils.

ASTM. (2010). D2216-10: Standard Test Methods for Laboratory Determination of Water (Moisture) Content of Soil and Rock by Mass. https://doi.org/10.1520/D2216-10.N

ASTM. (2011). D2435-04: Standard Test Methods for One-Dimensional Consolidation Properties of Soils Using Incremental Loading.

ASTM. (2014). D854-14: Standard Test Methods for Specific Gravity of Soil Solids by Water Pycnometer.

ASTM. (2017). F2537: Standard Practice for Calibration of Linear Displacement Sensor Systems Used to Measure Micromotion.

Augustesen, A., Liingaard, M., Lade, P. V, & Asce, M. (2004). Evaluation of Time-Dependent Behavior of Soils, (September), 137–156.

Bell, J. S., Price, P. R., & McLellan, P. J. (1994). *In-situ Stress in the Western Canada Sedimentary Basin*.

Belmokhtar, M., Delage, P., Ghabezloo, S., & Conil, N. (2017). Thermal Behaviour and Creep of the Callovo-Oxfordian Claystone. *Poromechanics 2017 - Proceedings of the 6th Biot Conference on Poromechanics*, *c*(2013), 839–846.

Belmokhtar, Malik, Delage, P., Ghabezloo, S., & Conil, N. (2017). Thermal Volume Changes and Creep in the Callovo-Oxfordian Claystone. *Rock Mechanics and Rock Engineering*.

Brantut, N., Heap, M. J., Meredith, P. G., & Baud, P. (2013). Time-dependent cracking and brittle creep in crustal rocks: A review. *Journal of Structural Geology*, *52*(1), 17–43.

British Petroleum. (2020). *Statistical Review of World Energy*.

Burghignoli, A., Desideri, A., & Miliziano, S. (2011). A laboratory study on the thermomechanical behaviour of clayey soils. *Canadian Geotechnical Journal*, *37*(4), 764–780.

Burland, J. B. (1990). On the Compressibility and Shear Strength of natural Clays, (3), 329–378.

Campanella, R. G. and Mitchell, J. K. 1968. Influence of temperature variations on soil behaviour. Journal of the Soil Mechanics and Foundation Division, ASCE, 94(3): 709-734

Castellanos, B. (2013). *Use and Measurement of Fully Softened Shear Strength*. *PhD Dissertation*.

Cekerevac, C.; Laloui, L. (2004). Experimental Study of the Thermal Effects on the Mechanical Behaviour of a Clay. *International Journal for Numerical and Analytical Methods in Geomechanics*, 209–228.

Cepeda-Diaz, a. F., & Mesri, G. (1986). Residual shear strength of clays and shales. *Géotechnique*, *36*(2), 269–274.

Cerasi, P., Lund, E., Kleiven, M. L., Stroisz, A., Pradhan, S., Kjøller, C., … Fjær, E. (2017). Shale Creep as Leakage Healing Mechanism in CO2 Sequestration. *Energy Procedia*, *114*(1876), 3096–3112.

Chalaturnyk, R. J. (1996). *Geomechanics of SAGD Process in Heavy Oil Reservoirs: Ph.D.*

Thesis. University of Akberta.

Chalaturnyk, R. J., & Scott, J. D. (1992). Evaluation Of Reservoir Properties From Geomechanical Tests. *Journal of Canadian Petroleum Technology*, *31*(5).

Cotecchia, F., & Chandler, R. J. (2000). A General Framework for the Mechanical Behaviour of Clays. *Geotechnique*, *1*(4).

Cui, Y.-J., Le, T. T., Tang, A. M., Delage, P., & Li, X. L. (2009). Investigating the time-dependent behaviour of Boom clay under thermomechanical loading. *Géotechnique*, *59*(4), 319–329.

Delage, P., Sultan, N., & Cui, Y. J. (2000). On the thermal consolidation of Boom clay. *Canadian Geotechnical Journal*, *37*(2), 343–354.

Energy Resources Conservation Board. (2010). Total E&P Canada Ltd. Surface Steam Release of May 18, 2006 Joslyn Creek SAGD Thermal Operation.

Fjaer, E., Folstad, J. S., & Li, L. (2016). How Creeping Shale May Form a Sealing Barrier Around a Well. *50th US Rock Mechanics / Geomechanics Symposium*, (1), 8.

Fjaer, E., Holt, R. M., Horsrud, P., Raaen, A. M., & Risines, R. (2008). *Petroleum Related Rock Mechanics*. (Elsevier, Ed.) (Second Edi).

François, B., & Laloui, L. (2010). An Oedometer for Studying Combined Effects Of Temperature and Suction on Soils. *Geotechnical Testing Journal*, *33*(2), 112–122.

Ghassemi, R. (2016). *Time-Independent and Time-Dependent Behavior of Clearwater Clay Shale Underneath Large Storage Tanks – Laboratory Testing and Numerical Modelling: Ph.D. Thesis*. University of Calgary.

Graham, J., Crooks, J. H. A., & Bell, A. L. (1983). Time effects on the stress-strain behaviour of natural clays. *Geotechnique*, *33*(3), 327–340.

Guo, K., Li, H., & Yu, Z. (2016). In-situ heavy and extra-heavy oil recovery : A review. *Fuel*, *185*, 886–902.

Horseman, S. (2001). Self-healing of Fractures in Argillaceous Media from the Geomechanical Point of View. *IGSC Working Group on Measurement and Physical Understanding of Groundwater Flow through Argillaceous Media (CLAY CLUB)*, (May), 18–25. Retrieved

Huag, K. M., Greene, P., & Mei, S. (2014). *Geological Characterization of the Lower Clearwater*

Shale in the Athabasca Oil Sands Area, Townships 87–99, Ranges 1–13, West of the Fourth Meridian.

Hueckel, T., & Borsetto, M. (1990). Thermoplasticity of Saturated Soils and Shales: Constitutive Equations. *Journal of Geotechnical Engineering*, *116*(12), 1765–1777.

Jarad, N., & Masrouri, F. (2016). *Temperature impact on the consolidation and creep behaviour of compacted clayey soils: Ph.D. Thesis*. Université de Lorraine.

Jia, S. & Chalaturnyk, R. (2018) Physical Modeling for SAGD Caprock Integrity (Centrifuge Studies). Internal Communication Report. Reservoir Geomechanics Research Group, University of Alberta.

Josh, M., Esteban, L., Piane, C. D., Sarout, J., Dewhurst, D. N., & Clennell, M. B. (2012). Journal of Petroleum Science and Engineering Laboratory characterisation of shale properties. *Journal of Petroleum Science and Engineering*, *88–89*, 107–124.

Khosravi, E., & Ghassemi, A. (2017). Influence of temperature and anisotropy on creep behavior of Mancos shale, (November).

Kosar, K. M. (1989). *Geotechnical Properties of Oil Sands and Related Strata. Ph.D. Thesis*.

La Gatta, D. P. (1970). "Residual strength of clays and clay-shale by rotation shear tests." Rep., Harvard Soil Mechanics Ser. No. 86, Harvard Univ., Cambridge, Mass.

Laloui, L. (2001). Thermo-mechanical behaviour of soils. *Revue Française de Génie Civil*, *5*(6), 809–843.

Leonards, G. A., and Ramiah, B. K. (1960). "Time effects in the consolidation of clays." STP 254, ASTM, Philadelphia, Pa., 116-130.

Leonards, G. A. (1977). Panel discussion, Proceedings ninth international conference on soil mechanics and foundation engineering, Tokyo, 3, 384 – 386

Leroueil, S., Tavenas, F., Brucy, F., La Rochelle, P. & Roy, M. (1979). Behaviour of destructured natural clays. Proc. ASCE 105, No. GT6, 759±778.

Li, X. (2017). Experimental Investigations for SAGD Well Integrity Numerical Modelling: M.Sc. Thesis.

Mesri, G. (2001). Primary Compression and Secondary Compression. *Soil Behavior and Soft Ground Construction, Geotechnical Special Publication, ASCE*, (119), 122–166.

Mesri, G., & Ajlouni, M. A. (1997). Viscous behaviour of soil under oedometric conditions: Discussion. *Canadian Geotechnical Journal*, *34*, 159–161.

Mesri, G., & Castro, A. (1987). Ca/Cc Concept and Ko During Secondary Compression. *Journal of Geotechnical Engineering, ASCE*, *113*(3), 230–247.

Mesri, G., & Choi, Y. K. (1984). Time effects on the stress-strain behaviour of natural soft clays: Discussion. *Geotechnique*, *34*(3), 439–442.

Mesri, G., & Choi, Y. K. (1985). The Uniqueness of th End-of-Primary (EOP) Void Ratio-Effective Stress Relationship. In *11th International Conference on Soil Mechanics and Foundation Engineering* (Vol. 2, pp. 587–590). San Francisco, California.

Mesri, G., & Feng, T. W. (2014). Consolidation of soils. *Geotechnical Special Publication*, (233), 322–337.

Mitchell, J. K., & Soga, K. (2005). *Fundamentals of Soil Behavior*. (I. John Wiley & Sons, Ed.) (Third Edit).

Oldakowski, K., Sawatzky, R. P., & Alvarez, J. M. (2016). Geomechanical Properties of Clearwater Shale at Elevated Temperatures. *SPE Canada Heavy Oil Technical Conference*, (June), 1–35.

Petrochina Canada. (2018). 2018 Performance Presentation MacKay River Commercial Project.

Rassouli, F., & Zoback, M. (2017). *Laboratory Study on the Effects of Carbonates and Clay Content on Viscoplastic Deformation of Shales at Reservoir Conditions: Ph.D. Thesis*. Stanford University.

Research Council of Alberta. (1959). *Geology of the McMurray Formation Part III General Geology of the McMurray Area*.

Schmertmann, B. J. H. (1992). The mechanical aging of soils, *117*(9), 1288–1330.

Sone, H, & Zoback, M. (2010). Strength, creep and frictional properties of gas shale reservoir rocks. *44th US Rock Mechanics Symposium and 5th U.S.-Canada Rock Mechanics Symposium. Salt Lake City, UT*.

Sone, Hiroki. (2012). Mechanical Properties of Shale Gas Reservoir Rocks and its Relation to the In-Situ Stress Variation Observed in Shale Gas Reservoirs: Ph.D. Thesis. *Stanford University*.

Sone, Hiroki, & Zoback, M. D. (2013). Mechanical properties of shale-gas reservoir rocks — Part 2: Ductile creep, brittle strength, and their relation to the elastic modulus. *Geophysics*, *78*(5), D393–D402.

Sone, Hiroki, & Zoback, M. D. (2014). Time-dependent deformation of shale gas reservoir rocks and its long-term effect on the in situ state of stress. *International Journal of Rock Mechanics and Mining Sciences*, *69*, 120–132.

Stark. (1995). Measurement of Drained Residual Strength of Overconsolidated Clays. *Transportation Research Record*, 26–34. Retrieved from

Stark, T., Choi, H., & McCone, S. (2005). Drained Shear Strength Parameters for Analysis of Landslides. *Journal of Geotechnical and Geoenvironmental Engineering*, *131*(5), 575–588.

Stark, T. D. (2016). Development and Use of Fully Softened Shear Strength in Slope Stability Analyses Preface and Acknowledgments.

T. Hueckel and G.Baldi. (1990). THERMOPLASTICITY OF SATURATED C L A Y S : EXPERIMENTAL CONSTITUTIVE STUDY, *116*(12), 1778–1796.

Tavenas, F., Leroueil, S., La Rochelle, P., & Roy, M. (1978). Creep behavior of an undisturbed lightly overconsolidated clay. *Canadian Geotechnical Journal*, *15*(3), 402–423.

Taylor, D. W., & Merchant, W. (1940). A Theory of Clay Consolidation Accounting for Secondary Compression. *Journal of Mathematics and Physics*, *19*(4), 167–185.

Terzaghi, K., Peck, R. B., & Mesri, G. (1996). *Soil Mechanics in Engineering Practice* (Third Edit). New York, NY, USA.

Terzaghi K (1925) Erdbaumechanik auf Bodenphysikalischer Grundlage. Franz Deuticke, Liepzig-Vienna

Townsend, F. C., and Banks, D. C. 共1974夫. “Preparation effects on clay shale classification indexes.” Proc., Natl. Meet.on Water Res. Eng., ASCE, New York, 21–25

Total E&P Canada Ltd. (2007). *Summary of Investigations into The Joslyn May 18th 2006 Steam Release*.

Wong, G. (2007). Geomechanical Characterization for Clearwater Formation Clay Shale: MEng Thesis. University of Alberta.

Xu, B., Yuan, Y. G., & Wang, Z. C. (2011). Thermal Impact On Shale Deformation/Failure Behaviors - Laboratory Studies. *45th U.S. Rock Mechanics / Geomechanics Symposium*.

Zadeh, N. S. (2016). *Multiple Packer Techniques for In Situ Stress Measurement in Hard Soils-Soft Rocks. Ph.D. Thesis*. University of Alberta.

Zadeh, N. S., & Chalaturnyk, R. (2015). Geotechnical Characterization of Clearwater Clay Shale and Comparison of the Properties with Other Cretaceous Clay Shales in North America. *Journal of Canadian Petroleum Technology*, *54*(6), 394–411.